



HAL
open science

Towards general network architecture design criteria for negative gas adsorption transitions in ultraporous frameworks

Simon Krause, Jack Evans, Volodymyr Bon, Irena Senkowska, Paul Iacomi, Felicitas Kolbe, Sebastian Ehrling, Erik Troschke, Jürgen Getzschmann, Daniel M Többens, et al.

► To cite this version:

Simon Krause, Jack Evans, Volodymyr Bon, Irena Senkowska, Paul Iacomi, et al.. Towards general network architecture design criteria for negative gas adsorption transitions in ultraporous frameworks. Nature Communications, 2019, 10 (1), 10.1038/s41467-019-11565-3 . hal-02282172v1

HAL Id: hal-02282172

<https://hal.umontpellier.fr/hal-02282172v1>

Submitted on 9 Sep 2019 (v1), last revised 19 May 2020 (v2)

HAL is a multi-disciplinary open access archive for the deposit and dissemination of scientific research documents, whether they are published or not. The documents may come from teaching and research institutions in France or abroad, or from public or private research centers.

L'archive ouverte pluridisciplinaire **HAL**, est destinée au dépôt et à la diffusion de documents scientifiques de niveau recherche, publiés ou non, émanant des établissements d'enseignement et de recherche français ou étrangers, des laboratoires publics ou privés.

Towards General Network Architecture Design Criteria for Negative Gas Adsorption Transitions in Ultraporous Frameworks

Simon Krause, Jack D. Evans, Volodymyr Bon, Irena Senkowska, Paul Iacomi, Felicitas Kolbe, Sebastian Ehrling, Erik Troschke, Jürgen Getzschmann, Daniel D. Többens, Alexandra Franz, Dirk Wallacher, Pascal G. Yot, Guillaume Maurin, Eike Brunner, Philip L. Llewellyn, François-Xavier Coudert, Stefan Kaskel

Submitted date: 12/03/2019 • Posted date: 13/03/2019

Licence: CC BY-NC-ND 4.0

Citation information: Krause, Simon; Evans, Jack D.; Bon, Volodymyr; Senkowska, Irena; Iacomi, Paul; Kolbe, Felicitas; et al. (2019): Towards General Network Architecture Design Criteria for Negative Gas Adsorption Transitions in Ultraporous Frameworks. ChemRxiv. Preprint.

Critical design criteria for negative gas adsorption (NGA), a counterintuitive feature of pressure amplifying materials, hitherto uniquely observed in a highly porous framework compound (DUT-49), are derived by analysing the physical effects of micromechanics, pore size, interpenetration, adsorption enthalpies, and the pore filling mechanism using advanced in situ X-ray and neutron diffraction, NMR spectroscopy, and calorimetric techniques parallelized to adsorption for a series of six isorecticular networks. Aided by computational modelling, we identify DUT-50 as a new pressure amplifying material featuring distinct NGA transitions upon methane and argon adsorption. In situ neutron diffraction analysis of the methane (CD₄) adsorption sites at 111 K supported by grand canonical Monte Carlo simulations reveals a sudden population of the largest mesopore to be the critical filling step initiating structural contraction and NGA. In contrast, interpenetration leads to framework stiffening and specific pore volume reduction, both factors effectively suppressing NGA transitions.

File list (5)

Krause et al - Towards NGA design - manuscript.pdf (1.12 MiB)	view on ChemRxiv • download file
Krause et al. Supplementary video.gif (27.67 MiB)	view on ChemRxiv • download file
Krause et al - Towards NGA design - ESI.pdf (3.82 MiB)	view on ChemRxiv • download file
MOF-FF optimized simulated structures.zip (247.99 KiB)	view on ChemRxiv • download file
SCXRD-cif.zip (48.45 KiB)	view on ChemRxiv • download file

Towards general network architecture design criteria for negative gas adsorption transitions in ultraporous frameworks

Simon Krause¹, Jack D. Evans^{1,2}, Volodymyr Bon¹, Irena Senkowska¹, Paul Iacomi³, Felicitas Kolbe¹, Sebastian Ehrling¹, Erik Troschke¹, Jürgen Getzschmann¹, Daniel M. Töbrens⁴, Alexandra Franz⁴, Dirk Wallacher⁴, Pascal G. Yot⁵, Guillaume Maurin⁵, Eike Brunner¹, Philip L. Llewellyn³, François-Xavier Coudert², Stefan Kaskel^{1*}

Abstract

Critical design criteria for negative gas adsorption (NGA), a counterintuitive feature of pressure amplifying materials, hitherto uniquely observed in a highly porous framework compound (DUT-49), are derived by analysing the physical effects of micromechanics, pore size, interpenetration, adsorption enthalpies, and the pore filling mechanism using advanced *in situ* X-ray and neutron diffraction, NMR spectroscopy, and calorimetric techniques parallelized to adsorption for a series of six isorecticular networks. Aided by computational modelling, we identify DUT-50 as a new pressure amplifying material featuring distinct NGA transitions upon methane and argon adsorption. *In situ* neutron diffraction analysis of the methane (CD₄) adsorption sites at 111 K supported by grand canonical Monte Carlo simulations reveals a sudden population of the largest mesopore to be the critical filling step initiating structural contraction and NGA. In contrast, interpenetration leads to framework stiffening and specific pore volume reduction, both factors effectively suppressing NGA transitions.

Introduction

Porous solids featuring adaptable pore sizes as a stimulated response to characteristic molecules in the gas phase, i.e. changes of gas pressure or activity, led to the discovery of unique phenomena such as gating¹, breathing², and more recently negative gas adsorption (NGA)³. Metal-Organic Frameworks (MOFs) reach record values of porosity⁴⁻⁶ (specific surface area, pore volume), often at the expense of reduced mechanical stability⁷. Hence, energetics at the solid-fluid interface reach an order of magnitude comparable with chemical bond energetics leading to stimuli responsive structural transformations and severe deformations of the framework constituents. A stark contrast in adsorption behaviour compared to rigid adsorbents⁸⁻¹¹ has promoted new applications in gas separation^{12,13}, storage¹⁴, proton conduction¹⁵, and sensing¹⁶. However, the mechanistic understanding and rational governing responsivity in such soft porous solids is still at an early stage¹⁷⁻²⁰. The experimental discovery of flexibility in MOFs has often been dictated by serendipity while rational synthesis strategies have rarely been applied²¹. Rationalization of adsorption-induced structural transformations has been achieved by analysing their thermodynamics via Density Functional Theory (DFT)²⁰ and molecular dynamic (MD) simulations²², demonstrating the importance of micromechanics in responsive frameworks. But modular construction of MOFs provides an ideal platform to achieve a mechanistic understanding of adsorption induced structural deformations.

35 Isoreticular pore expansion is a powerful modular concept²³ leading to prototypical series of solids with
36 individually adjustable porosity and flexibility²⁴⁻²⁷. The versatility of this approach provides clear
37 structure-property relationships and mechanistic insights by independently probing the impact of surface
38 functionality, mechanical stiffness and porosity.

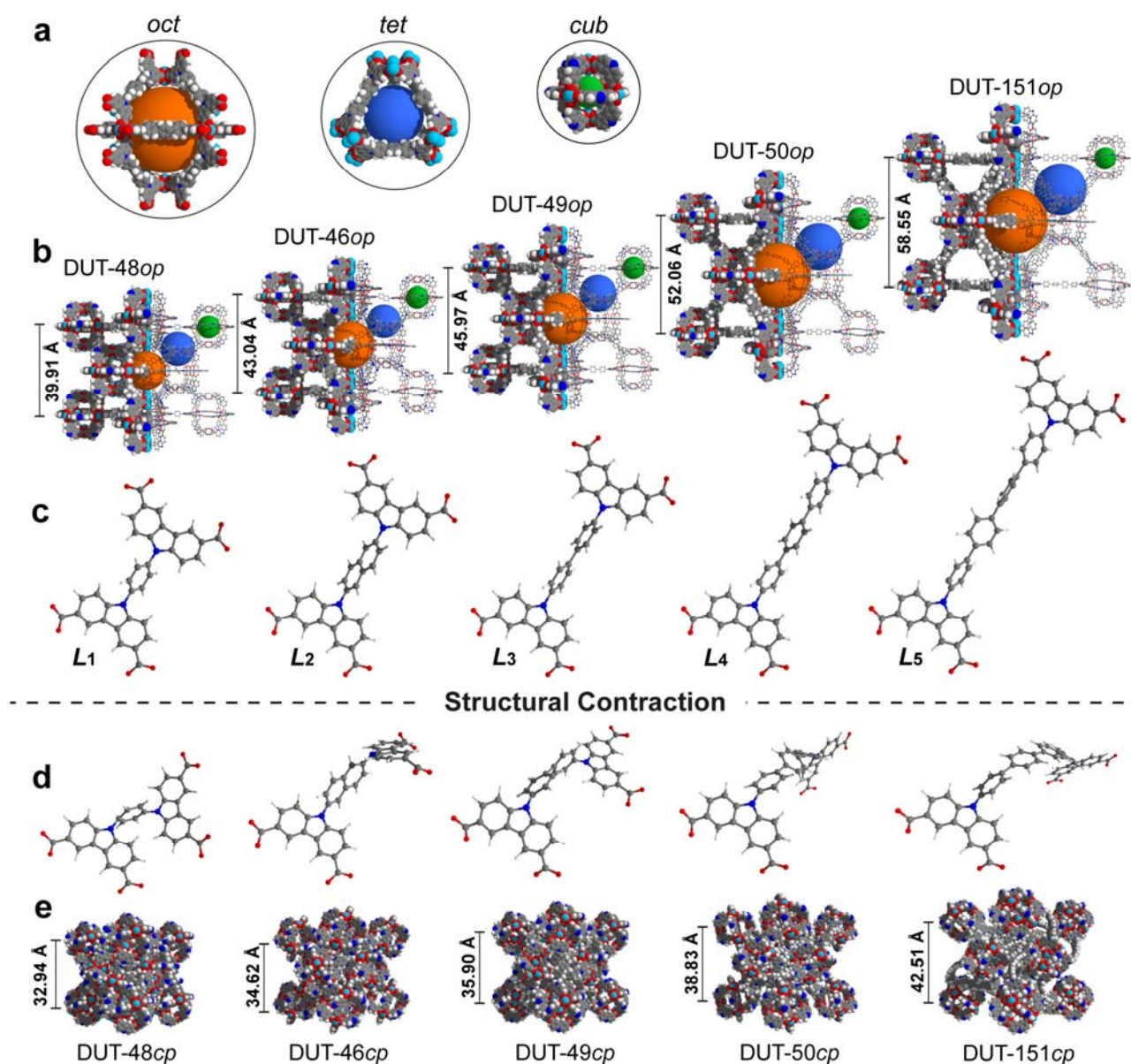
39 Negative Gas Adsorption (NGA) is a novel counterintuitive phenomenon discovered in a highly porous
40 framework³. DUT-49, a MOF constructed by connecting 9*H*-carbazole-3,6-dicarboxylate-based metal-
41 organic polyhedra (MOP) with 4,4'-substituted 1,1'-biphenyl, was originally synthesized for methane
42 storage applications²⁸. However, upon adsorption of gases such as methane (111 K) or *n*-butane (298 K)³
43 a colossal structural contraction is induced, accompanied by an external gas pressure increase. NGA
44 materials show self-propelled gas pressure amplification. Upon structural contraction, DUT-49 expels
45 previously adsorbed gas from the framework leading to a step-wise desorption in the adsorption branch of
46 the isotherm corresponding to a pressure amplification in the closed measuring cell³. Such NGA
47 transitions require the system to traverse through metastable states. Experimental and computational
48 analysis of NGA in DUT-49 revealed enhanced solid-fluid interactions for the contracted pore structure
49 (*cp*) to be the driving force for the contraction of the initially stable open pore state (*op*)²⁹. The structural
50 transitions during NGA for xenon (200 K) were confirmed by *in situ* ¹²⁹Xe NMR spectroscopy³⁰, while
51 for nitrogen (77 K), a subtle influence of crystallite size indicates NGA to be a highly cooperative
52 phenomenon, as structural transitions are suppressed in small crystallites (< 1 μm).³¹ Reducing the pore
53 size and ligand length in an isoreticular network (DUT-48) increases the framework rigidity and
54 decreases the energetic driving force for the contraction, suppressing the adsorption-induced structural
55 transition³², while the external pressure, inducing the compaction is increased from 35 MPa (DUT-49) to
56 65 MPa (DUT-48) using mercury as the pressure transducing medium.

57 Until today, DUT-49 has been the only known framework material showing NGA transitions. In the
58 following we deduce rational design criteria for NGA, prerequisites from the perspective of the network
59 structure, using a combined theoretical and experimental approach. Systematic linker elongation in a
60 series of six isoreticular frameworks shows the crucial importance of pore size, framework softness, and
61 interpenetration to permit adsorption-induced structural contraction leading to NGA transitions. The
62 computational prediction is confirmed by experimental analysis of the structural transitions using
63 advanced *in situ* diffraction, calorimetric, and spectroscopic experimentation. Ultimately, we deduce
64 DUT-50 as the second NGA material among more than 20.000 MOFs known today. This finding
65 indicates NGA to be a general phenomenon observable for a wider class of highly porous materials
66 satisfying specific structural design rules.

67 ***In silico* network micromechanics**

68 The assembly of modular porous networks and prediction of their properties for separation and storage of
69 gaseous energy carriers is nowadays effectively aided by computational modelling³³⁻³⁶. Consequently,
70 before investing major synthetic efforts, we decided to model an isoreticular series of DUT-48-derived
71 MOFs with increasing ligand length. Based on the experimental crystal structures of DUT-48³² and DUT-

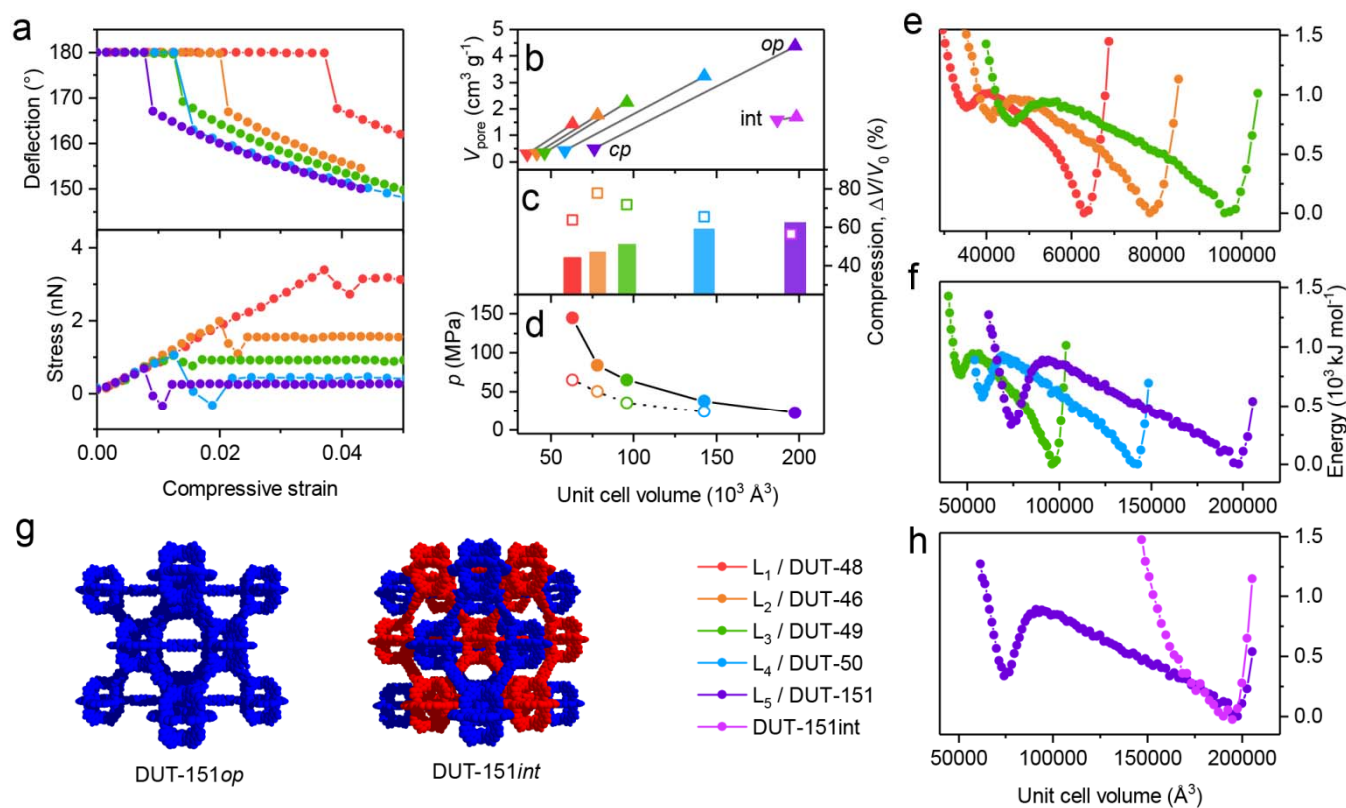
72 49²⁸ the number of 1,4-substituted phenylene units in the ligand backbone was increased step-wise from
 73 one in L₁ (DUT-48, Figure 1) and two in L₃ (DUT-49), to three in L₄ (DUT-50), and four units in L₅
 74 (DUT-151). In addition, we decided to include a 2,6-substituted naphthalene unit in L₂ (DUT-46) to
 75 achieve an intermediate length between L₁ and L₃. As a result, a series of five MOFs was obtained all
 76 sharing the same topology and trimodal pore structure with lattice constants increasing from 39.91 to
 77 58.55 Å and pore volumes ranging from 1.8 to 4.6 cm³ g⁻¹ (DUT-48 to DUT-151, Figure 1).



78

79 **Figure 1. Crystal structures and ligands of isoreticular DUT-49 derivatives.** **a** Trimodal pore system: octahedral (*oct*, orange), tetrahedral
 80 (*tet*, blue), cuboctahedral (*cub*, green). **b** Crystal structures of open pore (*op*) of DUT-48, 46, 49, 50, and non-interpenetrated DUT-151 from
 81 left to right including respective lattice parameter of the cubic unit cells with *Fm* $\bar{3}$ *m* symmetry. **c-d** Conformation of ligands L₁ – L₅ before
 82 (c) and after (d) structural contraction. **e** Crystal structures of contracted pore (*cp*) structures of DUT-48, 46, 49, 50, and non-interpenetrated
 83 DUT-151 from left to right including respective lattice parameter of the cubic unit cells with *Pa* $\bar{3}$ symmetry. Lattice constants for the
 84 structures were obtained by relaxation using force fields which were found to describe the behaviour of DUT-49 well^{29,37}. Colour code:
 85 hydrogen (white), carbon (grey), nitrogen (blue), oxygen (red), and copper (turquoise).

86 The compression of empty DUT-49_{op} requires significant energy and is dominated by the buckling
 87 deformation of the ligand. For first insights into micromechanics we analysed the buckling behaviour of
 88 isolated ligands L₁-L₅ using DFT methods by applying compressive strain decreasing the N-N distance
 89 from the local minimum to a compressive strain of 0.05 (Figure 2).



90

91 **Figure 2. Mechanical properties of ligands and MOFs.** a DFT analysis of ligands L₁ (red), L₂ (orange), L₃ (green), L₄ (blue), and L₅
 92 (purple). b Evolution of pore volume upon contraction in the open (triangles up) and closed (triangles down) states, c Compression by
 93 hydrostatic pressure (open squares correspond to Hg intrusion experiments). d Transition pressures under hydrostatic compression (open
 94 circles correspond to Hg intrusion experiments). e-f Free energy profiles of non-interpenetrated MOFs per unit cell. g Structures of non- and
 95 double interpenetrated DUT-151. h Free energy profiles of DUT-151 and DUT-151_{int}. Colour code: DUT-48 (red), DUT-46 (orange), DUT-
 96 49 (green), DUT-50 (blue), DUT-151 (purple) and DUT-151_{int} (pink). Closed symbols represent simulation, open symbols experimental
 97 data.

98 For all ligands, the initial elastic deformation regime is followed by severe inelastic ligand deflection at
 99 higher compressive strain. As expected, the shorter ligands withstand higher stress (L₁: 3.40 nN, L₂:
 100 1.99 nN) before buckling occurs. While buckling of L₄ is observed at 1.06 nN in the range of L₃
 101 (1.04 nN), L₅ demonstrates buckling at even lower stress (0.68 nN), indicating that these ligands and
 102 consequently the MOFs should demonstrate softer behaviour similar to DUT-49. Because the ligands are
 103 comprised of the same phenylene-based backbone with varying length, all ligands display equivalent
 104 elastic moduli and the mechanical behaviour can be exclusively attributed to the variation in length. To
 105 ascertain whether the behaviour of a single ligand is transferable to the behaviour of the corresponding
 106 crystalline network, we analysed the compressibility and free energy profile of a whole unit cell by
 107 computationally less expensive classical methods using force fields which were found to describe the
 108 behaviour of DUT-49 well^{29,37}. The free energy profiles of the series of MOFs were all found to exhibit a

109 bistable nature, a crucial requirement for NGA, with activation energies in a comparable range. However,
110 transition pressures and energies for the structural contraction were found to decrease with increasing
111 ligand length (Supplementary Table 31). Consequently, ligand elongation in this system should favour
112 adsorption-induced structural contraction and potentially NGA, assuming that the adsorption-induced
113 stress in these systems is of comparable magnitude.

114 **Synthesis of ligands and MOFs**

115 A retrosynthetic approach based on previously described synthesis of carbazole-derived carboxylates³⁸
116 was developed to obtain the proposed ligands and MOF materials. Ligands L₁-L₅ could be obtained in
117 six-step syntheses with total yields of over 60% (for detailed information see Supplementary Chapter 2).
118 The crystalline network syntheses were elaborated to yield phase pure crystalline powders of the targeted
119 MOFs as confirmed by powder X-ray diffraction (PXRD) (Supplementary Figure 5), thermogravimetric
120 analysis (Supplementary Figure 6), elemental analysis (Supplementary Table 5), and diffuse reflectance
121 infrared Fourier transform (DRIFT) spectroscopy (Supplementary Figure 59). Desolvation of the MOF
122 powders was performed using a protocol previously applied on DUT-49³. Particle size distributions were
123 determined via scanning electron microscopy (SEM) and the mean crystal size was found to exceed
124 2.5 μm (Supplementary Table 6). The latter is important, as we recently demonstrated that NGA critically
125 depends on crystallite size for DUT-49³¹.

126 The structures of DUT-46, 50, and 151 were determined using synchrotron-based single crystal X-ray
127 diffraction experiments. They crystallize in the cubic space group $Fm\bar{3}m$, except DUT-151 which
128 crystallizes in the monoclinic space group $C2/m$ containing two interwoven **fcu** nets (Supporting
129 Information 3.4.2). The latter finding is interesting for two reasons: First, it demonstrates limitations of
130 ligand elongation to obtain a non-interpenetrated structure in the IR-series of DUT-49 at given synthesis
131 conditions. Second, the impact of interpenetration on structural contraction and NGA can be analysed.
132 Consequently, the computational analysis of DUT-151 was extended by the experimentally obtained
133 interpenetrated crystal structure DUT-151_{int}. The free energy profile no longer exhibits a bistable nature
134 in the energy range of the non-interpenetrated structures which can be expected for a much denser
135 structure that lacks the void required for the ligand buckling upon contraction (Figure 2 g,h).

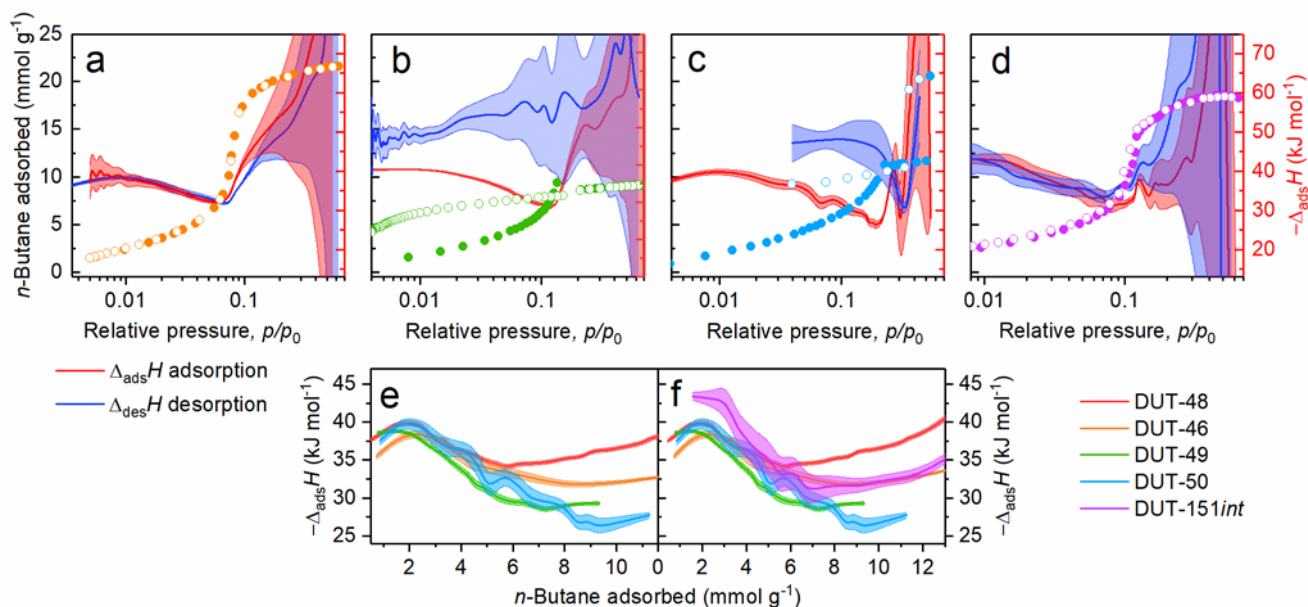
136 **Experimental analysis of structural responsivity**

137 The response of the guest-free MOF powders towards external mechanical pressure was experimentally
138 analysed using mercury as a pressure transducing medium, revealing an upper stress limit for compaction
139 and the corresponding volume changes³² (Supplementary Figure 17). With increasing linker length the
140 transition pressures corresponding to the compression of the frameworks decrease from 65 MPa (DUT-
141 48) to 24 MPa (DUT-50). The experimental pressures follow the trend of the simulated values but are
142 found to be in general lower, however within the range of accuracy of these methods (Figure 2d). The
143 volume change upon compression was found to be larger than simulated values with higher deviation for

144 DUT-48 and DUT-47, indicating a complete compaction of the networks for both, while a good
 145 agreement for an *op-cp* transition is observed for DUT-50 (Figure 2c). However, reliable phase analysis
 146 after compression is hampered by mercury contamination. The gradual intrusion curve observed for
 147 DUT-151*int* (Supplementary Figure 17) with an initial transition pressure of 29 MPa and a total
 148 volumetric compression of only 1.53 cm³ g⁻¹ indicates a transition mechanism different compared to the
 149 non-interpenetrated structures, for example caused by inter-framework dynamics.

150 In order to elucidate structural design criteria provoking NGA and pressure amplification in the networks,
 151 we analysed the new network series with respect to adsorption-induced structural contractions by
 152 exposing them to gases such as *n*-butane (273, 298, 303 K, Supplementary Figure 13) and methane
 153 (111 K, Supplementary Figure 14)³. Nitrogen (77 K) and argon (87 K) adsorption were used to
 154 characterise textural properties such as surface area and pore volume (Supplementary Figure 12).
 155 Methane adsorption at 111 K and argon adsorption at 87 K finally allowed us to uncover DUT-50 as a
 156 new material showing pronounced NGA transitions and hysteresis similar to DUT-49, while none of the
 157 other networks exhibit NGA. DUT-46 showed no hysteresis and the isotherm is similar to DUT-48.
 158 Isotherms of DUT-151*int* exhibit small hysteresis but absence of NGA due to a higher rigidity and lack of
 159 bistability (Figure 2h).

160 *In situ* calorimetry during the adsorption and desorption of *n*-butane at 303 K allowed us to measure the
 161 differential enthalpy of adsorption $\Delta_{\text{ads}}H$ and thus experimentally analyse the adsorption energetics during
 162 NGA at near ambient conditions (Figure 3).

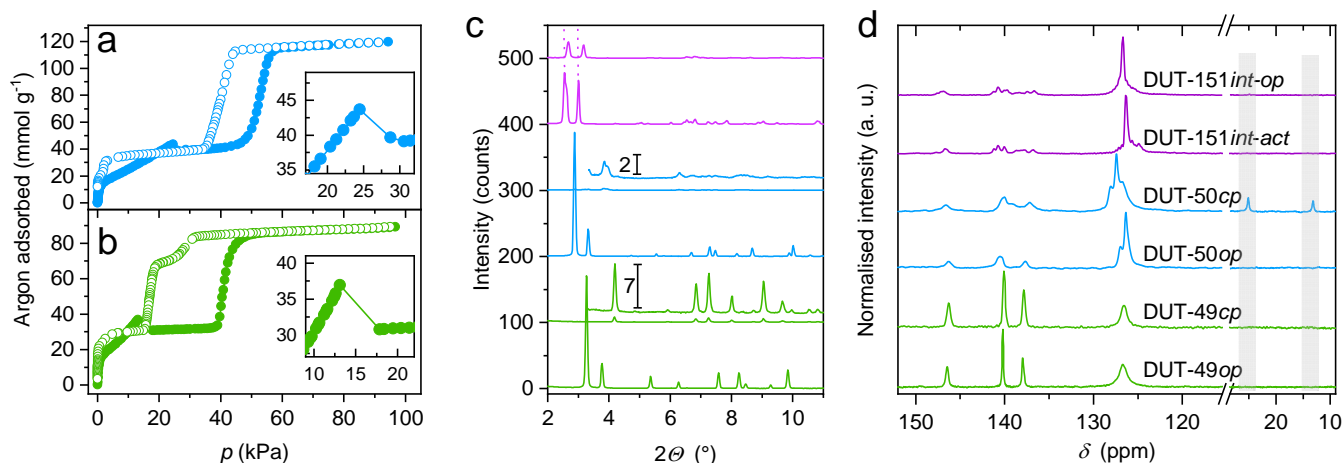


163
 164 **Figure 3. Analysis of *n*-butane adsorption energetics.** *In situ* calorimetric analysis in parallel to adsorption/desorption of *n*-butane at 303 K
 165 for **a** DUT-46, **b** DUT-49, **c** DUT-50, and **d** DUT-151*int*. Adsorption and desorption in closed and open symbols, respectively, adsorption
 166 enthalpies red, enthalpy of desorption blue, error regimes indicated as coloured areas. **e-f** Adsorption enthalpies plotted against adsorbed
 167 amount of *n*-butane for the series non-interpenetrated MOFs (**e**) and in comparison with DUT-151*int* (**f**).

168 For the entire series of non-interpenetrated structures, the enthalpy profile during adsorption exhibits a
 169 maximum at $p/p_0 \approx 0.01$. With increasing pressure, a reduction and minimum of $|\Delta_{\text{ads}}H|$ is observed

170 shifting to increasing p/p_0 with increasing ligands length (DUT-48: $p/p_0 = 0.06$, DUT-50: $p/p_0 = 0.2$). A
 171 subsequent sudden increase in $|\Delta_{\text{ads}}H|$ correlates with a steep slope in uptake in the isotherm due to
 172 enhanced fluid-fluid interactions at complete pore filling. At lower p/p_0 , the enthalpy profiles are identical
 173 for the investigated series reflecting similar adsorption mechanisms at lower loadings. However, with
 174 increasing pore size, the confinement of the guest is expected to decrease³⁹ well reflected by the observed
 175 reduction in $|\Delta_{\text{ads}}H|$ with increasing ligand length and corresponding pore volume of the MOF (Figure
 176 3f). In DUT-46, a non-hysteretic profile is observed for both isotherm and enthalpy branches (Figure 3a).
 177 In DUT-49 and DUT-50, an increase in enthalpy is observed upon desorption after NGA alongside a
 178 hysteresis in the isotherm. Thus, the analysis of the desorption branch provides information about the
 179 adsorption enthalpy of the *cp* phase. The difference of enthalpy between the *op* and *cp* structure was
 180 previously found to be the driving force of the structural contraction³ and is now for the first time
 181 accessible experimentally in the pressure range of NGA. When this difference ($25.4 \pm 2 \text{ kJ mol}^{-1}$) is
 182 multiplied by the number of *n*-butane molecules (n_{ads}) adsorbed per unit cell in the *op* phase, $\Delta\Delta_{\text{ads}}H_{\text{total}}$
 183 approximates the gain in enthalpy per unit cell upon structural contraction. Interestingly, upon adsorption
 184 of *n*-butane in DUT-49, $\Delta\Delta_{\text{ads}}H_{\text{total}} = -4470 \pm 550 \text{ kJ mol}_{\text{uc}}^{-1}$ (mol_{uc} refers 1 mol unit cells of the respective
 185 DUT) which exceeds the transition energy calculated for guest-free DUT-49 by over $2500 \text{ kJ mol}_{\text{uc}}^{-1}$
 186 (Figure 2f). In comparison, DUT-151_{int} shows a higher adsorption enthalpy throughout the whole
 187 pressure range, reflecting the smaller pore size and enhanced solid-fluid interactions. A small hysteresis at
 188 a relative pressure of 0.06-0.11 indicates possible network displacements of the two interpenetrating nets
 189 (Supplementary Figure 16).

190 To analyse the structural transitions further we performed *in situ* PXRD experiments in parallel to
 191 adsorption of *n*-butane at 273 K. DUT-50 shows significant peak broadening and loss of crystallinity
 192 upon adsorption of *n*-butane at 20 kPa and 273 K (Figure 4c, Supplementary Figure 19).



193
 194
 195 **Figure 4. Argon adsorption, *in situ* X-ray diffraction and NMR spectroscopy.** a, b Argon adsorption (filled circles) and desorption
 196 (open circles) isotherm at 87 K of DUT-50 (a) and DUT-49 (b), inset represents magnified region of NGA. c X-ray diffraction patterns of
 197 evacuated (bottom) and *n*-butane loaded (top) samples at 273 K including magnification (offset 100 counts). d ¹³C CP MAS NMR spectra of
 198 argon-filled (bottom) and *n*-butane loaded (top) samples at 298 K, grey areas indicate peaks corresponding to *n*-butane. Colour code: DUT-
 199 49 (green), DUT-50 (blue), DUT-151_{int} (purple).

200 At elevated pressures the peaks of the pristine *op* phase reappear, reflecting the reversible reopening of
201 the structure indicating a rare crystalline-disordered-crystalline transition. Upon desorption, the *op* phase
202 undergoes contraction without indications for reopening at lower pressure. The fact that DUT-50
203 completely transforms into the *op* phase at higher pressures suggests that the framework connectivity is
204 preserved and is an evidence for a cooperative transformation within a single crystal. Reduction in
205 crystallinity upon DUT-50 contraction is more pronounced in comparison to DUT-49 (Figure 4c)
206 indicating a higher degree of flexibility of the ligand and loss of long-range order of the building units
207 within the highly porous network providing a higher degree of freedom for displacements of the building
208 blocks. For complementary understanding of the local structural transformations we analysed the series of
209 MOFs by *in situ* DRIFT (Supplementary Figure 60 - Supplementary Figure 66) and solid-state ¹³C cross-
210 polarization (CP) MAS NMR spectroscopy (Supplementary Figure 67 - Supplementary Figure 70) in
211 parallel to adsorption of *n*-butane at 298 K. Both methods are ideal to probe local chemical environments
212 independent of long-range order and crystallinity. Indeed, only a small degree of peak broadening in the
213 spectra of both methods is observed upon contraction indicating a uniform ligand conformation in the *cp*
214 phase in both DUT-49 and 50. Shifts especially of peaks assigned to C-H groups of the bridging units
215 indicate uniform changes in the local environment associated with the buckling illustrated in Figure 1.
216 Additionally, two signals in the ¹³C CP MAS NMR spectra at lower chemical shifts are observed upon
217 contraction in DUT-50 (Figure 4 c). They can be assigned to the aliphatic carbons of *n*-butane indicating
218 a partial immobilization of *n*-butane within the contracted pores. In contrast, spectra of *n*-butane loaded
219 DUT-48 and DUT-151*int* which do not undergo large scale structural contraction do not exhibit these
220 peaks, demonstrating the rapid diffusion of the *n*-butane within the open pores of these systems.
221 Comparison of the DRIFT spectra for *op* and *cp* structures in DUT-49 and DUT-50 (Supplementary
222 Figure 62, 63) demonstrate red shifts of several peaks that can be attributed to elongation of the C-N and
223 C-C bonds in the bridging unit of the ligands. Vibrations of the carbazole-core remain mostly unchanged
224 indicating that the structure of the MOPs remains unchanged upon structural contraction. Although the
225 spectroscopic analysis supports that the structural contraction in DUT-50 is of similar nature as in DUT-
226 49, the dynamics of DUT-50*cp* at 273 K obstruct an in depth crystallographic structural analysis. As this
227 high degree of mobility within the strained ligands may be reduced at lower temperature, we decided to
228 analyse the adsorption behaviour with *in situ* PXRD for methane at 111 K (Supplementary Figure 20) as
229 an NGA inducing medium. Again, a strong reduction of crystallinity and peak broadening is observed
230 after NGA, however less severe compared to the patterns recorded in the presence of *n*-butane at 273 K.
231 The unit cell of DUT-50*cp*, appearing after NGA was refined by Le Bail method in monoclinic symmetry
232 (*P*2₁/*c* space group). The unit cell volume of 60611 Å³ represents a 59% volume reduction compared with
233 DUT-50*op*. The latter is in good agreement with DUT-50*cp* predicted *in silico* (*V* = 58185 Å³, Figure 2e
234 and Supplementary Table 31). In summary, DUT-50 undergoes NGA transitions analogous to those of
235 DUT-49, as demonstrated using various *in situ* methods confirming the predicted structural models.

236 For DUT-151*int* only minor structural flexibility is observed, as predicted by *in silico* modelling. The
237 PXRD patterns of DUT-151*int* after supercritical activation (DUT-151*int-act*) show a shift of peaks in the
238 range of 2-3.5° to lower 2 θ values and appearance of new reflections in comparison with the as made

239 material are observed. This change can be assigned to a change in symmetry and unit cell volume upon
240 solvent removal from monoclinic $C2/m$ (in solvated DUT-151 int) to triclinic $P\bar{1}$ in DUT-151 $int-act$.
241 Adsorption of *n*-butane at 273 K at intermediate pressures (8-10 kPa) causes reformation of the initial
242 monoclinic net ($C2/m$), however the structure is contracted by 14% (DUT-151 $int-cp$, 87419 Å³) compared
243 with DUT-151 int (101103 Å³). With increasing pressure, the unit cell volume increases again reaching
244 101740 Å³ (DUT-151 $int-op$). The reversed path is observed during desorption (For structural details see
245 Supplementary Figure 31). Overall, the ligand deformations are less severe and the difference in pore
246 volume of DUT-151 $int-op$ vs. $-cp$ is only 0.32 cm³ g⁻¹, less than 20 % compared with the colossal
247 contractions in DUT-49 and DUT-50. DUT-151 int lacks the pronounced bistability required for NGA
248 materials as predicted *in silico* (Figure 2h) and confirmed by *in situ* PXRD (Supplementary Table 14 and
249 Supplementary Figure 27).

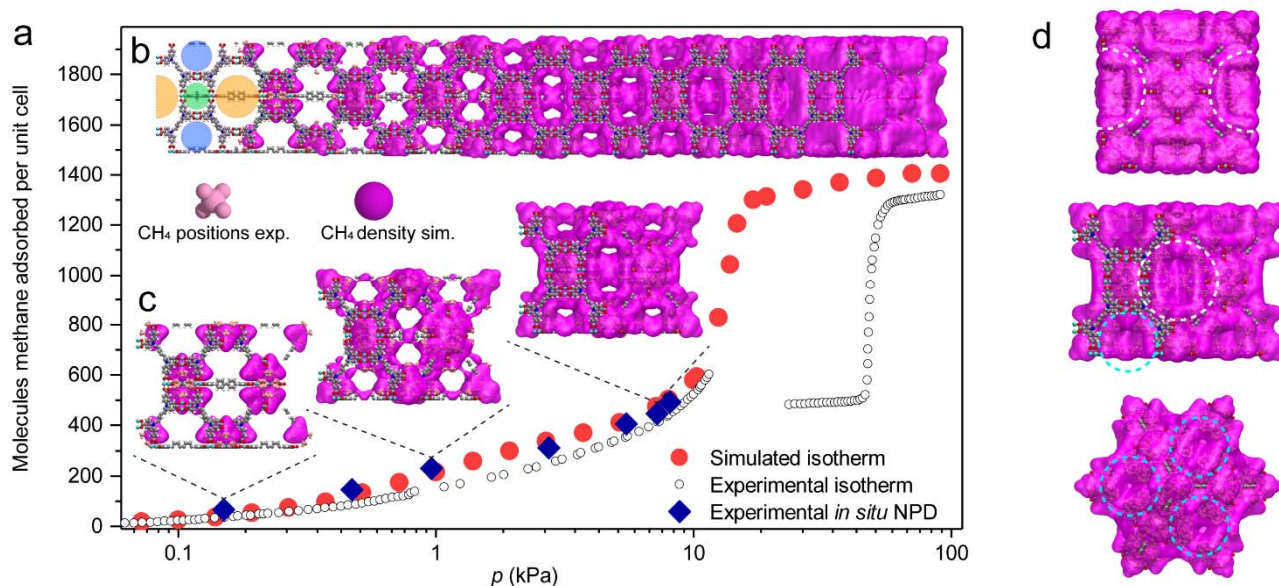
251 ***In situ* analysis of the adsorbate structure**

252 In regard to the adsorption mechanism of NGA two open questions remain: (i) what is the role of
253 characteristic adsorbate structures forming metastable states and their role in pressure amplification
254 phenomena in mesoporous networks, and (ii) from which pore of the frameworks is the gas released upon
255 NGA. To locate methane molecules within the pores of DUT-49 and derivatives at different
256 pressures/loadings, we decided to combine computational grand canonical Monte Carlo (GCMC) analysis
257 of methane with experimental *in situ* neutron powder diffraction (NPD) in parallel to the adsorption of
258 deuterated methane (CD₄) at 111 K. NPD has previously been used to investigate primary adsorption sites
259 in MOFs *via* Rietveld refinement⁴⁰⁻⁴³, however the analysis of higher loadings in mesoporous networks at
260 elevated temperatures such as 111 K, crucial for mechanistic understanding of NGA, remains unexplored.

261 Methane adsorption isotherms and corresponding adsorption enthalpy profiles at 111 K for *op* and *cp*
262 phases were simulated by GCMC methods (Supplementary Figure 71). A good agreement between the
263 simulated and the experimental isotherms (Supplementary Figure 14) indicates the validity of the
264 simulations which allow to further analyse the adsorption energetics. The enthalpy profile of DUT-151 int
265 is different in nature compared to the non-interpenetrated MOFs due to the different pore structure and
266 will thus be excluded from the following discussion. Simulated enthalpy profiles of all non-
267 interpenetrated *op* phases are almost identical up to 1.1 kPa where a maximum at $-\Delta_{ads}H_{op} = 14.3$ kJ mol⁻¹
268 is reached. At higher pressures a decrease in $-\Delta_{ads}H_{op}$ is observed reaching a minimum at 11.2 kJ mol⁻¹ at
269 3.7 kPa for DUT-48, $-\Delta_{ads}H = 10.2$ kJ mol⁻¹ at 10.3 kPa for DUT-49, and 9.6 kJ mol⁻¹ at 23 kPa for DUT-
270 50. In this pressure region, the adsorption enthalpies ($-\Delta_{ads}H_{cp}$) of the corresponding *cp* phases are found
271 to decrease with increasing ligand length from 17.8 kJ mol⁻¹ in DUT-48 to 16.7 kJ mol⁻¹ in DUT-50. With
272 increasing ligand length, the adsorbed amount of methane per unit cell at the intersection of the *op* and *cp*
273 isotherm increases from 318 CH₄ per UC (DUT-48), 388 CH₄ per UC (DUT-46), 463 CH₄ per UC (DUT-
274 49), to 596 CH₄ per UC (DUT-50). Consequently, the values of $\Delta\Delta_{ads}H_{total}$ at this point are found to

275 favour structural contraction as they become progressively more exothermic: $-1177 \text{ kJ mol}_{\text{uc}}^{-1}$ (DUT-48),
276 $-2289 \text{ kJ mol}_{\text{uc}}^{-1}$ (DUT-46), $-3491 \text{ kJ mol}_{\text{uc}}^{-1}$ (DUT-49), to $-4458 \text{ kJ mol}_{\text{uc}}^{-1}$ (DUT-50).

277 To derive the impact of different pore sizes on NGA experimentally we analysed at least 6 loadings of
278 CD_4 in a wide pressure range from 0.1 to 20 kPa for DUT-48, -49, and -50 at 111 K and refined the CD_4
279 positions by Rietveld analysis taking single crystal structural data of the guest-free frameworks and
280 complementary computational analysis into account for analysing a multitude of loadings in regions of
281 the isotherms experimentally not accessible due to structural transitions (Figure 5).

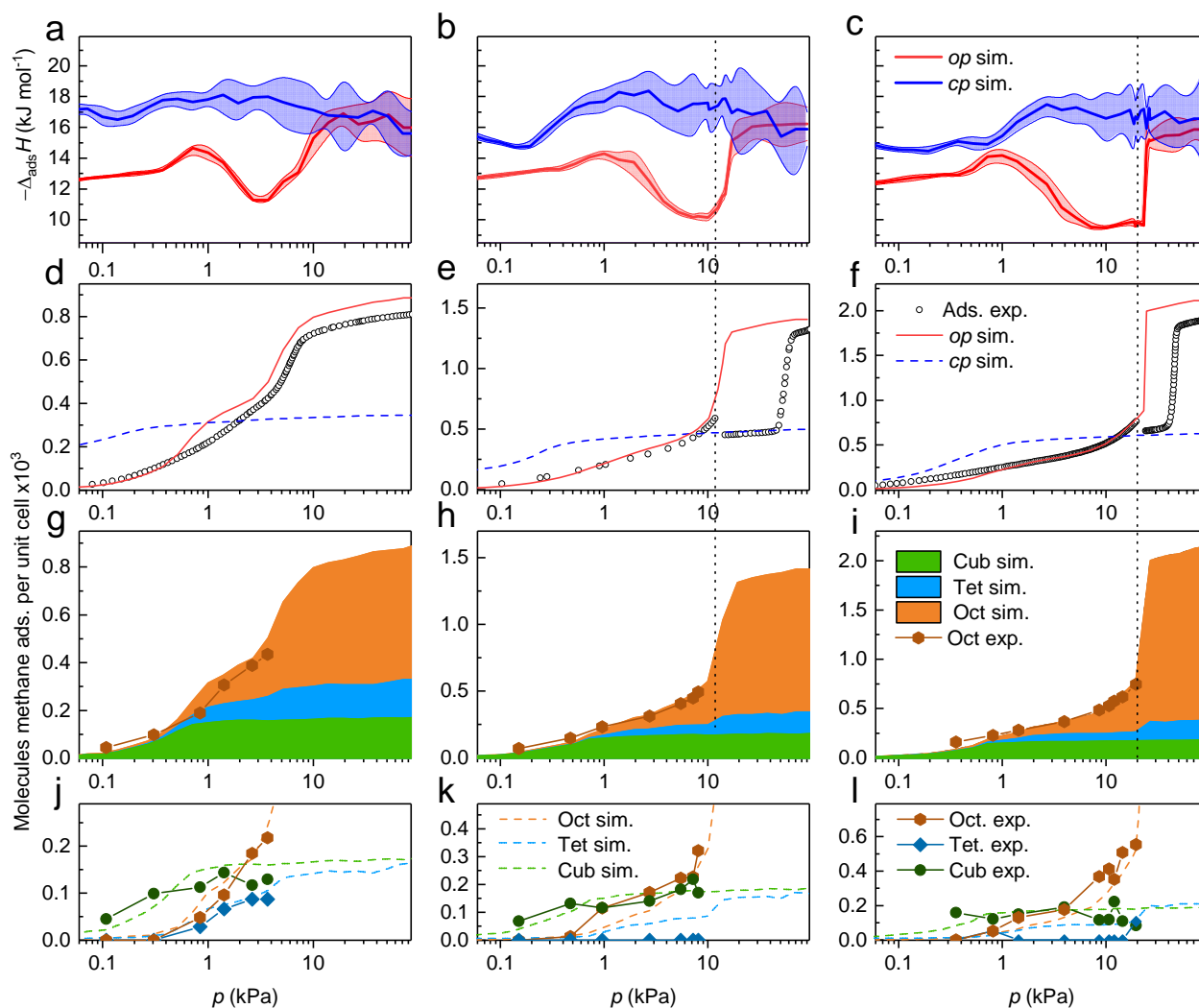


282

283 Figure 5. Methane distribution in DUT-49. **a** Simulated (red circles) and experimental (open symbols) methane adsorption isotherm of DUT-
284 49 at 111 K including points at which NPD patterns were recorded (blue diamonds). **b** Structure of DUT-49 with increasing population of
285 pores with methane upon pressure increase, including on the left trimodal pore system: octahedral (oct, orange), tetrahedral (tet, blue),
286 cuboctahedral (cub, green). Experimentally refined methane positions in light pink, simulated methane density in pink. **c** Visualisation of
287 DUT-49 unit cell at selected loadings which correspond to experimentally investigated pressure. **d** Illustration of methane-filled pores of
288 DUT-49 unit cell in the region of NGA viewed along (100) direction (top), (110) direction (middle), and (111) direction (bottom). For
289 detailed mechanism see supplementary video.

290 The analysis shows that for all three frameworks methane is first adsorbed in the cuboctahedral
291 micropores (cub) identical in size for each of the investigated MOFs. Primary adsorption sites are the
292 open-metal sites inside the cub-pore and its pore windows. This is in line with the analysis of other MOFs
293 with similar structure.⁴³ At higher loadings ($> 300 \text{ CD}_4$ per unit cell), visualization and analysis of
294 adsorption sites in the 3D unit cells becomes challenging due to the large amount of CD_4 molecules.
295 Illustration of the methane positions by methane distribution maps (supplementary video) provide a
296 qualitative picture of the pore filling but make extraction of a quantitative pore filling mechanism
297 difficult. Thus, crystal structures with refined CD_4 positions from Rietveld refinements as well as
298 methane distributions obtained by GCMC analysis were investigated by radial distribution analysis
299 (RDA). This statistical method, in which each methane molecule is assigned to be present in one pore by
300 analysing its distance to the respective pore centre, allows us to dissect isotherms of the *op* phases in

301 separate isotherms for each pore. In the case of DUT-49 and its derivatives a trimodal pore structure
 302 consisting of cuboctahedral (cub, 1.0 nm), tetrahedral (tet, 1.4–2.1 nm), and octahedral (oct, 1.9–
 303 3.1 nm) voids was extracted from the pore size distributions (Supplementary Figure 73) and used as a
 304 model for the analysis of the pore filling. In addition, the extracted single-pore isotherms can be
 305 correlated to the adsorption enthalpy profiles of the *op* phases of DUT-48, -49 and -50 to derive the
 306 adsorption sites responsible for the non-monotonic profile (Figure 6).



307

308 **Figure 6. Analysis of adsorption mechanism.** Columns represent DUT-48 (left), DUT-49 (middle), and DUT-50 (right). **a-c** Adsorption
 309 enthalpy profiles for *op* (red) and *cp* (blue). **d-f** Methane adsorption isotherms at 111 K experimental (circles), simulated for *op* (red) and *cp*
 310 (blue dashed line). **g-i** Stacked simulated isotherms of methane at 111 K for the cuboctahedral (green), tetrahedral (blue), and octahedral
 311 (orange) pores and experimentally obtained isotherms (orange hexagons). **j-l** Comparison of simulated (dashed lines) and experimental
 312 (symbols and solid lines) for the cuboctahedral (dark green), tetrahedral (dark blue), and octahedral (dark orange) pores. Vertical dashed
 313 black lines indicate the region of NGA for DUT-49 and 50.

314 *In situ* NPD and simulations for DUT-48, -49 and -50 revealed the cub voids to be filled first with
 315 methane reaching saturation at around 1 kPa. Thus, the low-pressure adsorption enthalpies are dominated
 316 by solid-fluid interactions in the cub pore and the gradual increase correlates with additional fluid-fluid
 317 interactions upon pore filling. In the range of 0.7 - 2 kPa tet and oct voids are starting to be filled with

318 methane molecules adsorbing on the linker backbone framing these pores. In this region the adsorption
319 enthalpy increases more strongly due to additional solid-fluid interactions reaching a maximum around
320 1.1 kPa where the cub pore reaches saturation. At higher pressures the decrease in adsorption enthalpy
321 can be correlated with reduced solid-fluid interactions due to multilayer adsorption on the surface of the
322 tet and oct voids.

323 Upon NGA ($p_{\text{NGA}}=11.7$ kPa in DUT-49, $p_{\text{NGA}}=19.5$ kPa in DUT-50) neither tet nor oct voids have
324 reached saturation. Interestingly, a steep slope in the isotherm and enthalpy profile which indicates
325 collective pore filling typical for capillary condensation in mesoporous materials^{44,45} is found for both
326 voids in both materials at pressures slightly higher than p_{NGA} . This collective filling is more pronounced
327 for the oct compared to the tet voids due to larger respective pore sizes and shifted towards higher
328 pressures with increasing pore size. Adsorption-induced stress and deformation in mesoporous materials
329 with cylindrical pores typically reaches a maximum in the region of collective pore filling referred to as
330 capillary condensation.⁴⁶ By analysing the evolution of pore size distribution upon contraction for DUT-
331 48 - 151 in the *op* and corresponding *cp* phases, the number of molecules present in the cub and tet voids
332 of the *op* phases and *cp* phases before and after NGA are found to be almost identical. Thus, we can
333 conclude that methane released upon NGA primarily originates from fluid adsorbed in the oct pore, which
334 undergoes the largest reduction in pore volume upon structural contraction. In addition, the performed
335 analysis indicates that the filling of the cub pore does not affect NGA and thus a material with bimodal or
336 possibly monomodal pore system and adaptive pore sizes in the range found for DUT-49 - 151 should
337 demonstrate a similar adsorption mechanism. However, a secondary role of cub pores assisting delayed
338 capillary condensation by hampering molecular guest redistribution cannot be completely ruled out.

339 **Perspective**

340 In this work, we evince NGA as a counterintuitive phenomenon not limited to the single network DUT-
341 49. Systematic linker expansion in an isoreticular series reveals an expanded version, DUT-50, with even
342 higher pore volume and larger pore size to show NGA transitions closely related to those found in DUT-
343 49. The series analysis allows us to derive structural prerequisites from the framework point of view to
344 promote NGA. Two minima in the free energy profile of the empty host corresponding to structures with
345 pronounced porosity differences separated by an activation barrier are a necessary condition for pressure
346 amplifying materials and NGA. Using a combined computational and experimental analysis of the
347 mechanical stability, we conclude linker elongation as a factor reducing the stress required to stimulate
348 structural contraction. Thus, only DUT-49, and -50 show adsorption-induced contraction while the
349 adsorption stress is not high enough to contract the more robust networks DUT-48 and -46. The
350 interpenetrated structure of DUT-151*int* shows detectable adsorption-induced deformation but lacks the
351 free pore volume change and bistability for colossal contraction.

352 Analysis of the adsorption mechanism of methane in DUT-48, -49 and -50 by *in situ* NPD in combination
353 with GCMC methods correlates the filling of the pores and adsorption sites to the adsorption enthalpy
354 profiles. As neither the tet nor the oct voids have reached saturation at p_{NGA} their filling by fluid

355 condensation and contraction is the main reason for NGA transitions. Hence, a pore size above 2 nm is a
356 prerequisite for NGA. Generic computational slit pore models for adsorption-induced deformation in
357 dynamic mesoporous systems support this hypothesis⁴⁷. Methane released during NGA was found to
358 mainly originate from the largest octahedral cavity which implicates their pore volume to correlate with
359 Δn_{NGA} . However, Δn_{NGA} in DUT-50 is found to be lower than in DUT-49 indicating a somewhat
360 decreased activation barrier defining the metastability regime of DUT-50*op*. This difference in activation
361 barrier for the solid transformation can be rationalized considering the lower mechanical stiffness of
362 DUT-50. Hence, an increase of specific pore volume and mechanical stiffness are both equally important
363 to maximize Δn_{NGA} and pressure amplification of mesoporous frameworks in future.

364 **Data availability:** The raw data that support the findings of this study are available from the corresponding author.

365 References

- 366 1 Li, D. & Kaneko, K. Hydrogen bond-regulated microporous nature of copper complex-assembled
367 microcrystals. *Chem. Phys. Lett.* **335**, 50-56 (2001).
- 368 2 Loiseau, T. *et al.* A Rationale for the Large Breathing of the Porous Aluminum Terephthalate
369 (MIL-53) Upon Hydration. *Chem. Eur. J.* **10**, 1373-1382 (2004).
- 370 3 Krause, S. *et al.* A pressure-amplifying framework material with negative gas adsorption
371 transitions. *Nature* **532**, 348-352 (2016).
- 372 4 Hönicke, I. *et al.* Balancing Mechanical Stability and Ultrahigh Porosity in Crystalline Framework
373 Materials. *Angew. Chem. Int. Ed.* **57**, 13780-13783 (2018).
- 374 5 Farha, O. K. *et al.* Metal–Organic Framework Materials with Ultrahigh Surface Areas: Is the Sky
375 the Limit? *J. Am. Chem. Soc.* **134**, 15016-15021 (2012).
- 376 6 Deng, H. *et al.* Large-Pore Apertures in a Series of Metal-Organic Frameworks. *Science* **336**,
377 1018-1023 (2012).
- 378 7 Tan, J. C. & Cheetham, A. K. Mechanical properties of hybrid inorganic-organic framework
379 materials: establishing fundamental structure-property relationships. *Chem. Soc. Rev.* **40**, 1059-
380 1080 (2011).
- 381 8 Chang, Z. *et al.* Flexible Metal–Organic Frameworks: Recent Advances and Potential
382 Applications. *Adv. Mater.* **27**, 5432-5441 (2015).
- 383 9 Schneemann, A. *et al.* Flexible metal-organic frameworks. *Chem. Soc. Rev.* **43**, 6062-6096 (2014).
- 384 10 Ferey, G. Structural flexibility in crystallized matter: from history to applications. *Dalton Trans.*
385 **45**, 4073-4089 (2016).
- 386 11 Horike, S., Shimomura, S. & Kitagawa, S. Soft porous crystals. *Nature Chem.* **1**, 695 (2009).
- 387 12 Van Assche, T. R., Baron, G. V. & Denayer, J. F. Molecular separations with breathing metal-
388 organic frameworks: modelling packed bed adsorbers. *Dalton Trans.* **45**, 4416-4430 (2016).
- 389 13 Sato, H. *et al.* Self-Accelerating CO Sorption in a Soft Nanoporous Crystal. *Science* **343**, 167-170
390 (2014).
- 391 14 Mason, J. A. *et al.* Methane storage in flexible metal–organic frameworks with intrinsic thermal
392 management. *Nature* **527**, 357-361 (2015).

- 393 15 Yang, F. *et al.* A flexible metal–organic framework with a high density of sulfonic acid sites for
394 proton conduction. *Nat. Energy* **2**, 877-883 (2017).
- 395 16 Yanai, N. *et al.* Gas detection by structural variations of fluorescent guest molecules in a flexible
396 porous coordination polymer. *Nat. Mater.* **10**, 787 (2011).
- 397 17 Coudert, F.-X. *et al.* Thermodynamics of Guest-Induced Structural Transitions in Hybrid
398 Organic–Inorganic Frameworks. *J. Am. Chem. Soc.* **130**, 14294-14302 (2008).
- 399 18 Neimark, A. V., Coudert, F.-X., Boutin, A. & Fuchs, A. H. Stress-Based Model for the Breathing
400 of Metal–Organic Frameworks. *J. Phys. Chem. Lett.* **1**, 445-449 (2010).
- 401 19 Salles, F. *et al.* Molecular Dynamics Simulations of Breathing MOFs: Structural Transformations
402 of MIL-53(Cr) upon Thermal Activation and CO₂ Adsorption. *Angew. Chem. Int. Ed.* **47**, 8487-
403 8491 (2008).
- 404 20 Vanduyfhuys, L. *et al.* Thermodynamic insight into stimuli-responsive behaviour of soft porous
405 crystals. *Nat. Commun.* **9**, 204 (2018).
- 406 21 Simon, K. *et al.* A Stimuli-Responsive Zirconium Metal–Organic Framework Based on
407 Supermolecular Design. *Angew. Chem. Int. Ed.* **56**, 10676-10680 (2017).
- 408 22 Rogge, S. M. J., Waroquier, M. & Van Speybroeck, V. Reliably Modeling the Mechanical
409 Stability of Rigid and Flexible Metal–Organic Frameworks. *Acc. Chem. Res.* **51**, 138-148 (2018).
- 410 23 Eddaoudi, M. *et al.* Systematic Design of Pore Size and Functionality in Isoreticular MOFs and
411 Their Application in Methane Storage. *Science* **295**, 469-472 (2002).
- 412 24 Surble, S. *et al.* A new isoreticular class of metal-organic-frameworks with the MIL-88 topology.
413 *Chem. Commun.*, 284-286 (2006).
- 414 25 Ramsahye, N. A. *et al.* Influence of the Organic Ligand Functionalization on the Breathing of the
415 Porous Iron Terephthalate Metal Organic Framework Type Material upon Hydrocarbon
416 Adsorption. *J. Phys. Chem. C* **115**, 18683-18695 (2011).
- 417 26 Horcajada, P. *et al.* How Linker’s Modification Controls Swelling Properties of Highly Flexible
418 Iron(III) Dicarboxylates MIL-88. *J. Am. Chem. Soc.* **133**, 17839-17847 (2011).
- 419 27 Munn, A. S. *et al.* The flexibility of modified-linker MIL-53 materials. *Dalton Trans.* **45**, 4162-
420 4168 (2016).
- 421 28 Stoeck, U. *et al.* A highly porous metal-organic framework, constructed from a cuboctahedral
422 super-molecular building block, with exceptionally high methane uptake. *Chem. Commun.* **48**,
423 10841-10843 (2012).
- 424 29 Evans, J. D., Bocquet, L. & Coudert, F.-X. Origins of Negative Gas Adsorption. *Chem* **1**, 873-886
425 (2016).
- 426 30 Schaber, J. *et al.* In Situ Monitoring of Unique Switching Transitions in the Pressure-Amplifying
427 Flexible Framework Material DUT-49 by High-Pressure ¹²⁹Xe NMR Spectroscopy. *J. Phys.*
428 *Chem. C* **121**, 5195-5200 (2017).
- 429 31 Krause, S. *et al.* The effect of crystallite size on pressure amplification in switchable porous
430 solids. *Nat. Commun.* **9**, 1573 (2018).
- 431 32 Krause, S. *et al.* Adsorption Contraction Mechanics: Understanding Breathing Energetics in
432 Isoreticular Metal–Organic Frameworks. *J. Phys. Chem. C* **122**, 19171-19179 (2018).
- 433 33 Nazarian, D. *et al.* Large-Scale Refinement of Metal–Organic Framework Structures Using
434 Density Functional Theory. *Chem. Mater.* **29**, 2521-2528 (2017).

- 435 34 Li, S., Chung, Y. G. & Snurr, R. Q. High-Throughput Screening of Metal–Organic Frameworks
436 for CO₂ Capture in the Presence of Water. *Langmuir* **32**, 10368-10376 (2016).
- 437 35 Agrawal, M., Sava Gallis, D. F., Greathouse, J. A. & Sholl, D. S. How Useful Are Common
438 Simulants of Chemical Warfare Agents at Predicting Adsorption Behavior? *J. Phys. Chem. C* **122**,
439 26061-26069 (2018).
- 440 36 Pulido, A. *et al.* Functional materials discovery using energy–structure–function maps. *Nature*
441 **543**, 657 (2017).
- 442 37 Bureekaew, S. *et al.* MOF-FF – A flexible first-principles derived force field for metal-organic
443 frameworks. *Phys. Status Solidi B* **250**, 1128-1141 (2013).
- 444 38 Weseliński, Ł. J., Luebke, R. & Eddaoudi, M. A Convenient Preparation of 9H-Carbazole-3,6-
445 dicarbonitrile and 9H-Carbazole-3,6-dicarboxylic Acid. *Synthesis* **46**, 596-599 (2014).
- 446 39 Simon, C. M. *et al.* Optimizing nanoporous materials for gas storage. *Phys. Chem. Chem. Phys.*
447 **16**, 5499-5513 (2014).
- 448 40 Wu, H., Zhou, W. & Yildirim, T. Methane Sorption in Nanoporous Metal–Organic Frameworks
449 and First-Order Phase Transition of Confined Methane. *J. Phys. Chem. C* **113**, 3029-3035 (2009).
- 450 41 Wu, H. *et al.* Metal-Organic Frameworks with Exceptionally High Methane Uptake: Where and
451 How is Methane Stored? *Chem. Eur. J.* **16**, 5205-5214 (2010).
- 452 42 Getzschmann, J. *et al.* Methane storage mechanism in the metal-organic framework Cu₃(btc)₂: An
453 in situ neutron diffraction study. *Microporous Mesoporous Mater.* **136**, 50-58 (2010).
- 454 43 Rowland, C. A. *et al.* Methane Storage in Paddlewheel-Based Porous Coordination Cages. *J. Am.*
455 *Chem. Soc.* **140**, 11153-11157 (2018).
- 456 44 Wang, Y., Do, D. D. & Nicholson, D. Study of heat of adsorption across the capillary
457 condensation in cylindrical pores. *Colloids Surf. A* **380**, 66-78 (2011).
- 458 45 Horikawa, T., Do, D. D. & Nicholson, D. Capillary condensation of adsorbates in porous
459 materials. *Adv. Colloid Interface Sci.* **169**, 40-58 (2011).
- 460 46 Gor, G. Y., Huber, P. & Bernstein, N. Adsorption-induced deformation of nanoporous materials—
461 A review. *Appl. Phys. Rev.* **4**, 011303 (2017).
- 462 47 Jack D., E. *et al.* Exploring the Thermodynamic Criteria for Responsive Adsorption Processes.
463 Preprint at
464 https://chemrxiv.org/articles/Exploring_the_Thermodynamic_Criteria_for_Responsive_Adsorption_Processes/7527680
465 (2018).
- 466

467 Acknowledgements

468 This project has received funding from the European Research Council (ERC) under the European
469 Union’s Horizon 2020 research and innovation programme (grant agreement No. 742743). The authors
470 thank the BMBF (No. 05K16OD1) and ANR/DFG Program FUN for financial support and Helmholtz-
471 Zentrum Berlin für Materialien und Energie for allocated beam time at KMC-2 (*in situ* PXRD), MX
472 BL14.3 (single crystal X-ray diffraction) beamlines of BESSY-II, E9 (FIREPOD) neutron powder
473 diffractometer (*in situ* NPD) of BER-II and travel funding. Furthermore, the MADIREL authors have
474 received funding from the European Union's Horizon 2020 research and innovation programme under the

475 Marie Sklodowska-Curie grant agreement No 641887 (project acronym: DEFNET). G.M. thanks Institut
476 Universitaire de France for its support.

477 **Author contributions:** S. Krause synthesized, activated and performed characterization of organic
478 ligands and MOF samples. E. Troschke contributed to the synthesis of organic ligands. S. Krause, V. Bon,
479 D. Wallacher, and D. M. Többens contributed to *in situ* PXRD measurements. S. Krause, V. Bon, D.
480 Wallacher, and A. Franz contributed to *in situ* NPD measurements. V. Bon performed refinement of SCD
481 and PXRD data. J. Getzschmann performed refinement of NPD data. S. Krause, V. Bon, I. Senkovska and
482 S. Kaskel contributed to analysis, interpretation and discussion of adsorption and single crystal X-ray
483 diffraction data. F. Kolbe and E. Brunner performed and discussed NMR data. P. Iacomi and P. Llewellyn
484 performed and analysed *in situ* calorimetry experiments. P. G. Yot and G. Maurin performed, analysed
485 and interpreted the mercury intrusion experiments. J. D. Evans and F.-X. Coudert performed
486 computational analysis of mechanical and adsorption properties. S. Ehrling performed SEM analysis. S.
487 Krause, V. Bon, J. D. Evans and S. Kaskel organized the project. All authors contributed to writing and
488 improving the manuscript.

489 **Additional information:** Supplementary Information accompanies this paper at (to be filled in by editor)

490 **Competing interests:** The Authors declare no Competing Financial or Non-Financial Interests.

491 **Affiliations**

492 **1** Faculty of Chemistry and Food Chemistry, TU Dresden, Bergstrasse 66, 01062 Dresden, Germany.

493 **2** Chimie ParisTech, PSL Research University, CNRS, Institut de Recherche de Chimie, Paris, 75005
494 Paris, France.

495 **3** Aix-Marseille Univ., CNRS, MADIREL (UMR 7246), 13013 Marseille, France.

496 **4** Helmholtz-Zentrum Berlin für Materialien und Energie, Hahn- Meitner-Platz 1, 14109 Berlin,
497 Germany.

498 **5** Institut Charles Gerhardt Montpellier UMR 5253 Univ. Montpellier CNRS UM ENSCM, Université de
499 Montpellier, Place Eugène Bataillon, 34095 Montpellier cedex 05, France.

500

501

502

Krause et al - Towards NGA design - manuscript.pdf (1.12 MiB)

[view on ChemRxiv](#) • [download file](#)

Methane adsorption in DUT-49 at 111 K

Krause et al. Supplementary video.gif (27.67 MiB)

[view on ChemRxiv](#) • [download file](#)

Supplementary Information for

Towards general network architecture design criteria for negative gas adsorption transitions in ultraporous frameworks

1 Chemicals and Methods

1.1 Chemicals and Gases

All materials and gases used in the synthesis and analysis in this study were of high purity as summarized in Supplementary Table 1.

Supplementary Table 1. List of chemicals used for the synthesis of ligands and MOFs.

Name	CAS	purity	Manufacturer
1,1'-Ferrocenediyl-bis(diphenylphosphine)	12150-46-8	99%	Alfa Aesar
2,6-Dibromonaphthalene	13720-06-4	99%	ABCR
4,4''-Dibromo- <i>p</i> -terphenyl	17788-94-2	n.a.	Sigma Aldrich
4,4'-Diiodobiphenyl	3001-15-8	99%	Alfa Aesar
4-Bromophenylboronic acid	5467-74-3	99%	TCI
9 <i>H</i> -Carbazole	86-74-8	>95%	Sigma Aldrich
Acetic acid	64-19-7	99.9%	Roth
Bis(dibenzylideneacetone)palladium(II)	32005-36-0	99%	Sigma Aldrich
Copper(I) iodide	7681-65-4	99%	Riedel-de Haen
Copper(II) nitrate trihydrate	10031-43-3	98%	Sigma Aldrich
Hydrochloric acid	7647-01-0	37%	Sigma Aldrich
<i>L</i> -Proline	147-85-3	99%	Sigma Aldrich
<i>N,N'</i> -Ethylenediamine	107-15-3	99%	Alfa Aesar
<i>N,N'</i> -Dimethylethylenediamine	110-70-3	99%	Alfa Aesar
<i>N,N</i> -Dimethylformamide (DMF)	68-12-2	99%	Fischer Scientific
<i>N</i> -Bromosuccinimide	128-08-5	99%	Sigma Aldrich
Potassium hydroxyde	1310-58-3	95%	Fischer Scientific
Potassium carbonate	584-08-7	99%	Grüssing
Sodium hydroxyde	1310-73-2	98.5%	Fischer Scientific
Sulfuric acid	7664-93-9	99%	Alfa Aesar
Tetrakis(triphenylphosphine)palladium(0)	14221-01-3	99%	Sigma Aldrich
Zinc cyanide	557-21-1	98%	Sigma Aldrich

1.2 Instruments and Methods

1.2.1 Solution/liquid-state NMR

Nuclear magnetic resonance (NMR) spectra were acquired on a BRUKER Avance III 500 spectrometer (500.13/600.16 MHz and 125.77/150.91 MHz for ^1H and ^{13}C respectively) and/or on a VARIAN Mercury (300 MHz, 282 MHz and 75.5 MHz for ^1H and ^{13}C , respectively). All ^1H and ^{13}C NMR spectra are reported in parts per million (ppm) downfield of TMS and were measured relative to the residual signals of the solvents at 7.26 ppm (CHCl_3) or 2.54 ppm (DMSO). Data for ^1H NMR spectra are described as following: chemical shift (δ (ppm)), multiplicity (s, singlet; d, doublet; t, triplet; q, quartet; m, multiplet; br, broad signal), coupling constant J (Hz), integration corresponding to amount of C or CH. Data for ^{13}C NMR spectra are described in terms of chemical shift (δ (ppm)) and functionality were derived from DEPT spectra.

1.2.2 Mass spectrometry

Matrix-assisted laser desorption/ionization (MALDI) time of flight (TOF) mass spectrometry analysis was performed on a BRUKER Autoflex Speed MALDI TOF MS using dithranol as matrix. Atmospheric-pressure solid analysis probe (ASAP) mass spectrometry was performed on an ADVION expression LCMS with an APCI ion source.

1.2.3 Elemental analysis

Elemental analysis was carried out by Philipp Lange (Institut für Anorganische Molekülchemie, Technische Universität Dresden) on a VARIO MICRO-cube Elemental Analyzer by Elementar Analysatorsysteme GmbH in CHNS modus. The composition was determined as the average of three individual measurements on three individually prepared samples.

1.2.4 DRIFT Spectroscopy

Diffuse reflectance infrared Fourier transform (DRIFT) spectroscopy was performed on a BRUKER VERTEX 70 with a SPECAC Golden Gate DRIFT setup. Prior to the measurement 2 mg of sample were mixed with 10-15 mg dry KBr in a mortar and pressed in the DRIFT-cell. Assignments of peaks in wavenumber ν (cm^{-1}) were categorized by strong (s), medium (m), weak (w).

1.2.5 Thermogravimetric analysis

Thermal analysis (TGA) was carried out in synthetic dry air using a NETZSCH STA 409 thermal analyser at a heating rate of 5 K min^{-1} . Air sensitive MOF samples were prepared in an Ar-filled glovebox and inserted in the instrument with little exposure to ambient conditions.

1.2.6 X-Ray Diffraction

Powder X-ray diffraction (PXRD) patterns were collected in transmission geometry with a STOE STADI P diffractometer operated at 40 kV and 30 mA with monochromatic Cu-K α_1 ($\lambda = 0.15405$ nm) radiation, a scan speed of 30 - 15 s/step and a detector step size of $2\theta = 0.1 - 2^\circ$. The samples were placed between non-diffracting adhesive tape or in a glass capillary. "As made" samples were analysed while suspended in DMF. Desolvated samples were prepared under inert atmosphere. Theoretical PXRD patterns were calculated on the basis of crystal structures using Mercury 3.9 software package.

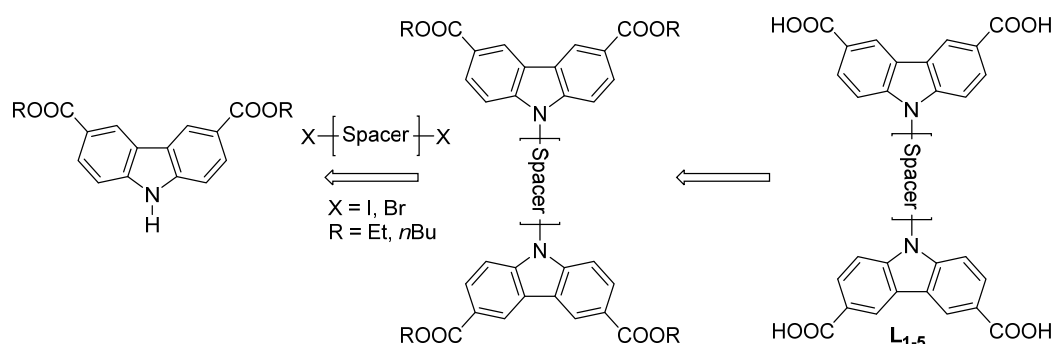
1.2.7 SEM analysis of crystal size and morphology

Scanning electron microscopy (SEM) images of DUT-49 were taken with secondary electrons in a HITACHI SU8020 microscope using 1.0 kV acceleration voltage and 10.8 mm working distance. The powdered samples were prepared on a sticky carbon sample holder. To avoid degradation upon exposure to air, the samples were prepared under argon atmosphere. For each sample a series of images was recorded at different magnifications and for each sample three different spots on the sample holder were investigated. The crystal size refers to the edge length of the cubic crystals as they are the easiest to measure. The analysis of the SEM images was performed with ImageJ Software package.¹ Values for mean crystal size, as well as relative standard deviation (RSD) were obtained by using the ImageJ Analyse-Distribution function.

2 Synthesis of Organic Ligands

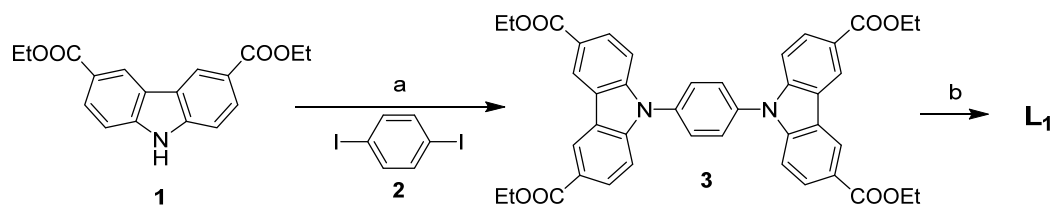
2.1 Synthetic approach

Attempts to synthesize L₃-derived ligands by using the synthesis conditions previously used to synthesize L₃ involving lithiation and subsequent carboxylation proved difficult for synthesizing the proposed series of ligands mainly due to low solubility of the bromides and low yields. Thus, we decided to apply a different synthetic pathway (Supplementary Figure 1).



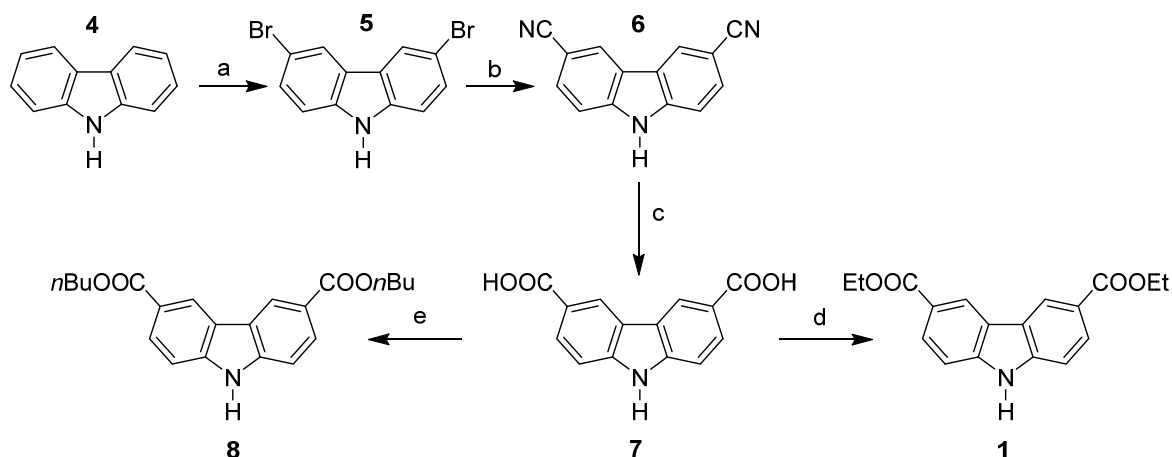
Supplementary Figure 1. Retrosynthesis for the construction of L₁-derived ligands with different spacer units.

The same approach was previously used in the synthesis of L_1 in DUT-48² and PCN-81^{3,4} (Supplementary Figure 2).



Supplementary Figure 2. Reaction sequence used to synthesize L_1 : a) CuI, K_2CO_3 , *L*-proline, 90-110°C, 1-8 d, b) KOH, THF, H_2O , 90 °C, 24 h.

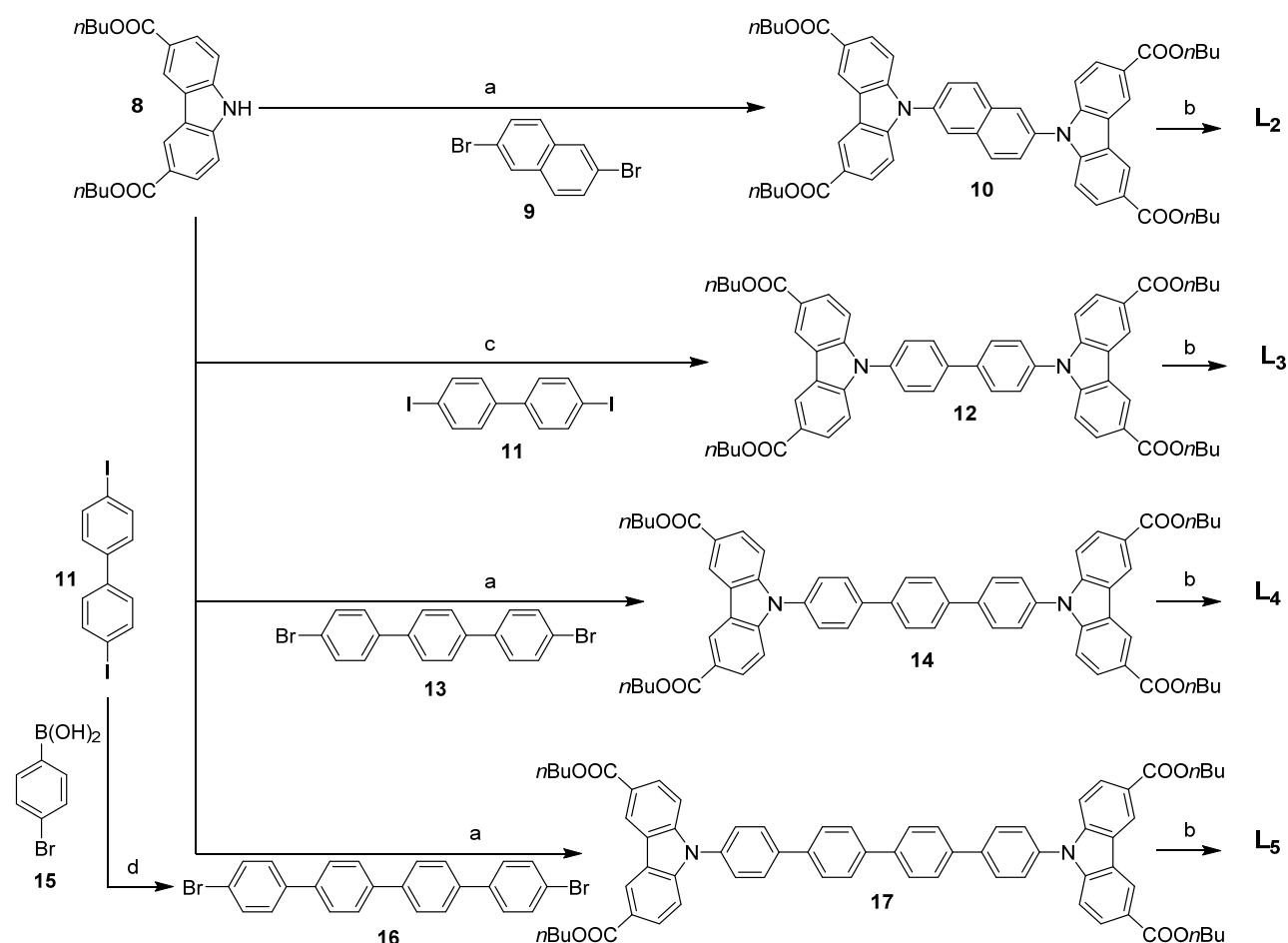
However, the initially used procedure to synthesise ester **1** showed low yield and difficulties towards upscaling required for the synthesis of 5 different derivatives. Thus, we decided to use a protocol established by Eddaoudi et al.⁵ developed to synthesize the carboxylic acid **7** in large quantities and high yields by hydrolysis of the corresponding cyanide which can be synthesized on large scale in two steps based on the commercially available, inexpensive 9*H*-carbazole (**4**).



Supplementary Figure 3. Reaction sequence for the synthesis of ester **1** and **8**. a) *N*-Bromosuccinimide, THF, 30 °C, 24 h, b) $ZnCN_2$, ZnOAc, Pd(dba)₃, 1,1'-Bis(diphenylphosphino)ferrocene, DMF, 100 °C, 72 h, c) CuI (cat.), NaOH, H_2O , 130 °C, 24 h, d) ethanol, H_2SO_4 (cat.), 85 °C, 18 h, e) *n*-butanol, H_2SO_4 (cat.), 130 °C, 48 h.

By esterification with ethanol ester **1** could be obtained in overall higher yields than the previously reported procedure and the reaction sequence allows for easier upscaling. However, attempts to synthesize L_2 and L_3 by using the ethyl ester **1** as starting material lead to the formation of the mono-coupled product which precipitated from the reaction mixture and demonstrated low solubility in DMSO and DMF. To overcome these limits of solubility we decided to substitute ethyl by *n*-butyl groups which should in general support solubility. By esterification with *n*-butanol, the *n*-butyl ester **8** could be obtained on the scale of 45 g product and overall yield of 71% over four steps. When reacted with iodide **11** via Cu-catalysed Ullmann-coupling in DMF, potassium carbonate as base and *N,N'*-dimethylethylenediamine to stabilize the catalyst at 120 °C the *n*-butyl ester **12** could be obtained with 43% yield in contrast to the

previous unsuccessful synthesis using the ethyl ester **1**. The Cu-based Ullman coupling reaction was found to be the most efficient and cheapest method in contrast to Pd-based catalysts. The following reaction sequences were used to synthesize L₂-L₅ (Supplementary Figure 4).

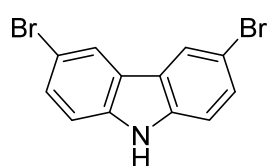


Supplementary Figure 4. Scheme for the synthesis of ligands L₁ – L₅. a) CuI, K₂CO₃, DMF, *N,N'*-dimethyl ethylenediamine, 90-110°C, 1-8 d, b) KOH, THF, H₂O, 90 °C, 24 h, c) CuI, K₂CO₃, DMSO, *L*-proline, 90-110°C, 1-8 d, d) tetrakis(triphenylphosphine)palladium(0), K₂CO₃, toluene, H₂O, 100 °C, 24 h.

Based on whether the coupling reaction was performed with an iodide or bromide, reaction conditions were adjusted. Detailed description on all reactions can be found in the following:

2.2 Synthesis of 9H-Carbazole Building Blocks

2.2.1 3,6-Dibromo-9H-carbazole



A 1 l flask was charged with 60 g (0.36 mol) 9H-carbazole which was previously recrystallized from a mixture of 900 ml toluene and 100 ml ethanol and dissolved in 800 ml anhydrous THF. To the solution 140 g (0.79 mol) *N*-bromosuccinimide was added over 30 min at room temperature and the solution was stirred for 28 h at 30 °C. The THF was removed in vacuum, the remaining solid dissolved in diethyl ether, and the solution extracted with water. The organic phases were collected, dried over MgSO₄ and the solvent

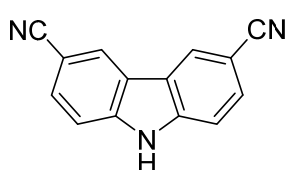
removed in vacuum. The yellow powder was recrystallized from a mixture of 800 ml chloroform and 50 ml diethyl ether and dried in vacuum to yield 103 g (89%) of white product.

^1H NMR (500 MHz, CHLOROFORM-*d*) δ (ppm): 7.33 (d, $J=8.51$ Hz, 2 H) 7.53 (dd, $J=8.51, 1.89$ Hz, 2 H) 8.15 (d, $J=1.89$ Hz, 2 H) 8.33 (br. s., 1 H).

^{13}C NMR (151 MHz, CHLOROFORM-*d*) δ ppm 111.34 (s, 1 C) 113.69 (s, 1 CH) 123.45 (s, 1 CH) 123.99 (s, 1 C) 128.87 (s, 1 CH) 138.91 (s, 1 CH).

ASAP-MS (m/z): Calculated for $\text{C}_{12}\text{H}_7\text{Br}_2\text{N}$: 324; found: 324 $[\text{M}-\text{H}]^+$.

2.2.2 9H-Carbazole-3,6-dicarbonitrile



Due to the high toxicity of cyanide the reaction was performed in a sealed fume hood. Deactivation of glassware and tools used for the reaction were performed in a 5% H_2O_2 solution containing ammonia with a pH higher than 11. A 500 ml Schlenk flask was charged with 80 g (246 mmol) of bromide **5** and 656 mg (0.59 mmol) 1,1'-bis(diphenylphosphino)ferrocene. The flask was evacuated, flushed with Ar, and 250 ml DMF and 2.4 ml water were added. In a glovebox a flask with 640 mg (9.9 mmol) Zn powder, 34.5 g (294 mmol) anhydrous zinc cyanide, 1.8 g (9.8 mmol) zinc acetate, and 460 mg (0.5 mmol) bis(dibenzylideneacetone)palladium(0) was prepared and the reactants added to the Schlenk flask. The reaction mixture was stirred at 100 °C for 72 h. Afterwards the brown suspension was cooled to room temperature and poured into an aqueous solution of 400 ml saturated ammonium chloride solution and 400 ml concentrated ammonia solution. The off-white precipitate was filtered off and washed with the same amount of previously described aqueous solution followed by thorough washing with water. The waste solutions were collected and deactivated as described above. The off-white powder was dried, washed twice with 20 ml methanol, twice with 30 ml toluene, and dried in vacuum. The solid was recrystallized from DMF to yield 48.2 g (90%) of the white product.

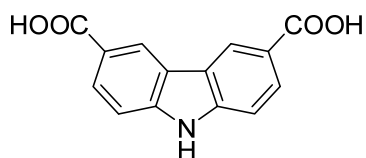
^1H NMR (500 MHz, DMSO-*d*₆) δ (ppm): 7.72 (d, $J=8.51$ Hz, 2 H) 7.85 (dd, $J=8.20, 1.58$ Hz, 2 H) 8.79 (s, 2 H) 12.38 (s, 1 H).

^{13}C NMR (151 MHz, DMSO-*d*₆) δ ppm 101.59 (s, 1 CH) 112.69 (s, 1 CH) 119.95 (s, 1 C) 121.69 (s, 1 C) 126.26 (s, 1 CH) 129.77 (s, 1 CH) 142.16 (s, 1 C).

MS-ASAP (m/z): Calculated for $\text{C}_{14}\text{H}_7\text{N}_3$: 218; found: 218 $[\text{M}+\text{H}]^+$.

Elemental analysis: Calculated: C: 77.41%; H: 3.25%; N: 19.34%; found: C: 78.19%; H: 3.056%; N: 19.47%.

2.2.3 9H-Carbazole-3,6-dicarboxylic acid



In a 2 l flask 30 g (0.13 mol) cyanide **6**, 90 g (2.25 mol) sodium hydroxide, and 300 mg (1.58 mmol) copper (I) iodide were dissolved in 1 L water and stirred under reflux for 24 h. the solution was cooled down to room temperature and filtered over Celite[®]. The solution was neutralized with 6 M hydrochloric acid, the white precipitate was filtered off, washed thoroughly with water, and dried at 80 °C to yield 33 g (93%) off-white powder.

^1H NMR (500 MHz, $\text{DMSO-}d_6$) δ ppm 7.57 (d, $J=8.51$ Hz, 2 H) 8.03 (dd, $J=8.51$, 1.89 Hz, 2 H) 8.79 - 8.85 (m, 2 H) 12.02 (s, 1 H)

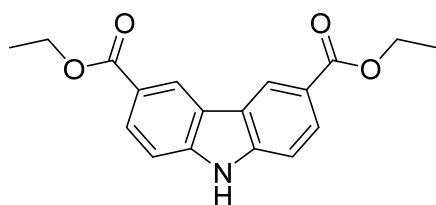
^{13}C NMR (126 MHz, $\text{DMSO-}d_6$) δ ppm 11.121 (s, 1 CH), 122.03 (s, 1 C) 122.33 (s, 1 C) 122.95 (s, 1 CH) 127.80 (s, 1 CH) 143.26 (s, 1 C) 167.07 (s, 1 C) 168.82 (s, 1 C).

MS-ASAP (m/z): Calculated for $\text{C}_{14}\text{H}_9\text{NO}_4$: 256; found: 256 $[\text{M}+\text{H}]^+$.

Elemental analysis: Calculated ($\text{C}_{14}\text{H}_9\text{NO}_4 \cdot 0.55 \cdot \text{H}_2\text{O}$): C: 63.42%; H: 3.84%; N: 5.28%; found: C: 63.44%; H: 3.681%; N: 5.08%.

DRIFT, KBr, 298 K (cm^{-1}): 3471 (w), 2823 (w), 2644 (w), 1913 (w), 1789 (m), 1681 (s), 1633 (m), 1606 (s), 1585 (m), 1491 (w), 1470 (m), 1451 (m), 1419 (s), 1354 (m), 1288 (s), 1254 (s), 1217 (m), 1137 (w), 1024 (m), 931 (m), 898 (m), 851 (w), 828 (m), 802 (w), 769 (s), 724 (m), 682 (w).

2.2.4 Diethyl 9H-carbazole-3,6-dicarboxylate



In a 250 ml flask 3 g (11.7 mmol) H_2CDC **1** was suspended in 150 ml ethanol and 1 ml of sulfuric acid was added. The mixture was refluxed at 85 °C for 18 h to form a clear yellow solution. The ethanol was removed in vacuum, the resulting solid dissolved in chloroform, and extracted with diluted aqueous potassium carbonate solution. The

organic phases were combined, dried over MgSO_4 and the solvent removed in vacuum to obtain 3.3 g (91%) white powder.

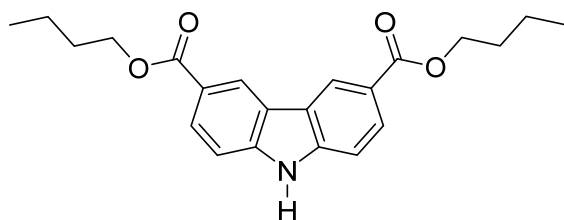
^1H NMR (500 MHz, $\text{CHLOROFORM-}d$) δ (ppm): 1.48 (t, $J=7.09$ Hz, 3 H) 4.46 (q, $J=7.25$ Hz, 2 H) 7.48 (d, $J=8.51$ Hz, 2 H) 8.20 (dd, $J=8.51$, 1.58 Hz, 2 H) 8.58 (br. s., 1 H) 8.88 (d, $J=1.26$ Hz, 2 H).

^{13}C -NMR (150 MHz, $\text{DMSO-}d_6$): δ (in ppm): 14.38 (1 CH_3), 60.39 (1 CH_2), 111.31 (1 CH), 121.24 (1 C), 122.29 (1 C), 122.77 (1 CH), 127.46 (1 CH), 143.25 (1 C), 166.33 (1 C).

MALDI-TOF-MS (m/z): Calculated for $\text{C}_{18}\text{H}_{17}\text{NO}_4$: 266; found 266 $[\text{M}-\text{C}_2\text{H}_5\text{OH}]^+$.

Elemental analysis: Calculated: C: 69.44%; H: 5.5%; N: 4.5%; found: C: 68.73%; H: 5.299%; N: 4.5%.

2.2.5 Dibutyl 9H-carbazole-3,6-dicarboxylate



In a 1 l flask 33 g (0.13 mmol) H_2CDC **1** was suspended in 750 ml 1-butanol and 3 ml of sulfuric acid was added. The mixture was refluxed at 130 °C for 48 h to form a clear yellow solution. The 1-butanol was removed in vacuum, the resulting solid dissolved in chloroform, and extracted with

diluted aqueous potassium carbonate solution. The organic phases were combined, dried over MgSO_4 and the solvent removed in vacuum. The obtained solid was recrystallized from ethyl acetate to obtain 45 g (95%) white powder.

^1H NMR (600 MHz, $\text{CHLOROFORM-}d$) δ (ppm): 1.04 (t, $J=7.34$ Hz, 6 H) 1.51 - 1.60 (m, 4 H) 1.81 - 1.88 (m, 4 H) 4.41 (t, $J=6.59$ Hz, 4 H) 7.48 (d, $J=8.28$ Hz, 2 H) 8.19 (dd, $J=8.47$, 1.69 Hz, 2 H) 8.57 (br. s., 1 H) 8.87 (d, $J=1.51$ Hz, 2 H).

^{13}C NMR (151 MHz, $\text{CHLOROFORM-}d$) δ (ppm): 13.83 (s, 1 CH_3) 19.36 (s, 1 CH_2) 30.93 (s, 1 CH_2) 64.82 (s, 1 CH_2) 110.47 (s, 1 CH) 122.75 (s, 1 C) 123.04 (s, 1 CH) 123.14 (s, 1 C) 128.13 (s, 1 CH) 142.66 (s, 1 C) 167.20 (s, 1 C).

MALDI-TOF-MS (m/z): Calculated for C₃₆H₂₀Br₄N₂: 294; found 294 [M-C₄H₉OH]⁺.

Elemental analysis: Calculated: C: 71.91%; H: 6.86%; N: 3.81%; found: C: 72.01%; H: 6.443%; N: 3.68%.

2.3 Synthesis of L₃ and analogues

2.3.1 General procedure of Ullman coupling

The general synthesis of ligands derived from H₂CDC is based on Ullmann coupling of the esters **8** or **1** with different iodides and bromines. The following procedures were used:

Ullmann Coupling with iodides

This procedure is based on syntheses previously used for carbazole based ligands⁶. A Schlenk flask was charged with indicated amounts of ester **8**, the corresponding iodide, potassium carbonate, copper (I) iodide, and *L*-proline under inert atmosphere. To the mixture indicated amounts of degassed DMSO or DMF were given and Ar was bubbled through the suspension for 30 min. The reaction mixture was stirred at 90 – 120 °C for 24 h to 10 d and the reaction was cooled down to room temperature. The suspension was quenched with diluted (< 0.02 M) hydrochloric acid and extracted with chloroform. The organic phases were collected, dried over MgSO₄, and the solvent removed in vacuum. The crude product was purified by flash column chromatography using indicated mixtures of chloroform, DCM, *iso*-hexane and ethyl acetate. Corresponding amounts of the chemicals added and used for the synthesis and purification are provided for each coupling product.

Ullmann Coupling with bromides

This procedure is based on syntheses previously used for carbazole based ligands⁴. A Schlenk flask was charged with indicated amounts of ester **8**, the corresponding bromide, potassium carbonate, copper (I) iodide, and *N,N'*-dimethylethylenediamine under inert atmosphere. To the mixture indicated amounts of degassed anhydrous 1,4-dioxane were given and Ar was bubbled through the suspension for 30 min. The reaction mixture was stirred at 80 – 110 °C for 24 h to 12 d and the reaction was cooled down to room temperature. The solvent was removed in vacuum and the obtained powder was dissolved in chloroform and extracted with diluted (< 0.02 M) hydrochloric acid. The organic phases were collected, dried over MgSO₄, and the solvent removed in vacuum. The crude product was purified by flash column chromatography using indicated mixtures of chloroform, DCM, *iso*-hexane and ethyl acetate. Corresponding amounts of the chemicals added and used for the synthesis and purification, reaction times and temperatures are provided for each coupling product.

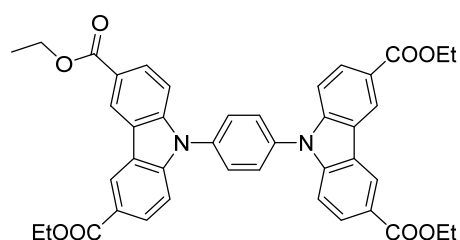
2.3.2 General procedure for ester hydrolysis

To hydrolyse the ester groups the corresponding coupling products were dissolved in indicated volumes of THF, methanol, and water at 85 °C. To the solution potassium hydroxide was added and the mixture was stirred at 85 °C for 12 h– 5 d. In case a precipitate formed from the previous clear solution (most

likely the potassium salt of the hydrolysed ester which is insoluble in THF) small amounts of water were added until a clear solution formed again. After the indicated reaction time THF and methanol were removed in vacuum, the resulting solution was filtered, and neutralized with 2 M hydrochloric acid. The precipitate was filtered off and dried in vacuum at room temperature. Corresponding amounts of the chemicals added and reaction times are provided for each hydrolysis product.

2.4 Variation of ligand length

2.4.1 Tetraethyl 9,9'-(1,4-phenylene)bis(9H-carbazole-3,6-dicarboxylate)



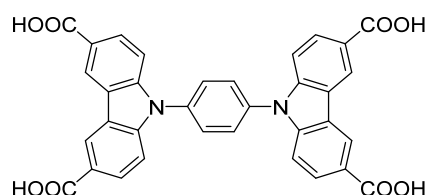
Synthesis conditions: 4.5 g (14.4 mmol) ethylester **1**, 2.16 mg (0.74 mmol) 4,4'-diiodophenyl, 3.63 g (26.3 mmol) potassium carbonate, 250 mg (1.31 mmol) copper(I) iodide, 104 mg (2.62 mmol) *L*-proline, 80 ml DMSO, 85 °C for 24 h and 95 °C for 48 h; Recrystallized from ethyl acetate.

Yield: 3 g (65%) white powder.

¹H-NMR (500 MHz, DMSO-*d*₆): δ (ppm): 1.38 (tr, *J* = 7.0 Hz, 6 H), 4.33 (q, *J* = 7.0 Hz, 4 H), 7.65 (dd, *J* = 8.5 Hz, *J* = 0.6 Hz, 2 H), 8.11 (dd, *J* = 8.5 Hz, *J* = 1.7, 2 H), 8.89 (dd, *J* = 1.7 Hz, *J* = 0.6 Hz, 2 H), 12 (s, 1 H).

¹³C-NMR (150 MHz, DMSO-*d*₆): δ (ppm): 14.34 (1 CH₃), 60.39 (1 CH₂), 111.35 (1 CH), 121.25 (1 C), 122.29 (1 C), 122.71 (1 CH), 127.486 (1 CH), 143.25 (1 C), 166.39 (1 C).

2.4.2 9,9'-(1,4-phenylene)bis(9H-carbazole-3,6-dicarboxylic acid)



Synthesis conditions: 3 g (4.31 mmol) ester **3**, 1.44 g (20.7 mmol) potassium hydroxide, 115 ml THF, 3 ml methanol, 50 ml H₂O, 75 °C for 2 d.

Yield: 2.35 g (93%) white powder.

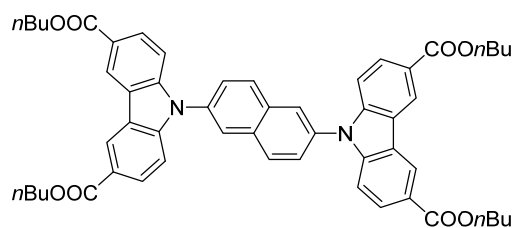
¹H NMR (500 MHz, DMSO-*d*₆) δ (ppm): 7.68 (d, *J*=8.51 Hz, 1 H) 8.03 (s, 1 H) 8.15 (dd, *J*=8.83, 1.58 Hz, 1 H) 9.01 (d, *J*=1.58 Hz, 1 H) 12.69 (s, 1 H)

¹³C-NMR (150 MHz, DMSO-*d*₆) δ (ppm): 110.04 (1 CH), 123.1 (1 C), 123.51 (1 CH), 124.02 (1 C), 128.79 (1 CH), 129.29 (1 CH), 136.03 (1 C), 143.85 (1 C), 168 (1 C).

Elemental analysis: Calculated (C₃₄H₂₀N₂O₈ · 1.76·H₂O): C: 66.27%; H: 3.85%; N: 4.55%; found: C: 66.22%; H: 3.85%; N: 4.61%.

DRIFT, KBr, 298 K (cm⁻¹): 3070 (w), 2647 (w), 1694 (w), 1627 (s), 1602 (m), 1518 (s), 1475 (m), 1416 (m), 1339 (w), 1292 (s), 1266 (s), 1179 (m), 1137 (w), 1027 (s), 950 (w), 904 (m), 818 (m), 805 (w), 768 (s), 722 (w), 703 (w), 666 (w).

2.4.3 Tetrabutyl 9,9'-(naphthalene-2,6-diyl)bis(9H-carbazole-3,6-dicarboxylate)



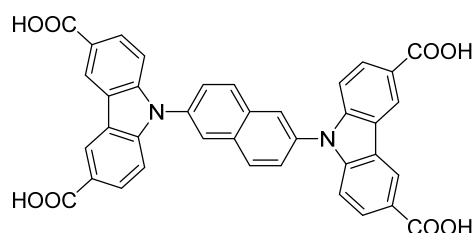
Synthesis conditions: 3.76 g (10.2 mmol) *n*-butylester **8**, 0.98 g (3.41 mmol) 2,6-dibromonaphthalene, 1.88 g (13.6 mmol) potassium carbonate, 428 mg (2.12 mmol) copper(I) iodide, 0.1 ml (0.91 mmol) *N,N'*-dimethylethylenediamine, 30 ml anhydr. 1,4 dioxane, 110 °C for 3 d; Flash column chromatography chloroform : *iso*-hexane : ethyl acetate = 1 : 0.03 : 0.06 (R_f 0.53); Yield: 2.81 g (96%) white powder.

¹H NMR (500 MHz, CHLOROFORM-*d*) δ (ppm): 1.05 (t, J =7.41 Hz, 6 H) 1.52 - 1.65 (m, 4 H) 1.83 - 1.92 (m, 4 H) 4.44 (t, J =6.78 Hz, 4 H) 7.51 (d, J =8.51 Hz, 2 H) 7.81 (dd, J =8.67, 1.73 Hz, 1 H) 8.21 (d, J =1.89 Hz, 1 H) 8.22 - 8.25 (m, 3 H) 8.99 (s, 2 H).

¹³C NMR (126 MHz, CHLOROFORM-*d*) δ (ppm): 14.10 (s, 1 CH₃) 19.63 (s, 1 CH₂) 31.18 (s, 1 CH₂) 65.17 (s, 1 CH₂) 109.92 (s, 1 CH) 123.37 (s, 1 C) 123.58 (s, 1 CH) 123.73 (s, 1 C) 126.03 (s, 1 CH) 126.42 (s, 1 C) 128.61 (s, 1 CH) 130.66 (s, 1 CH) 133.54 (s, 1 C) 135.32 (s, 1 C) 144.44 (s, 1 C) 167.28 (s, 1 C) 171.41 (s, 1 C).

Elemental analysis: Calculated: C: 75.5%; H: 6.34%; N: 3.26%; found: C: 75.93%; H: 6.342%; N: 2.91%.

2.4.4 9,9'-(naphthalene-2,6-diyl)bis(9H-carbazole-3,6-dicarboxylic acid)



Synthesis conditions: 1.7 g (1.98 mmol) ester **10**, 1 g (17.6 mmol) potassium hydroxide, 33 ml THF, 5 ml methanol, 16 ml H₂O, 75 °C for 3 d.; Yield: 1.18 g (94%) white powder.

¹H NMR (500 MHz, DMSO-*d*₆) δ (ppm): 7.59 (d, J =8.51 Hz, 2 H) 7.91 - 7.99 (m, 1 H) 8.14 (dd, J =8.83, 1.26 Hz, 2 H) 8.44 (d, J =8.83 Hz, 1 H) 8.53 (s, 1 H) 9.03 (s, 2 H) 12.84 (br. s., 2 H).

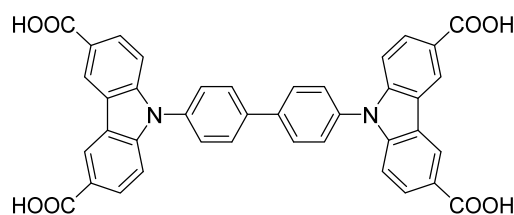
¹³C NMR (126 MHz, DMSO-*d*₆) δ (ppm): 110.09 (s, 1 CH) 122.66 (s, 1 C) 123.13 (s, 1 CH) 123.61 (s, 1 C) 125.78 (s, 1 CH) 125.95 (s, 1 C) 128.43 (s, 1 CH) 130.69 (s, 1 CH) 133.04 (s, 1 C) 134.26 (s, 1 C) 143.63 (s, 1 C) 167.63 (s, 1 C).

MALDI-TOF-MS (m/z): Calculated for C₃₈H₂₂N₂O₈: 634; found 634 [M]⁺.

Elemental analysis: Calculated (C₃₈H₂₂N₂O₈ 1.15·H₂O): C: 70.29%; H: 3.84%; N: 4.41%; found: C: 70.29%; H: 3.84%; N: 3.56%.

DRIFT, KBr, 298 K (cm⁻¹): 3065(w), 2642 (w), 1694 (s), 1629 (m), 1601 (s), 1508 (w), 1477 (s), 1393 (s), 1342 (m), 1236 (s), 1159 (m), 1137 (m), 1027 (w), 923 (w), 904 (m), 828 (m), 768 (s), 737 (w), 724 (w), 687 (w).

2.4.5 Tetrabutyl 9,9'-([1,1'-biphenyl]-4,4'-diyl)bis(9H-carbazole-3,6-dicarboxylate)



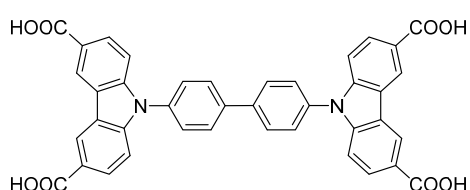
Synthesis conditions: 815 mg (2.22 mmol) *n*-butylester **8**, 300 mg (0.74 mmol) 4,4'-diiodobiphenyl, 224 mg (1.62 mmol) potassium carbonate, 90 mg (0.66 mmol) copper(I) iodide, 104 mg (0.9 mmol) *L*-proline, 15 ml anhydr. DMF, 120 °C for 48 h; Flash column chromatography DCM : chloroform : ethyl acetate – 0.1:1:0.010 (R_f 0.6); Yield: 280 mg (43%) white powder.

^1H NMR (300 MHz, CHLOROFORM-*d*) δ (ppm): 1.05 (t, $J=7.37$ Hz, 4 H) 1.57 (dq, $J=14.94, 7.36$ Hz, 3 H) 1.76 - 1.93 (m, 3 H) 4.43 (t, $J=6.61$ Hz, 3 H) 7.50 (d, $J=8.69$ Hz, 2 H) 7.73 (d, $J=8.50$ Hz, 2 H) 7.98 (d, $J=8.50$ Hz, 2 H) 8.21 (dd, $J=8.69, 1.70$ Hz, 2 H) 8.96 (d, $J=1.32$ Hz, 2 H).

^{13}C NMR (126 MHz, CHLOROFORM-*d*) δ (ppm): 13.81 (s, 1 CH₃) 19.34 (s, 1 CH₂) 30.88 (s, 1 C H₂) 64.85 (s, 1 C H₂) 109.72 (s, 1 CH) 122.98 (s, 1 CH) 123.19 (s, 1 C) 123.25 (s, 1 C) 127.52 (s, 1 CH) 128.20 (s, 1 CH) 128.85 (s, 1 CH) 136.14 (s, 1 C) 140.01 (s, 1 C) 144.02 (s, 1 C) 167.00 (s, 1 C).

Elemental analysis: Calculated: C: 76%; H: 6.38%; N: 3.17%; found: C: 75.69%; H: 6.172%; N: 2.98%.

2.4.6 9,9'-([1,1'-biphenyl]-4,4'-diyl)bis(9H-carbazole-3,6-dicarboxylic acid)



Synthesis conditions: 150 mg (0.17 mmol) ester **12**, 700 mg (12.3 mmol) potassium hydroxide, 18 ml THF, 1 ml methanol, 0.5 ml H₂O + 3 ml H₂O after 1 d, 85 °C for 72 h; Yield: 60 mg (54%) white powder.

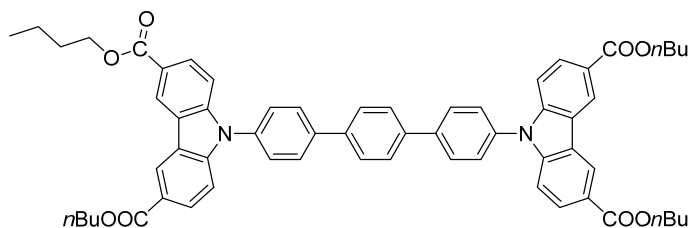
^1H NMR (300 MHz, DMSO-*d*₆) δ (ppm): 7.55 (d, $J=8.69$ Hz, 1 H) 7.86 (d, $J=8.50$ Hz, 1 H) 8.09 - 8.20 (m, 2 H) 9.01 (d, $J=1.51$ Hz, 1 H) 12.85 (br. s., 1 H).

^{13}C NMR (75 MHz, DMSO-*d*₆) δ (ppm): 110.02 (s, 1 CH) 122.61 (s, 1 C) 123.06 (s, 1 CH) 123.51 (s, 1 C) 127.56 (s, 1 CH) 128.34 (s, 1 CH) 128.80 (s, 1 CH) 135.50 (s, 1 C) 139.17 (s, 1 C) 143.42 (s, 1 C) 167.61 (s, 1 C).

Elemental analysis: Calculated (C₄₀H₂₄N₂O₈ · 3·H₂O): C: 67.22%; H: 4.23%; N: 3.92%; found: C: 66.78%; H: 3.73%; N: 3.96%.

DRIFT, KBr, 298 K (cm⁻¹): 3037 (w), 2619 (w), 1894 (m), 1657 (s), 1631 (s), 1602 (s), 1503 (s), 1403 (m), 1347 (m), 1298 (m), 1258 (s), 1186 (m), 1169 (m), 1135 (s), 1105 (w), 1062 (s), 1027 (m), 1007 (w), 915 (m), 899 (w), 855 (w), 813 (w), 757 (m), 715 (w), 669 (w).

2.4.7 Tetrabutyl 9,9'-([1,1':4,1''-terphenyl]-4,4''-diyl)bis(9H-carbazole-3,6-dicarboxylate)



Synthesis conditions: 5.71 g (15.5 mmol) *n*-butylester **8**, 2 g (5.18 mmol) 4,4''-dibromo-*p*-terphenyl, 2.86 g (20.7 mmol) potassium carbonate, 326 mg (1.71 mmol) copper(I) iodide, 0.1 ml (0.91 mmol) *N,N'*-

dimethylethylenediamine, 80 ml anhydr. 1,4 dioxane, 110 °C for 8 d; Flash column chromatography chloroform : *iso*-hexane : ethyl acetate – 1 : 0.5 : 0.02 (R_f 0.55); Yield: 3.65 g (95%) white powder.

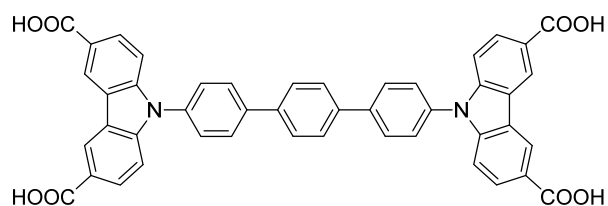
^1H NMR (500 MHz, CHLOROFORM-*d*) δ (ppm): 1.05 (t, $J=7.41$ Hz, 3 H) 1.57 (s, 2 H) 1.72 - 1.90 (m, 2 H) 4.43 (t, $J=6.62$ Hz, 2 H) 7.50 (d, $J=8.83$ Hz, 1 H) 7.69 (d, $J=8.51$ Hz, 1 H) 7.88 (s, 1 H) 7.96 (d, $J=8.20$ Hz, 1 H) 8.21 (dd, $J=8.51, 1.58$ Hz, 1 H) 8.96 (d, $J=1.58$ Hz, 1 H).

^{13}C NMR (126 MHz, CHLOROFORM-*d*) δ (ppm): 13.84 (s, 1 CH₃) 19.38 (s, 1 CH₂) 30.93 (s, 1 CH₂) 64.88 (s, 1 CH₂) 109.80 (s, 1 CH) 123.03 (s, 1 C) 123.20 (s, 1 C) 123.24 (s, 1 CH) 127.46 (s, 1 CH) 127.80 (s, 1 CH) 128.22 (s, 1 CH) 128.73 (s, 1 CH) 135.82 (s, 1 C) 139.43 (s, 1 C) 140.65 (s, 1 C) 144.16 (s, 1 C) 167.14 (s, 1 C).

MALDI-TOF-MS (m/z): Calculated for C₆₂H₆₀N₂O₈: 887; found: 887 [M-C₄H₉OH]⁺.

Elemental analysis: Calculated: C: 77.48%; H: 6.29%; N: 2.91%; found: C: 77.57%; H: 5.46%; N: 2.93%.

2.4.8 9,9'-([1,1':4',1''-Terphenyl]-4,4''-diyl)bis(9H-carbazole-3,6-dicarboxylic acid)



Synthesis conditions: 3.6 g (3.75 mmol) ester **14**, 8 g (144 mmol) potassium hydroxide, 350 ml THF, 30 ml methanol, 2 ml H₂O, 90 °C for 24 h; Yield: 2.65 g (96%) white powder.

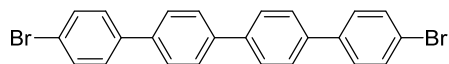
¹H NMR (500 MHz, DMSO-*d*₆) δ (ppm): 7.53 (d, *J*=8.51 Hz, 1 H) 7.79 (d, *J*=7.88 Hz, 1 H) 7.96 (s, 1 H) 8.08 (d, *J*=8.20 Hz, 1 H) 8.12 (d, *J*=8.51 Hz, 1 H) 8.99 (s, 1 H) 12.79 (br. s., 1 H).

¹³C NMR (126 MHz, DMSO-*d*₆) δ (ppm): 109.89 (s, 1 CH) 122.47 (s, 1 C) 122.93 (s, 1 C) 123.36 (s, 1 CH) 127.32 (s, 1 CH) 127.43 (s, 1 CH) 128.23 (s, 1 C) 128.35 (s, 1 CH) 135.09 (s, 1 C) 138.38 (s, 1 C) 139.40 (s, 1 C) 143.32 (s, 1 C) 167.53 (s, 1 C).

Elemental analysis: Calculated (C₄₆H₂₈N₂O₈·3.85H₂O): C: 68.54%; H: 4.46%; N: 3.48%; found: C: 68.15%; H: 4.027%; N: 3.40%.

DRIFT, KBr, 298 K (cm⁻¹): 3069 (w), 2628 (w), 1907 (w), 1695 (s), 1630 (m), 1600 (s), 1533 (w), 1494 (s), 1365 (m), 1291 (s), 1235 (s), 1173 (m), 1137 (m), 1027 (w), 1005 (m), 949 (w), 905 (w), 815 (s), 770 (s), 726 (m), 680 (w).

2.4.9 4,4'''-Dibromo-1,1':4',1''':4'',1''''-quaterphenyl



A flame-dried 500 ml Schlenk flask was charged with 1.7 g (3.36 mmol) iodide **11**, 1.45 g (7.22 mmol) 4-bromophenylboronic acid **15**, 2.7 g (19.5 mmol) potassium carbonate, 43 mg (0.037 mmol) tetrakis(triphenylphosphine)palladium(0), and a degassed mixture of 105 ml toluene, 15 ml water and 60 ml methanol. The brown suspension was refluxed under inert atmosphere at 110 °C for 3 d. The solvents were removed in vacuum and the remaining solid dissolved in chloroform, extracted with water, and the combined organic phases dried over MgSO₄. The obtained yellow solid was purified by flash column chromatography using an iso-hexane : chloroform (2 : 1) mixture (*R*_f 0.54) to obtain 850 mg (45 %) of white powder.

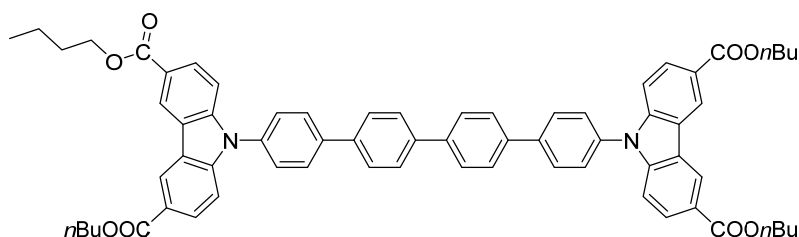
No NMR spectra could be collected due to low solubility in common organic solvents.

MALDI-TOF-MS (m/z): Calculated for C₂₄H₁₆Br₂: 463; found: 463 [M]⁺.

Elemental analysis: Calculated: C: 62.1%; H: 3.47%; found: C: 62.22%; H: 3.54%.

DRIFT, KBr, 298 K (cm⁻¹): 2585 (w), 2297 (w), 1912 (m), 1898 (m), 1778 (w), 1681 (w), 1646 (w), 1596 (m), 1476 (s), 1436 (m), 1388 (s), 1347 (m), 1281 (m), 1181 (w), 1141 (m), 1121 (m), 1103 (m), 1075 (s), 1043 (w), 1009 (m), 1000 (s), 964 (w), 860 (m), 843 (m), 822 (s), 807 (s), 764 (m), 750 (m), 742 (m), 695 (m), 660 (w), 642 (m), 624 (w).

2.4.10 Tetrabutyl 9,9'-([1,1':4',1''':4'',1''''-quaterphenyl]-4,4'''-diyl)bis(9H-carbazole-3,6-dicarboxylate)



Synthesis conditions: 7.12 g (19.4 mmol) *n*-butylester **8**, 3 g (6.46 mmol) 4,4'''-dibromo-1,1':4',1''':4'',1''''-quaterphenyl **16**, 3.57 g (25.8 mmol) potassium carbonate, 613 mg (3.23 mmol) copper(I) iodide,

0.1 ml (0.91 mmol) *N,N'*-dimethylethylenediamine, 80 ml anhydr. 1,4 dioxane, 110 °C for 8 d; Flash column chromatography chloroform : *iso*-hexane : ethyl acetate – 1 : 0.3 : 0.01 (R_f 0.29); Yield: 1.96 g (29%) white powder.

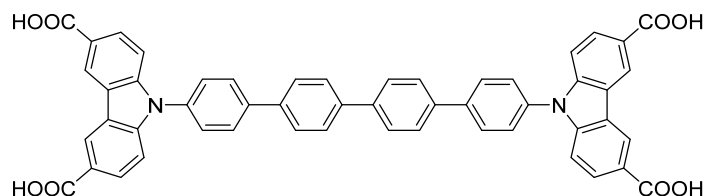
^1H NMR (500 MHz, CHLOROFORM-*d*) δ (ppm): 1.05 (t, $J=7.41$ Hz, 3 H) 1.51 - 1.70 (m, 1 H) 1.74 - 1.91 (m, 1 H) 4.43 (t, $J=6.62$ Hz, 1 H) 7.49 (d, $J=8.83$ Hz, 1 H) 7.67 (d, $J=8.51$ Hz, 1 H) 7.84 (d, $J=2.21$ Hz, 2 H) 7.94 (d, $J=8.51$ Hz, 1 H) 8.20 (dd, $J=8.51, 1.58$ Hz, 1 H) 8.96 (d, $J=1.58$ Hz, 1 H).

^{13}C NMR (126 MHz, CHLOROFORM-*d*) δ (ppm): 14.10 (s, 1 CH₃) 19.63 (s, 1 CH₂) 31.17 (s, 1 C) CH₂) 65.12 (s, 1 C CH₂) 110.06 (s, 1 CH) 123.26 (s, 1 CH) 123.43 (s, 1 C) 127.65 (s, 1 CH) 127.88 (s, 1 CH) 128.45 (s, 1 CH) 128.92 (s, 1 CH) 135.91 (s, 1 C) 139.28 (s, 1 C) 140.19 (s, 1 C) 141.03 (s, 1 C) 144.39 (s, 1 C) 167.33 (s, 1 C).

MALDI-TOF-MS (m/z): Calculated for C₆₈H₆₄N₂O₈: 963; found: 963 [M-C₄H₉OH]⁺.

Elemental analysis: Calculated: C: 78.47%; H: 6.22%; N: 2.7%; found: C: 77.88%; H: 6.117%; N: 2.79%.

2.4.11 9,9'-([1,1':4',1'':4'',1'''-Quaterphenyl]-4,4''-diyl)bis(9H-carbazole-3,6-dicarboxylic acid)



Synthesis conditions: 1.95 g (1.88 mmol) ester **17**, 1.4 g (24.6 mmol) potassium hydroxide, 120 ml THF, 2 ml methanol, 5 ml H₂O, 85 °C for 3 d; Yield: 1.5 g (98%) white powder.

^1H NMR (500 MHz, DMSO-*d*₆) δ (ppm): 7.53 (d, $J=8.83$ Hz, 1 H) 7.78 (d, $J=8.20$ Hz, 1 H) 7.93 (s, 2 H) 8.07 (d, $J=8.51$ Hz, 1 H) 8.12 (dd, $J=8.51, 1.58$ Hz, 1 H) 8.99 (s, 1 H) 12.73 (s, 1 H).

^{13}C NMR (126 MHz, DMSO-*d*₆) δ (ppm): 110.12 (s, 1 CH) 122.66 (s, 1 C) 123.14 (s, 1 CH) 123.54 (s, 1 C) 127.38 (s, 1 CH) 127.53 (s, 1 CH) 127.56 (s, 1 C) 128.44 (s, 1 CH) 128.53 (s, 1 CH) 135.22 (s, 1 C) 138.31 (s, 1 C) 138.94 (s, 1 C) 139.69 (s, 1 C) 143.53 (s, 1 C) 167.75 (s, 1 C).

Elemental analysis: Calculated (C₅₂H₃₂N₂O₈ · 2.85·H₂O): C: 72.27%; H: 4.4%; N: 3.24%; found: C: 72.10%; H: 4.197%; N: 3.25%.

DRIFT, KBr, 298 K (cm⁻¹): 3627 (w, br), 2629 (w), 1907 (w), 1694 (s), 1630 (m), 1601 (m), 1523 (m), 1489 (s), 1401 (m), 1364 (m) 1290 (s), 1250 (s), 1173 (m), 1137 (w), 1027 (w), 1003 (w), 949 (w), 907 (m), 813 (s), 770 (m), 735 (w), 725 (w), 692 (w).

3 Synthesis, Desolvation, and Characterisation of Metal-Organic Frameworks

3.1 Synthesis of microcrystalline MOF powders

In a previous study we have demonstrated that large crystals of DUT-49 show enhanced adsorption capacity and pronounced NGA⁷. Thus, the reaction conditions for the synthesis of DUT-48, -46, -50, -151 were chosen to produce crystals of average size above 2 μm , based on the reaction of DUT-49 by using acetic acid as modulator in a solvothermal reaction of ligands L₁ - L₅ at 80 °C. Because NMP was found to partially reduce Cu²⁺ if the reactions were carried out over 72 h or longer, we chose to use DMF

instead. Due to the lower solubility especially of ligand L₁ and L₂ in DMF, larger amounts of DMF in comparison to NMP were used. The reaction conditions including the corresponding mean crystal size of the activated MOF powders are summarized in Supplementary Table 2.

Supplementary Table 2. Reaction conditions and corresponding mean crystal size.

Material ID	m_{ligand} (mg)	n_{ligand} (mmol)	$m_{\text{Cu(NO}_3)_2 \cdot 3\text{H}_2\text{O}}$ (mg)	$n_{\text{Cu(NO}_3)_2 \cdot 3\text{H}_2\text{O}}$ (mmol)	$V_{\text{Acetic acid}}$ (ml)	$n_{\text{Acetic acid}}$ (mmol)	<i>Eq. per ligand</i>	V_{solvent} (ml)	t_{Reaction} (h)	Yield (%) ^[a]	Mean crystal size/ RSD (nm)
DUT-46	800	1.26	760	3.15	16	279.7	222	400	48	83.8	2488±1709
DUT-48	1000	1.71	1030	4.26	12	209.8	123	800	72	82.7	4065±2194
DUT-49	1000	1.53	935	3.86	7.5	240	150	172	44	39.3	3488±1574
DUT-50	500	0.68	410	1.70	7.75	135.5	199	150	48	63.4	8016±6048
DUT-151	400	0.49	480	1.99	4	69.9	142	95	48	73.8	9380±3858

^[a] yield based on L₃ after supercritical activation. Actual yields of reaction may be higher, ^[b] NMP used instead of DMF due to solubility limitations.

3.2 Synthesis of MOF single crystals

To obtain crystals with sizes large enough for single crystal X-ray diffraction (> 90 μm) we adapted the reaction conditions by diluting the reaction mixture with DMF and increasing the amount of acetic acid acting as modulator. The reaction conditions are summarized in Supplementary Table 3.

Supplementary Table 3. Synthesis conditions.

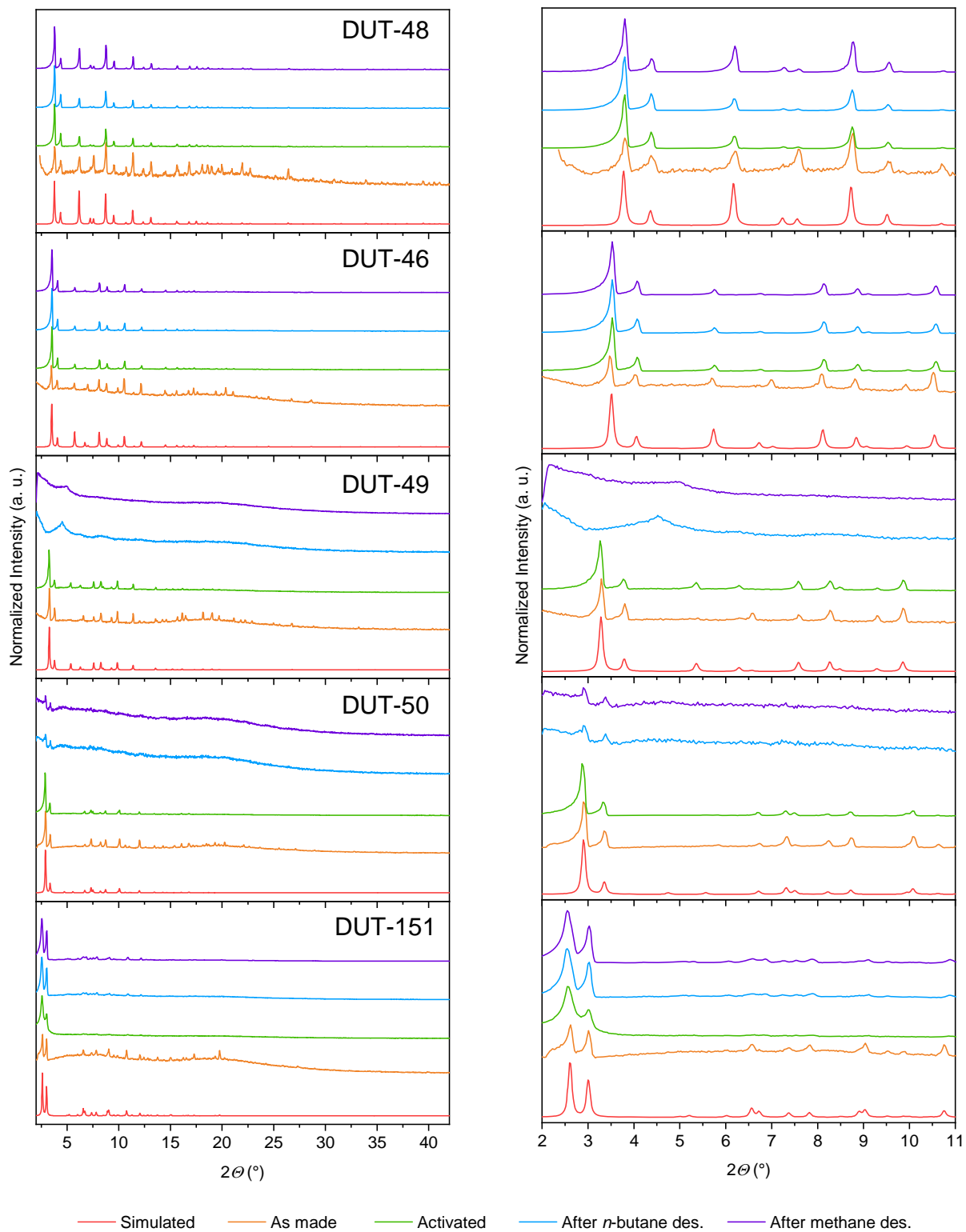
Material ID	m_{Ligand} (mg)	n_{Ligand} (μmol)	$m_{\text{Cu(NO}_3)_2 \cdot 3\text{H}_2\text{O}}$ (mg)	$n_{\text{Cu(NO}_3)_2 \cdot 3\text{H}_2\text{O}}$ (μmol)	$V_{\text{Acetic acid}}$ (μl)	$n_{\text{Acetic acid}}$ (mmol)	<i>Eq. per ligand</i>	V_{DMF} (ml)	t_{Reaction} (d)	Crystal shape and size
DUT-46	10	15.8	9.5	39.3	0.27	4.7	299	4	2	Cubes, 90 μm
DUT-48	10	17.1	9.8	40.6	0.11	1.9	112	5	3	Cubes, 90 μm
DUT-49	10	15.1	9.5	39.3	0.5	8.7	577	4	5	Cubes, 130 μm
DUT-50	10	13.6	8.2	33.9	0.16	2.8	206	4	3	Cuboctahedra, 110 μm
DUT-151int	10	12.3	7.4	30.6	0.14	2.4	199	4	1	Cubes, 100 μm

3.3 Desolvation of microcrystalline MOF powder

After the solvothermal reaction the blue precipitates were separated from the reaction solution by centrifugation and washed 6 times with fresh DMF over a period of two days at room temperature. DMF was exchanged with anhydr. acetone by washing 10 times over a period of at least four days. All samples were subjected to an activation procedure involving supercritical CO₂, as previously described for DUT-49⁸: In acetone suspended samples were placed on filter frits in a Jumbo Critical Point Dryer 13200J AB (SPI Supplies) which was subsequently filled with liquid CO₂ (99.995% purity) at 15 °C and 50 bar. To ensure a complete substitution of acetone by CO₂, the liquid in the autoclave was exchanged with fresh CO₂ 18 times over a period of 5 days. Temperature and pressure were then raised beyond the supercritical point of CO₂ (35 °C and 100 bar) and kept until the temperature and pressure were constant at least for 1 h. Supercritical CO₂ was slowly released over 3 h and the dry powder was transferred and stored in an argon filled glove box. To ensure complete removal of the solvent from the pores (especially from the open metal sites of the Cu-paddle-wheels) additional thermal activation at 120 °C in a Schlenk-tube under dynamic vacuum of 10⁻⁴ kPa for at least 24 h was performed.

3.4 Characterisation of Metal-Organic Frameworks

3.4.1 Powder X-Ray Diffraction



Supplementary Figure 5. PXRD patterns from top to bottom for DUT-48, -46, -49, -50, -151_{int}. Left column: wide angle and on the right corresponding magnified regions.

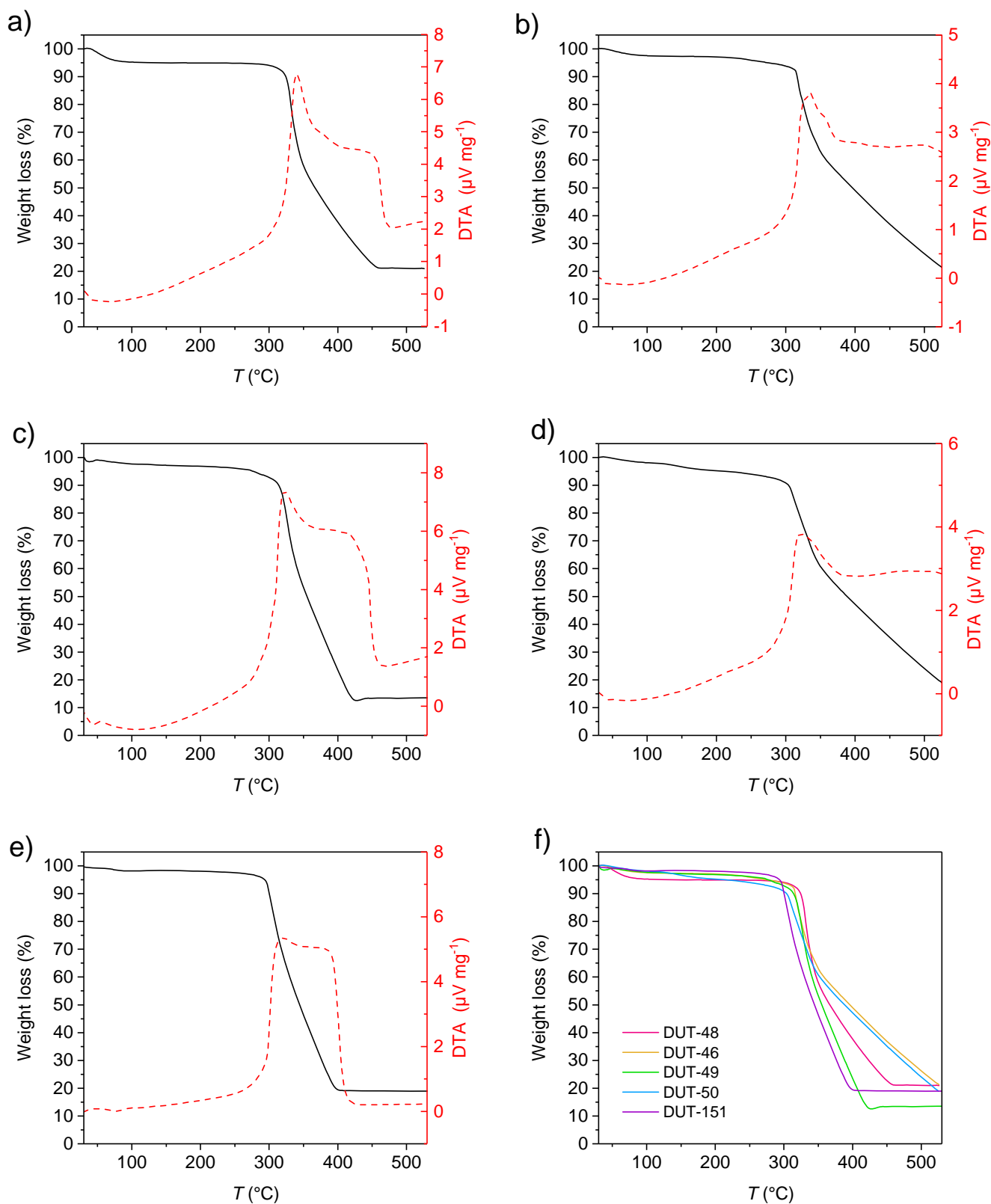
3.4.2 Single Crystal X-Ray Diffraction Analysis of DUT-46, DUT-50, DUT-151int

Blue cubic single crystals of DUT-46, DUT-50 and DUT-151 with dimensions ranging from 30 μm to 80 μm were prepared in a borosilicate glass capillary ($d = 0.3 \text{ mm}$) with small amount of the mother liquor. The capillaries were sealed with wax from both sides in order to avoid the contact with ambient atmosphere. The datasets were collected at BESSY MX BL14.3 beamline of Helmholtz-Zentrum Berlin für Materialien und Energie⁹. Monochromatic X-ray radiation with a wavelength of $\lambda = 0.08945 \text{ nm}$ ($E = 13.5 \text{ keV}$) was used in experiments. All datasets were collected at room temperature. After short test scans, the crystal symmetry and scan range were determined in each particular case using iMosflm program.^{10,11} The φ -scans with oscillation range of 0.5° were used for data collection. In the case of cubic structures of DUT-46 and DUT-50, 100 images were collected to reach the maximal completeness. For DUT-151, crystallizing in *C*-centered monoclinic lattice, 240 images were required. Further the datasets were processed automatically using XDSAPP 2.0 software.¹² Crystal structures were solved by direct methods and refined by full matrix least-squares on F^2 using SHELX-2016/4 program package.^{13,14} All non-hydrogen atoms were refined in anisotropic approximation. Hydrogen atoms were refined in geometrically calculated positions using “riding model” with $U_{iso}(H)=1.2U_{iso}(C)$. Since the symmetry of the naphthalene core in DUT-46 is incompatible with the symmetry of its position in the unit cell, the molecular fragment was refined disordered over four symmetrically dependent positions. In the case of DUT-50, the disorder of both symmetrically independent phenyl rings was treated by splitting over two equally occupied positions. The lower symmetry of DUT-151int, with four symmetrically independent paddle wheels in the asymmetric unit prompted us to use the AFIX 66, SIMU and DELU instructions in order to constrain the geometry and anisotropic displacement parameters of all phenyl rings in the structure. The large pores, high crystal symmetry and high measurement temperature did not allow refining the disordered solvent molecules within the pores of the frameworks, therefore, SQUEEZE routine in PLATON was used to generate the reflection intensities with subtracted solvent contribution.¹⁵ CCDC-1889257, 1889255 and 1889256 contain the supplementary crystallographic data for DUT-46, DUT-50 and DUT-151int, correspondingly. These data can be obtained free of charge from the Cambridge Crystallographic Data Centre via www.ccdc.cam.ac.uk/data_request/cif.

Supplementary Table 4. Single crystal data of DUT-46, DUT-50 and DUT-151int

	DUT-46	DUT-50	DUT-151int
Empirical formula	C ₃₈ H ₁₈ O ₁₀ N ₂ Cu ₂	C ₄₆ H ₂₄ O ₁₀ N ₂ Cu ₂	C ₅₂ H ₂₈ O ₁₀ N ₂ Cu ₂
Formula weight	789.66	891.75	967.84
Crystal system, space group	cubic, <i>Fm</i> $\bar{3}$ <i>m</i>	cubic, <i>Fm</i> $\bar{3}$ <i>m</i>	monoclinic, <i>C2/m</i>
Unit cell dimensions, Å or deg	<i>a</i> = 43.550(5)	<i>a</i> = 52.630(6)	<i>a</i> = 71.700(14) <i>b</i> = 41.570(8) <i>c</i> = 41.450(8) β = 125.08(3)
Unit cell volume, Å ³	82597(28)	145781(51)	101103(46)
<i>Z</i>	24	24	24
Calculated density, g cm ⁻³	0.381	0.244	0.382
Absorption coefficient, 1/mm	0.604	0.345	0.500
<i>F</i> (000)	9536 (after SQUEEZE)	10848 (after SQUEEZE)	11808 (after SQUEEZE)
θ range, °	1.02 – 37.08	0.84 – 25.48	0.76 – 33.99
	-32 ≤ <i>h</i> ≤ 56	-47 ≤ <i>h</i> ≤ 49	-88 ≤ <i>h</i> ≤ 25
Limiting indices	-51 ≤ <i>k</i> ≤ 55	-50 ≤ <i>k</i> ≤ 45	-31 ≤ <i>k</i> ≤ 51
	-58 ≤ <i>l</i> ≤ 17	-48 ≤ <i>l</i> ≤ 19	-46 ≤ <i>l</i> ≤ 51
Reflections collected / unique	52664 / 4900	34672 / 3320	100606 / 71100
<i>R</i> (int)	0.0501	0.1122	0.0565
Data / parameters	4900 / 102	3320 / 110	71100 / 1574
Goof on <i>F</i> ²	1.621	1.111	1.034
Final <i>R</i> indices [<i>I</i> > 2σ(<i>I</i>)]	<i>R</i> ₁ = 0.0587 <i>wR</i> ₂ = 0.1948	<i>R</i> ₁ = 0.0597 <i>wR</i> ₂ = 0.1864	<i>R</i> ₁ = 0.0622 <i>wR</i> ₂ = 0.1693
<i>R</i> indices (all data)	<i>R</i> ₁ = 0.0804 <i>wR</i> ₂ = 0.2198	<i>R</i> ₁ = 0.0963 <i>wR</i> ₂ = 0.2267	<i>R</i> ₁ = 0.1018 <i>wR</i> ₂ = 0.1942
Largest diff. peak / hole, eÅ ⁻³	0.52 / -0.35	0.47 / -0.36	0.37 / -0.30

3.4.3 Thermogravimetric analysis



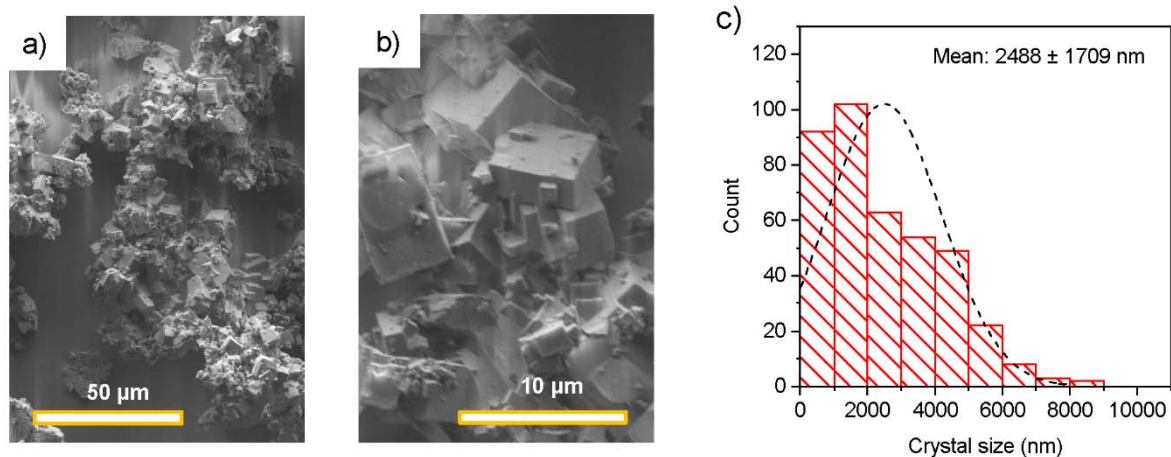
Supplementary Figure 6. Thermogravimetric analysis of a) DUT-48, b) DUT-46, c) DUT-49, d) DUT-50, e) DUT-151_{int} and f) comparison of all materials.

3.4.4 Elemental analysis

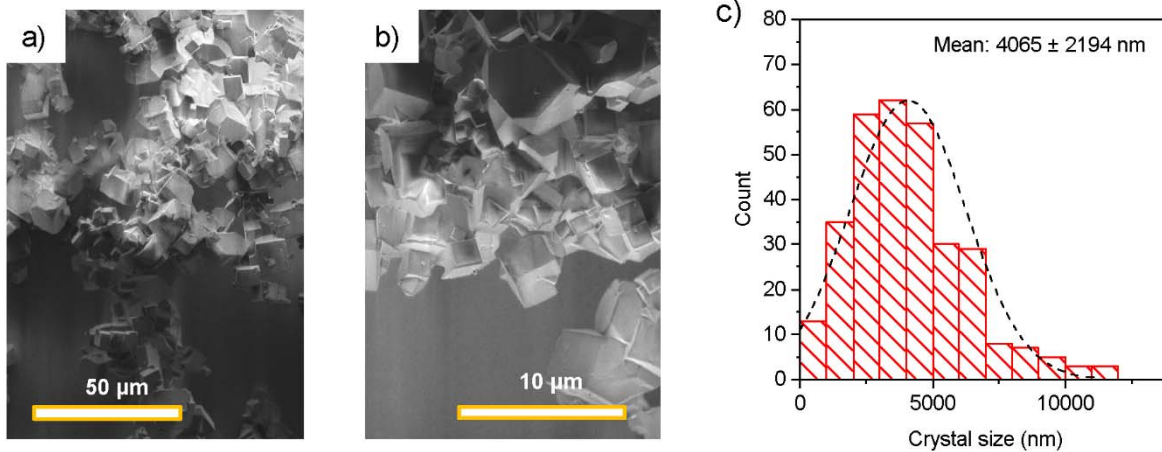
Supplementary Table 5. CHN elemental analysis for activated MOFs.

Material ID	Calculated (%)			Experimental (%)		
	C	H	N	C	H	N
DUT-46	60.24	2.39	3.7	59.06	2.33	3.81
DUT-48	57.71	2.28	3.96	56.99	2.403	3.98
DUT-49	61.3	2.57	3.57	59.85	2.542	3.64
DUT-50	64.26	2.81	3.26	62.82	3.549	3.45
DUT-151 <i>int</i>	66.73	3.02	2.99	66.58	3.077	3.37

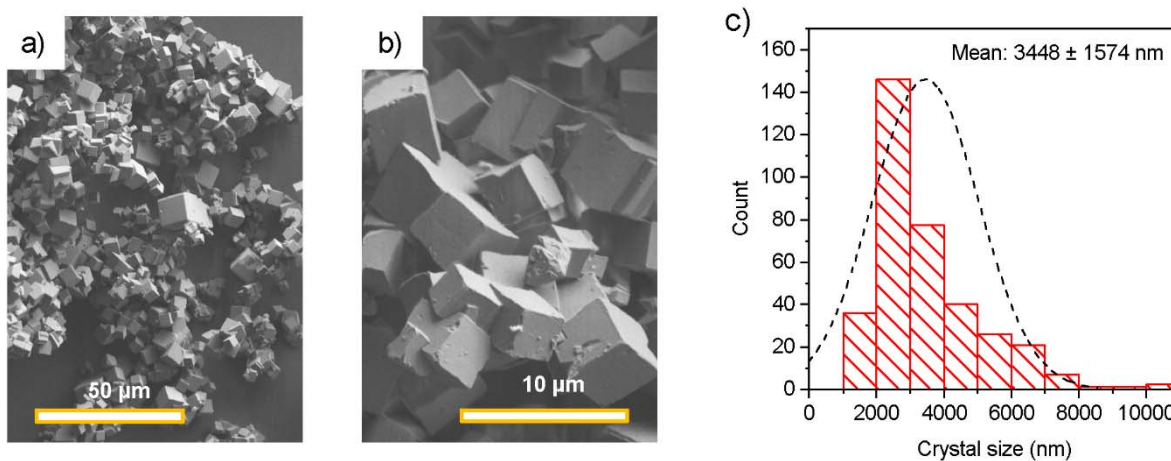
3.4.5 Scanning Electron microscopy and crystal size distribution



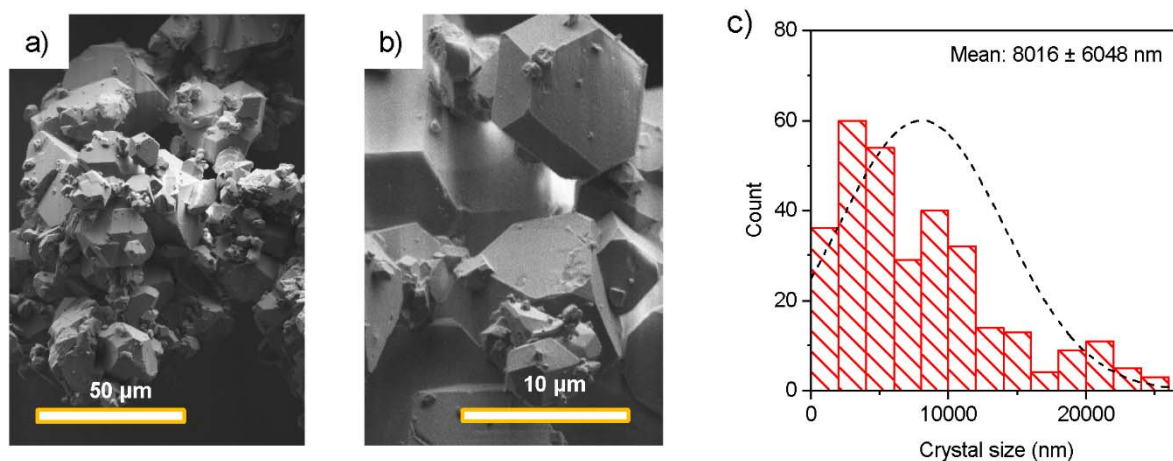
Supplementary Figure 7. a-b) Scanning electron microscopy images of DUT-48, scale bar a) 50 μm, b) 10 μm. c) Experimental crystal size distribution (red histogram) and distribution curve (black dashed line).



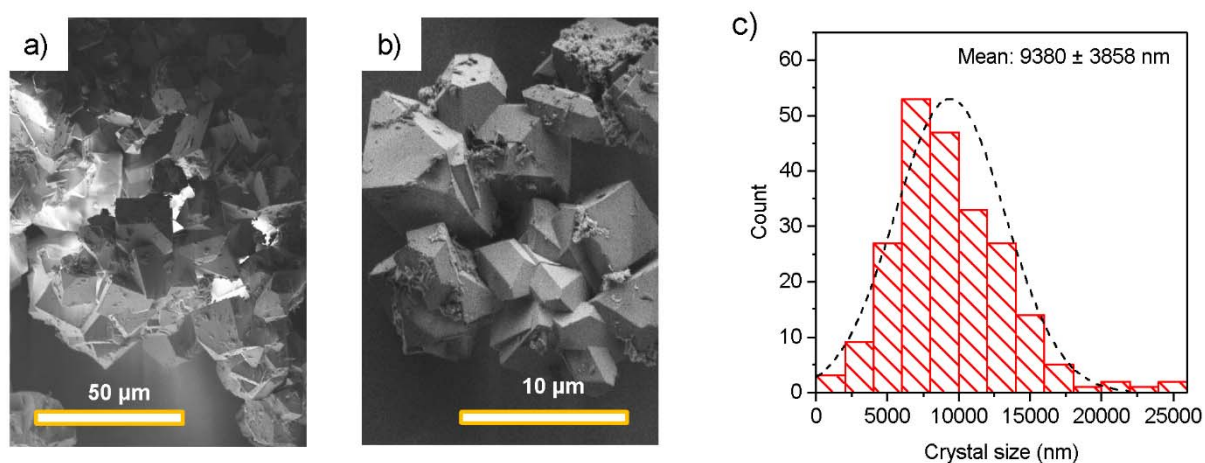
Supplementary Figure 8. a-b) Scanning electron microscopy images of DUT-46, scale bar a) 50 μm, b) 10 μm. c) Experimental crystal size distribution (red histogram) and distribution curve (black dashed line).



Supplementary Figure 9. a-b) Scanning electron microscopy images of DUT-49, scale bar a) 50 μm, b) 10 μm. c) Experimental crystal size distribution (red histogram) and distribution curve (black dashed line).



Supplementary Figure 10. a-b) Scanning electron microscopy images of DUT-50, scale bar a) 50 μm, b) 10 μm. c) Experimental crystal size distribution (red histogram) and distribution curve (black dashed line).

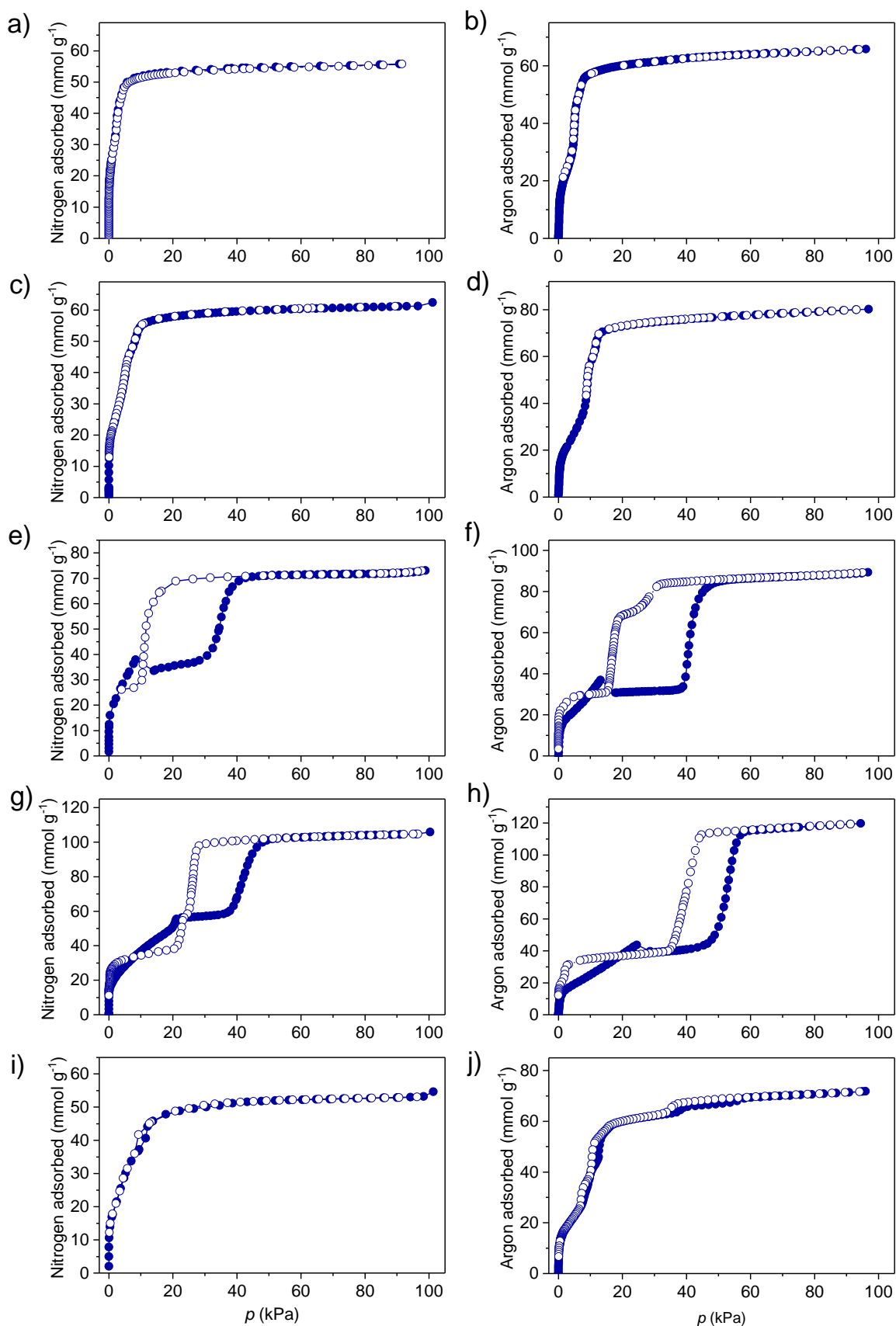


Supplementary Figure 11. a-b) Scanning electron microscopy images of DUT-151int, scale bar a) 50 μm, b) 10 μm. c) Experimental crystal size distribution (red histogram) and distribution curve (black dashed line).

Supplementary Table 6. Crystal size distribution extracted from SEM analysis.

Material ID	Mean crystal size (nm)	Standard deviation (nm)	Relative standard deviation (%)
DUT-48	2488	1709	68.7
DUT-46	4065	2194	53.9
DUT-49	3488	1574	45.1
DUT-50	8016	6048	75.4
DUT-151int	9380	3858	41.1

3.4.6 Argon, nitrogen, n-butane and methane adsorption isotherms



Supplementary Figure 12. Nitrogen at 77 K (left) and argon at 87 K (right) physisorption isotherms of DUT-48 (a,b), DUT-46 (c,d), DUT-49 (e,f), DUT-50 (g,h), DUT-151 (i,j). Filled symbols: adsorption, empty symbols: desorption.

Textural properties, such as geometric surface area, pore volume and pore size distributions (PSD), were calculated for these structures using the Zeo++ code¹⁶ on the basis of disorder-free simulated crystal structures for *op* phases and *in silico* determined crystal structures for the corresponding *cp* phases for DUT-48, -151, and experimental DUT-151*int* structure. The obtained results were compared to experimentally obtained values derived from nitrogen and argon adsorption isotherms at 77 K and 87 K, respectively.

Supplementary Table 7. Comparison of experimental and geometrical surface area and pore volumes.

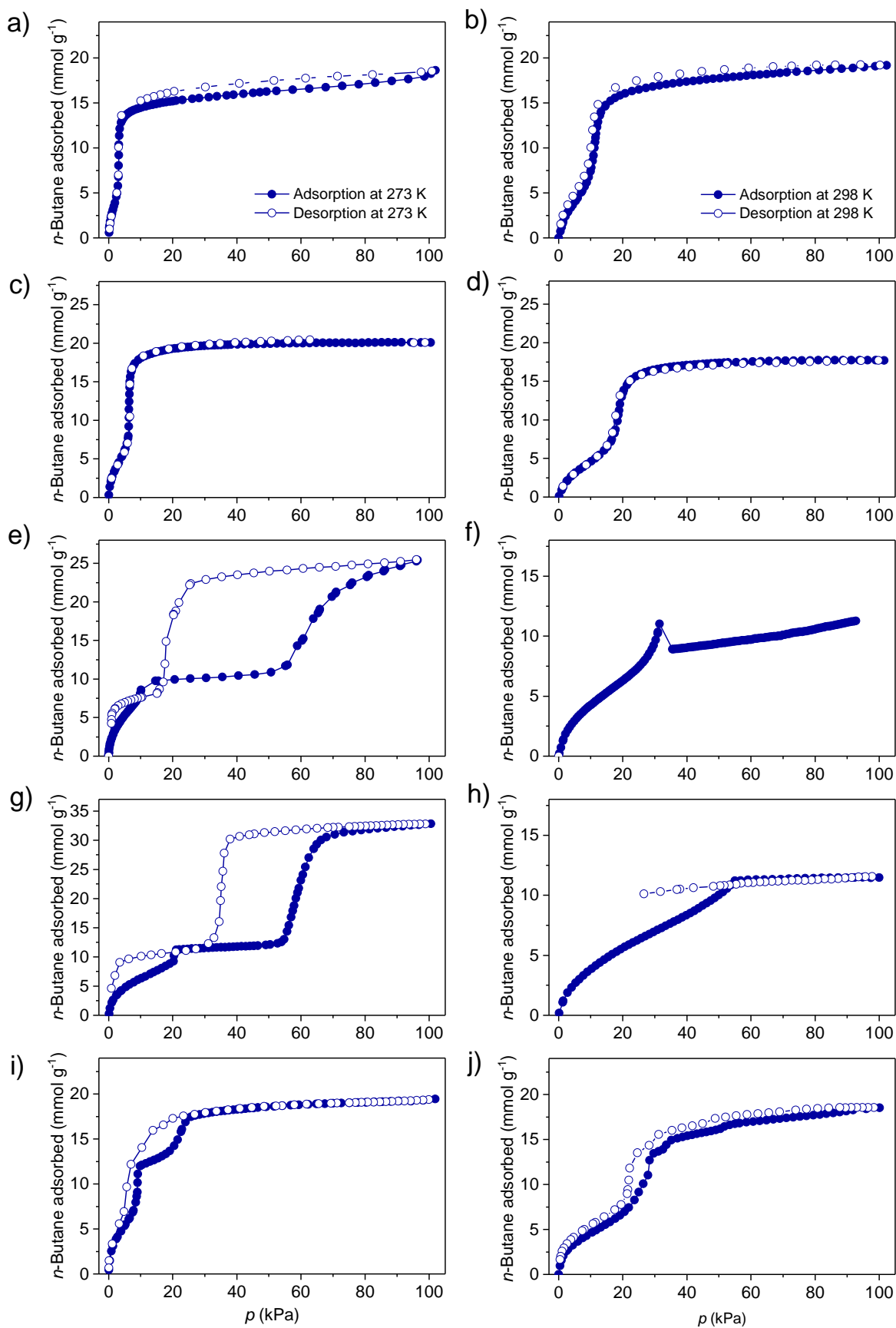
Material ID	Pore Volume (N ₂ ads.) (cm ³ g ⁻¹)	Pore Volume (Ar ads.) (cm ³ g ⁻¹)	Geometric surface area (m ² g ⁻¹)	Geometric pore volume (cm ³ g ⁻¹)	Framework density (g cm ⁻³)
DUT-48	1.98	1.88	4394	1.67	0.424
DUT-46	2.15	2.29	4736	1.89	0.365
DUT-49	2.73	2.81	5065	2.64	0.306
DUT-50	3.52	3.41	5386	3.45	0.235
DUT-151 <i>int</i>	1.95	2.05	4688	1.81	0.368
DUT-151	n. a.	n. a.	5672	4.43	0.183

In general, geometric values for pore volume and surface area are expected to be inferior to experimental values. From the experimental adsorption data, accurate determination of specific surface areas for the investigated materials was not possible by using the BET method fulfilling all consistency criteria recently defined for the analysis of mesoporous MOFs¹⁷. Several linear regions in the BET-plot were analysed and although all of them exhibit a good correlation coefficient only a few of them (marked red in Supplementary Table 7) were found to fulfil all consistency criteria recommended for determination of specific surface area by the BET method. Mostly, the third criterion is not fulfilled: the relative pressure value (p/p_0) corresponding to the monolayer capacity (n_m) should be located within the selected BET range.

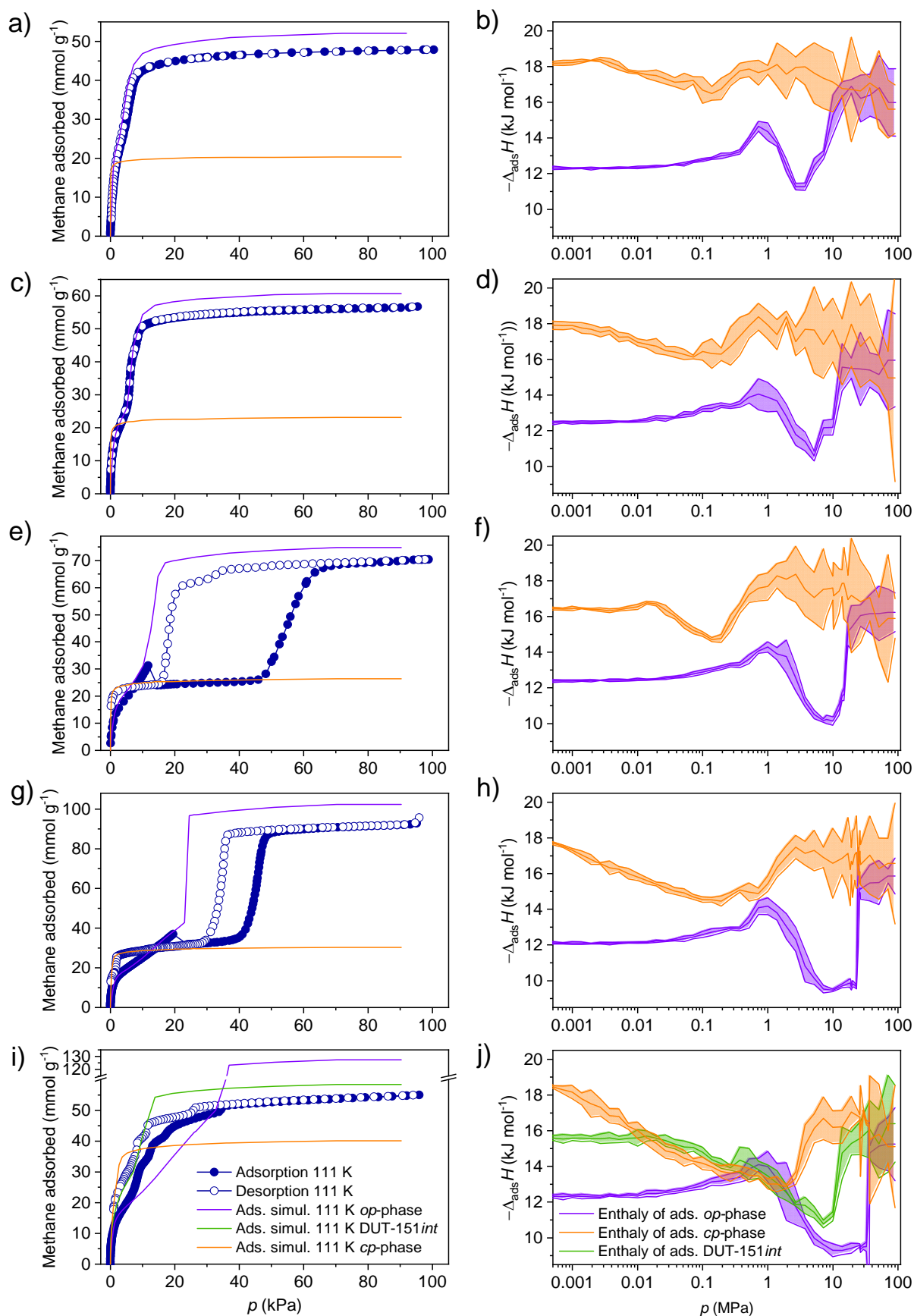
Only for DUT-151*int* a specific BET surface area in the range of the geometric surface area determined from the guest-free crystal structures was obtained. This might be due to the smaller pore size and microporous nature of DUT-151*int* in contrast to the mesoporous character of the other materials in this series. The only surface area observed to be within the selection criteria for DUT-50 is found to be drastically lower than the geometric surface area^{18,19}. Due to the observed disagreement of experimental and simulated surface area, only the geometric surface area is considered for the following discussions.

Supplementary Table 8. BET analysis of argon adsorption isotherms of DUT-46, -48, -50, and DUT-151. Red labeled values fulfill selection criteria for accurate experimental determination of specific surface area by the BET method.

Material ID	Relative pressure range	Slope	Intercept	Correlation coefficient R^2	BET constant, C	n_m (mol g ⁻¹)	p/p_0	n_m	BET surface area (m ² g ⁻¹)
DUT-48	0.007519 – 0.0112	1.05205	0.00425	0.9994	248	0.0236	0.059		2026
	0.01718 – 0.02553	0.83839	0.00715	0.9994	118	0.0296	0.084		2531
	0.02854 – 0.03448	0.61778	0.01301	0.9989	49	0.0397	0.126		3393
	0.03587 – 0.03981	0.4329	0.0195	0.9986	23	0.0553	0.172		4731
	0.05707 – 0.06591	0.3001	0.0152	0.9999	20	0.0799	0.180		6791
DUT-46	0.009669 – 0.0234	0.9980	0.005699	0.9998	176	0.0249	0.070		2133
	0.02528 – 0.04116	0.780784	0.010995	0.9992	72	0.0316	0.110		2704
	0.09791 – 0.10996	0.2319	0.0257	0.9999	10	0.0971	0.240		8310
DUT-151 _{int}	0.00019 – 0.00709	1.5573	0.0027	0.9999	578	0.016	0.040		1372
	0.00981 – 0.0244	1.1950	0.0060	0.9995	201	0.020	0.066		1782
	0.00272 – 0.0419	0.9522	0.0122	0.9991	79	0.0259	0.101		2219
	0.0448 – 0.0635	0.7228	0.0222	0.9983	34	0.0336	0.147		2873
	0.104 – 0.115	0.4004	0.02971	0.9998	15	0.058	0.208		4977
	0.14 – 0.164	0.4279	0.01423	0.9999	31	0.0566	0.152		4841
DUT-50	0.00432 – 0.00639	1.1761	0.00703	0.9991	168	0.0211	0.072		1809
	0.00695 – 0.0112	1.5407	0.0048	0.9994	321	0.0169	0.053		1385
	0.0655 – 0.108	0.776	0.0341	0.9976	23	0.0309	0.170		2642
	0.119 – 0.17	0.5368	0.06909	0.9986	9.8	0.0419	0.240		3581
	0.0182 – 0.245	0.4553	0.07436	0.9999	62	0.0541	0.113		4626



Supplementary Figure 13. *n*-Butane adsorption isotherms at 273 K (left) and 298 K (right) of DUT-48 (a,b), DUT-46 (c,d), DUT-49 (e,f), DUT-50 (g,h), DUT-151 (i,j). Filled symbols: adsorption, empty symbols: desorption.



Supplementary Figure 14. Methane isotherms at 111 K and corresponding simulated enthalpy profile of corresponding *op* and *cp* phases for DUT-48 (a,b), DUT-46 (c,d), DUT-49 (e,f), DUT-50 (g,h), and DUT-151 (i,j). Filled symbols: adsorption, empty symbols: desorption.

Supplementary Table 9. NGA parameters for DUT-49 and DUT-50.

Gas	T (K)	DUT-49		DUT-50	
		Δn_{NGA} (mmol g ⁻¹)	p_{Trans} (kPa)	Δn_{NGA} (mmol g ⁻¹)	p_{Trans} (kPa)
Nitrogen	77	4.41	8.32	0	21.14
Argon	87	6.13 (+0.02)	13.12	4.03 (+0.02)	24.5
Methane	111	7.24 (+0.05)	11.72	5.17 (+0.03)	19.52
<i>n</i> -Butane	298	1.89 (+0.05)	31.46	0	54.98
<i>n</i> -Butane	303	0.74 (+0.5)	38.21	0.14 (+0.5)	65.2

The accuracy of determination of Δn_{NGA} depends on the resolution of the isotherm. The errors provided in Supplementary Table 9 represent the step size and give an indication of what the maximum Δn_{NGA} could be for higher resolution isotherm.

3.5 *In situ* calorimetry

For microcalorimetry, all isotherms and enthalpies were measured experimentally using a Tian-Calvet type microcalorimeter coupled with a home-made manometric gas dosing system²⁰. This apparatus allows the simultaneous measurement of the adsorption isotherm and the corresponding differential enthalpies. Gas is introduced into the system using a step-by-step method and each dose is allowed to stabilize in a reference volume before being brought into contact with the adsorbent located in the microcalorimeter. The introduction of the adsorbate to the sample is accompanied by an exothermic thermal signal, measured by the thermopiles of the microcalorimeter. The peak in the calorimetric signal is integrated over time to give the total energy released during this adsorption step. Around 0.05 g of sample is used in each experiment. For each injection of gas, equilibrium was assumed to have been reached after 130 minutes. This was confirmed by the return of the calorimetric signal to its baseline ($< 5 \mu\text{W}$). The gases used for the adsorption experiment were obtained from Air Liquide and were of minimum N47 quality (99.997 % purity).

To obtain the experimental errors, the procedure described in the *Guide to the Expression of Uncertainty in Measurement* was used. The quantity, enthalpy or pressure, is first expressed as a function $f(y)$ of other physical measured quantities. The standard uncertainty ($u_c(y)$) is then calculated on the basis of, where $u_i(x_i)$ is the standard uncertainty in each input quantity. Here it is assumed that the input quantities are independent and uncorrelated. The error margins (a_i) for each quantity were taken from manufacturer specifications of the equipment used for recording. They were then divided by a value k_i chosen to cover the expected variance in that quantity, as each variable is assumed to be characterized by a probability distribution. The error introduced by the equation of state used (NIST REFPROP²¹) were assumed to be

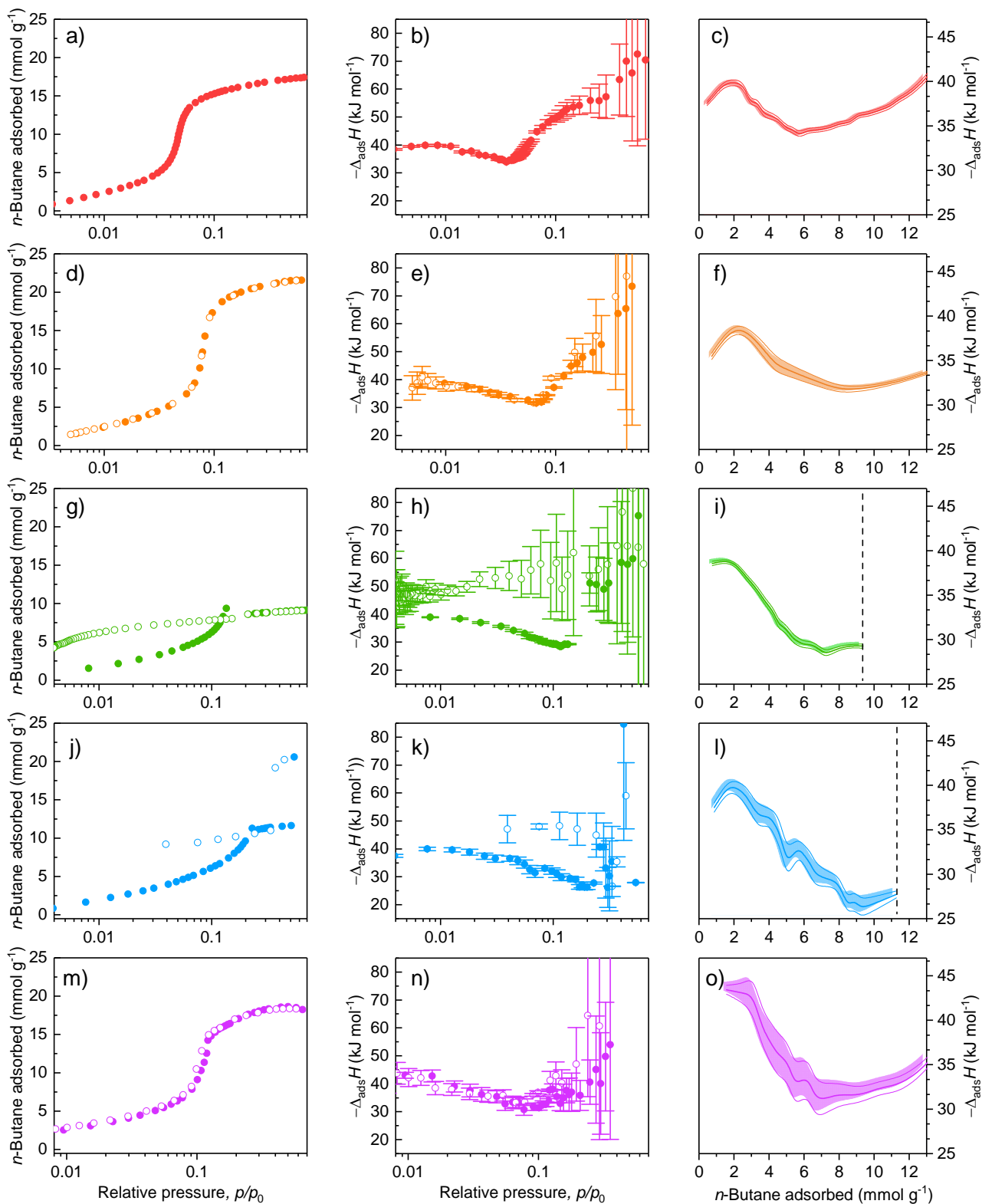
minor compared to the error introduced by the physical quantities, with the same to be said regarding the error in the calorimetric heat signal, which represents less than 1% of the error in enthalpy. Finally, the expanded uncertainty was calculated by choosing a suitable coverage factor of 1.645, corresponding to a 95% confidence interval.

$$f(y) = f(N_1, N_2 \dots N_i) \quad (1)$$

$$u_c(y) = \sqrt{\sum_{i=1}^N \left(\frac{\partial f(y)}{\partial x_i} \times u_i(x_i) \right)^2} \quad (2)$$

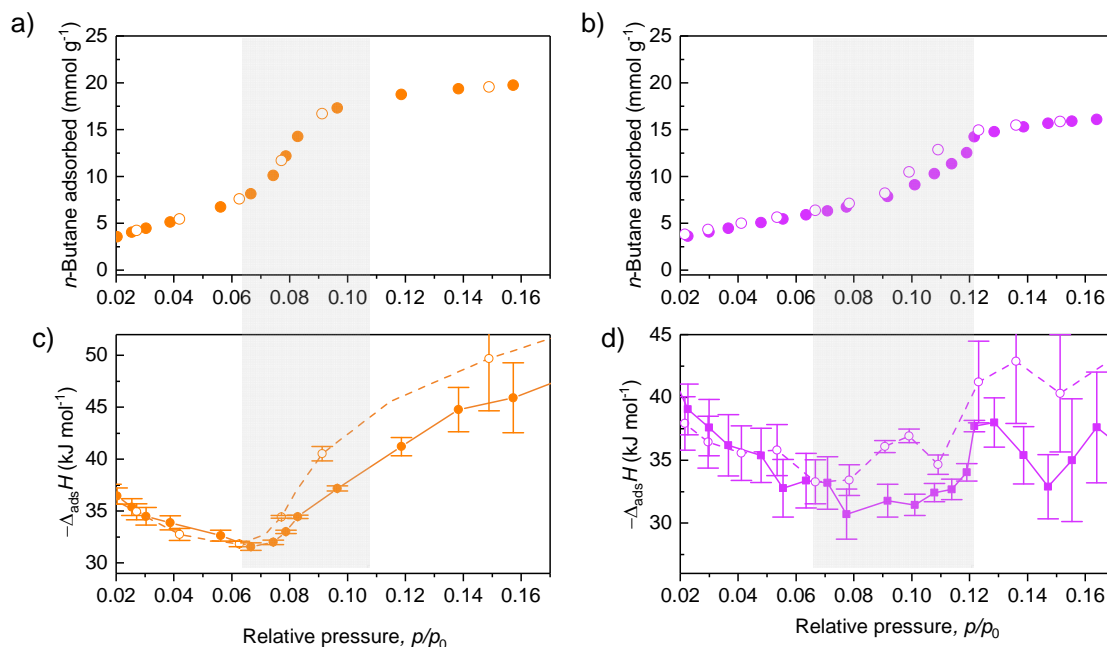
Supplementary Table 10. Parameters used to estimate the errors of *in situ* calorimetric analysis.

Variable (<i>i</i>)	a_i	k_i
Pressure, p (Pa)	20	$\sqrt{3}$
Temperature, T (K)	0.1	3
Sample mass, m (g)	1×10^{-4}	$\sqrt{3}$
Reference volume, V_r (m ³)	1×10^{-9}	$\sqrt{6}$
Cell volume, V_c (m ³)	6×10^{-7}	$\sqrt{6}$



Supplementary Figure 15. Adsorption (filled symbol) and desorption (empty symbol) isotherm of *n*-butane at 303 K (left), corresponding adsorption/desorption enthalpies and error bars (middle), and isosteric adsorption enthalpy profiles with semi-transparent error region (right) of a-c) DUT-48, d-f) DUT-46, g-i) DUT-49, j-l) DUT-50, m-o) DUT-151_{int}. dashed lines in i) and l) indicate NGA transition and enthalpies beyond this loading were removed for clarity.

In DUT-46 and DUT-151*int* small hystereses were observed in the enthalpy profile. In the case of DUT-151*int* this can be correlated to a structural transition analysed by in situ PXRD and reflected by a hysteresis in the adsorption isotherm. No hysteresis in the adsorption/desorption isotherms and no structural transition can be observed in the pressure range in which a hysteresis is observed in the enthalpy profile.



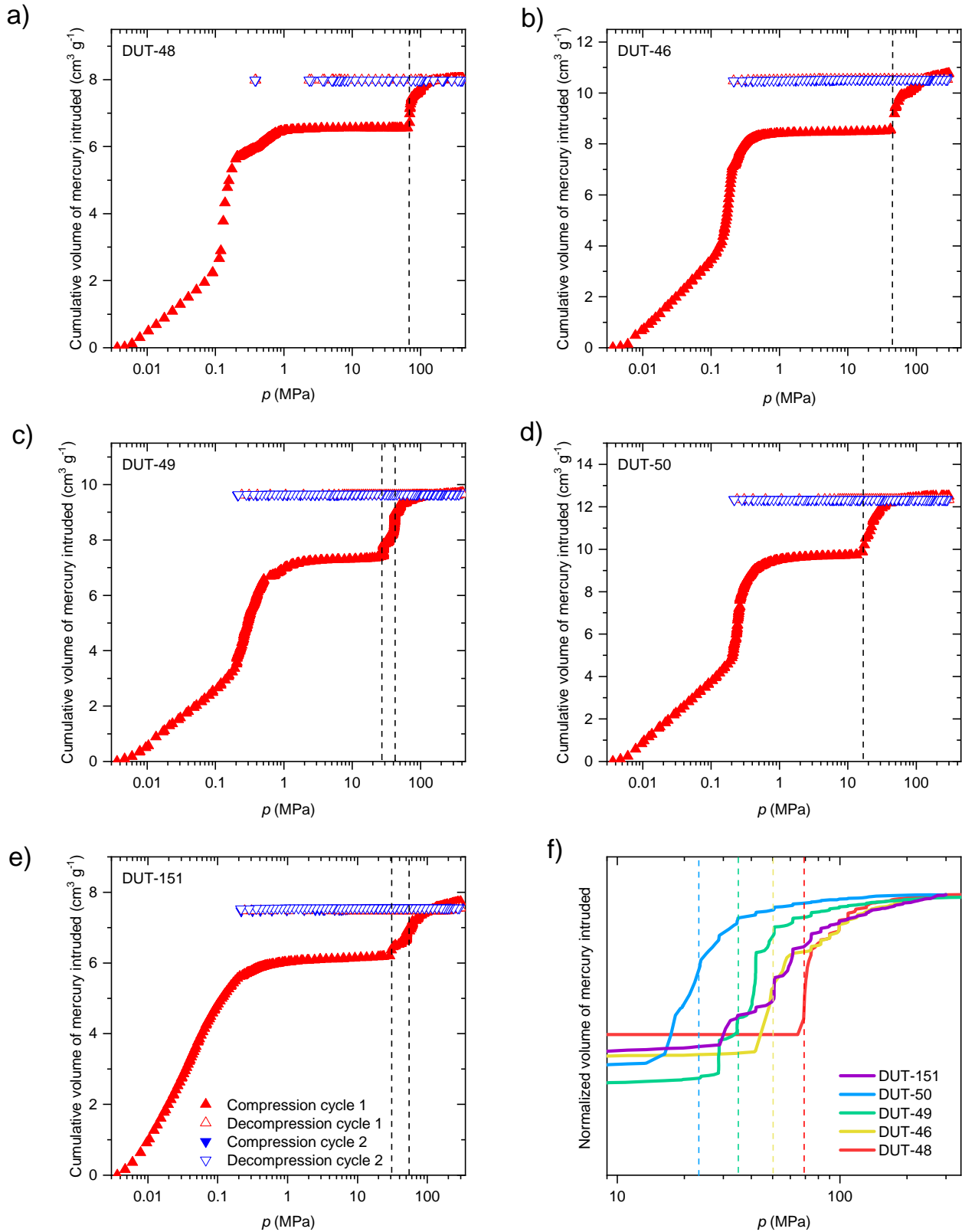
Supplementary Figure 16. Adsorption (filled symbol) and desorption (empty symbol) isotherm of *n*-butane at 303 K for a) DUT-46 and b) DUT-151*int* with corresponding adsorption/desorption enthalpies and error bars for c) DUT-46 and d) DUT-151*int*. grey region indicate hysteresis in enthalpy profiles.

3.6 Mercury intrusion

Mercury intrusion is a method frequently applied to investigate the mechanical properties and structural contraction of metal organic frameworks.²²⁻²⁷ To begin with, the solids were activated at 115°C for 8 h in secondary vacuum. The obtained powder was then loaded into a powder penetrometer of 3.1126 cm³ volume with a stem volume of 0.412 cm³ using a glove box (Jacomex P-BOX) under argon atmosphere H₂O < 5 ppm. The mercury intrusion experiments were carried out using a Micromeritics AutoPore IV 9500 allowing a range of pressure applied from 0.003 to 300 MPa. Prior to the experiment the powder was outgassed in vacuum at ~6.5 Pa for 15 minutes. The collected volume of mercury intruded was corrected by a blank measurement recorded under the same conditions (temperature and pressure) using the same penetrometer to obtain the absolute contracted volume as a function of the pressure reported in Supplementary Figure 17. The resulting volume change upon structural contraction can be determined from the cumulative volume of mercury intruded obtained by mercury intrusion using equation (3):

$$V_{cp} = V_{op} - \frac{Z \times M \times (V_{final} - V_{initial}) \times 10^{24}}{N_A} \quad (3)$$

where V_{cp} and V_{op} are the volumes of the contracted and open phases respectively in \AA^3 , Z the number of formula units per unit cell (in the case of the investigated materials $Z = 24$), M is the molar mass of a formula unit in g mol^{-1} derived from the crystal structure, V_{final} and $V_{initial}$ the cumulative volumes of mercury intruded at the end (last point of the second plateau) and at the beginning of the transition (end of the first plateau) in ml g^{-1} and N_A is Avogadro's constant in mol^{-1} .



Supplementary Figure 17. Mercury intrusion curves for DUT-48 (a), DUT-46 (b), DUT-49 (c), DUT-50 (d), DUT-151 (e), and f) comparison of the intrusion curves with transition pressures indicated as dashed lines.

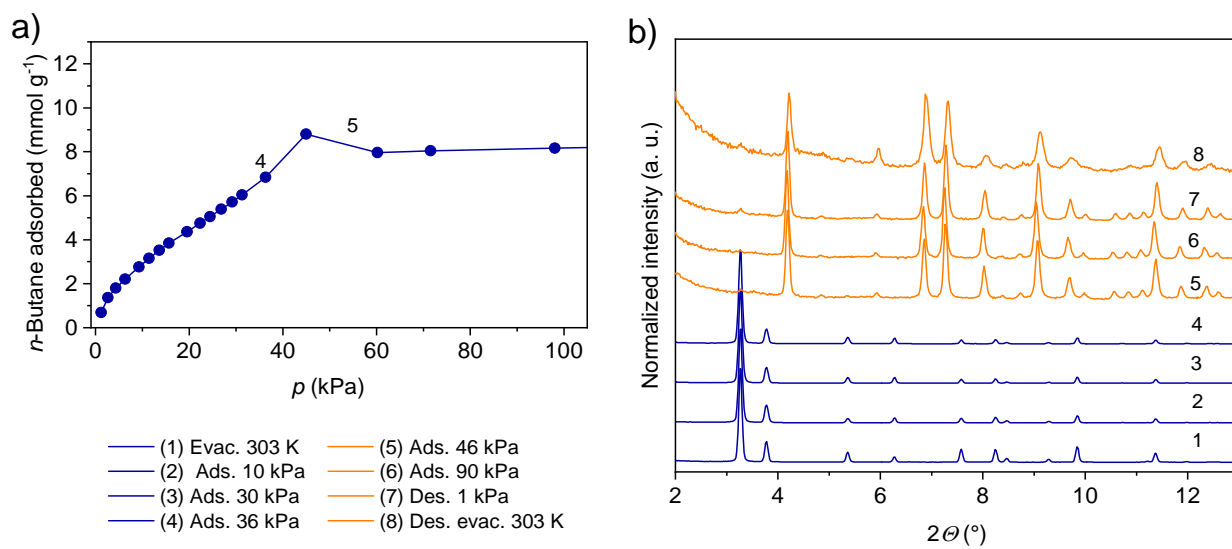
Supplementary Table 11. Summary of experimental details of Hg intrusion and comparison with simulated results.

	Pore volume (cm ³ g ⁻¹)	Volume change Hg intrusion total (cm ³ g ⁻¹)	Volume change Hg intrusion total (%)	ΔV simulation <i>op</i> - <i>cp</i> (%)	Transition pressure measured (MPa)	Transition pressure simulated (MPa)
DUT-48	1.98	1.5	63.7	44.0	65	145
DUT-46	2.153	2.01	77.8	47.2	50	84
DUT-49	2.89	2.30	71.8	51.4	35	65
DUT-50	4.02	2.78	65.3	59.2	24	38
DUT-151	n. a.	n. a.	n. a.	62.5	n. a.	22
DUT-151 <i>int</i>	1.891	1.53	56.4	27.9	29	n. a.

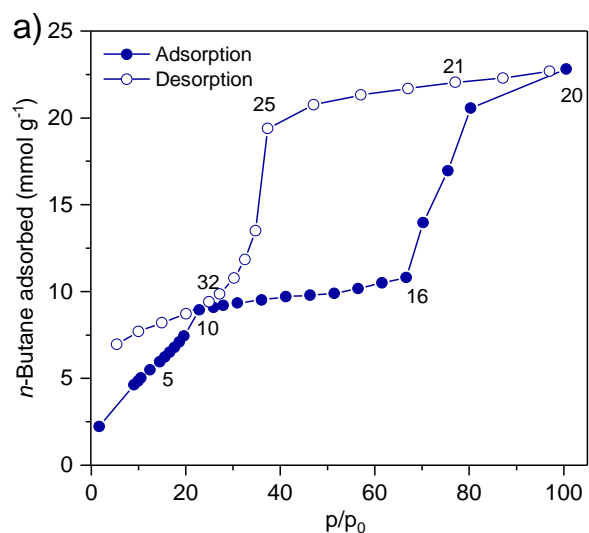
3.7 *In situ*-PXRD investigations

3.7.1 *Experimental details*

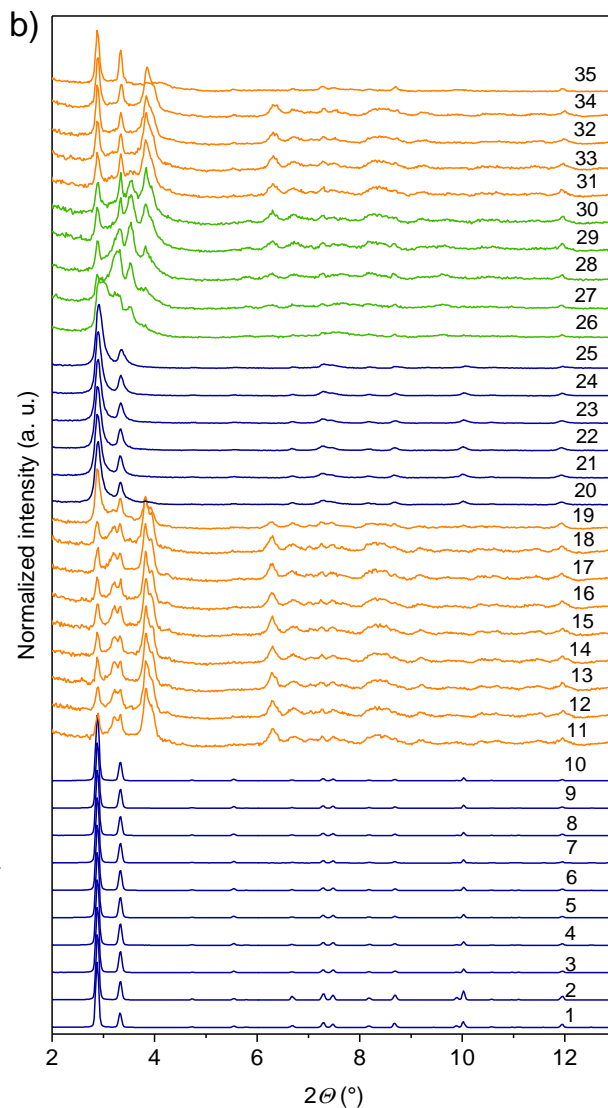
In situ-PXRD studies and parallelised gas adsorption were measured at KMC-2 beamline²⁸ of the BESSY II synchrotron, operated by Helmholtz-Zentrum Berlin für Materialien und Energie. Self-designed automated instrumentation, based on the volumetric adsorption instrument and closed-cycle Helium cryostat, equipped with adsorption chamber with beryllium domes was used in all experiments.²⁹ PXRD patterns were measured at constant wavelength $\lambda = 0.15406$ nm ($E = 8038$ eV) in transmission geometry. Because of the bulky cryostat, the sample holder cannot rotate during experiments, however an average crystallite size in the range of 2-15 μ m and using an area 2D detector (Vantec 2000, Bruker) allowed to record diffraction images with reasonable particle statistics. Each 2D image was measured with 31 s exposure. For each experiment 10-12 mg of sample were used. In order to block the reflections coming from the crystalline Be-dome, a tungsten aperture with 5 mm opening was mounted on the detector cone. The obtained diffraction images were integrated using DATASQUEEZE 2.2.9³⁰ with further processing in FITYK 0.9³¹ software. PXRD patterns, measured for DUT-50 during adsorption and desorption of methane at 111 K (Supplementary Figure 20) and *n*-butane at 273 K (Supplementary Figure 19) were obtained in the automatic mode in parallel to the isotherm measurement. The dataset of DUT-151*int* tracking the adsorption and desorption of *n*-butane at 273 K was collected in the automated modus as well (Supplementary Figure 22). For all automated measurements the physisorption isotherms were measured using equilibrium settings for pressure change of 0.1% within 300 s. The dataset during *n*-butane adsorption at 303 K (Supplementary Figure 18) as well as the analysis of DUT-151*int* at 273 K (Supplementary Figure 22) was measured in the manual mode. Each pressure was set manually and PXRD patterns were measured after the pressure in the cell was stabilized for at least 300 s.



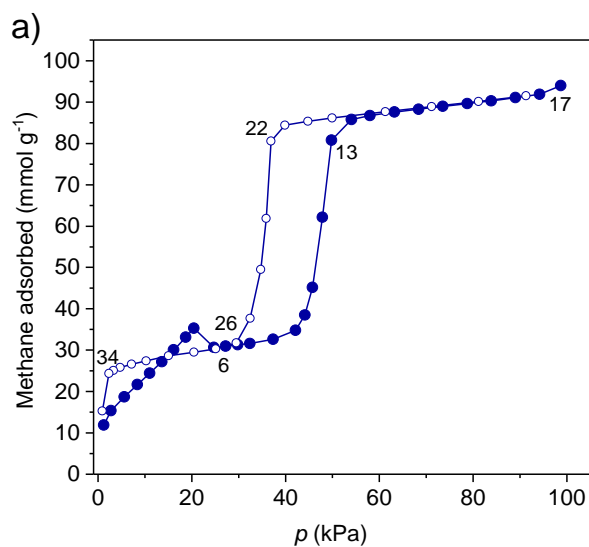
Supplementary Figure 18. *In situ*-PXRD data for DUT-49: a) *n*-butane adsorption isotherm at 303 K and corresponding PXRD patterns at varying pressures.



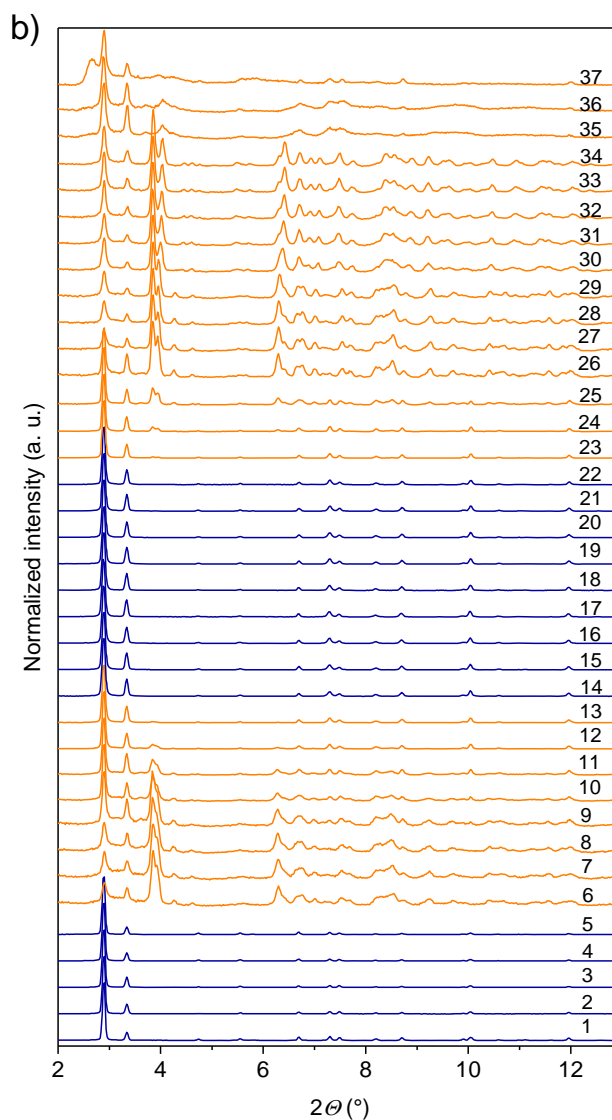
(1) evac 273 K	(21) Des. 77.02 kPa
(2) Ads. 10.49 kPa	(22) Des. 57.03 kPa
(3) Ads. 12.44 kPa	(23) Des. 47.09 kPa
(4) Ads. 14.48 kPa	(24) Des. 37.37 kPa
(5) Ads. 15.58 kPa	(25) Des. 34.80 kPa
(6) Ads. 16.59 kPa	(26) Des. 32.52 kPa
(7) Ads. 17.62 kPa	(27) Des. 30.24 kPa
(8) Ads. 18.63 kPa	(28) Des. 27.19 kPa
(9) Ads. 19.64 kPa	(29) Des. 24.91 kPa
(10) Ads. 22.88 kPa	(30) Des. 20.06 kPa
(11) Ads. 25.86 kPa	(31) Des. 14.97 kPa
(12) Ads. 27.91 kPa	(32) Des. 10.04 kPa
(13) Ads. 30.96 kPa	(33) Des. 5.43 kPa
(14) Ads. 36.05 kPa	(34) evac. 298 Des. evac. 27
(15) Ads. 41.16 kPa	(35) Des. evac. 298 K
(16) Ads. 56.45 kPa	
(17) Ads. 61.53 kPa	
(18) Ads. 70.23 kPa	
(19) Ads. 80.28 kPa	
(20) Ads. 100.5 kPa	



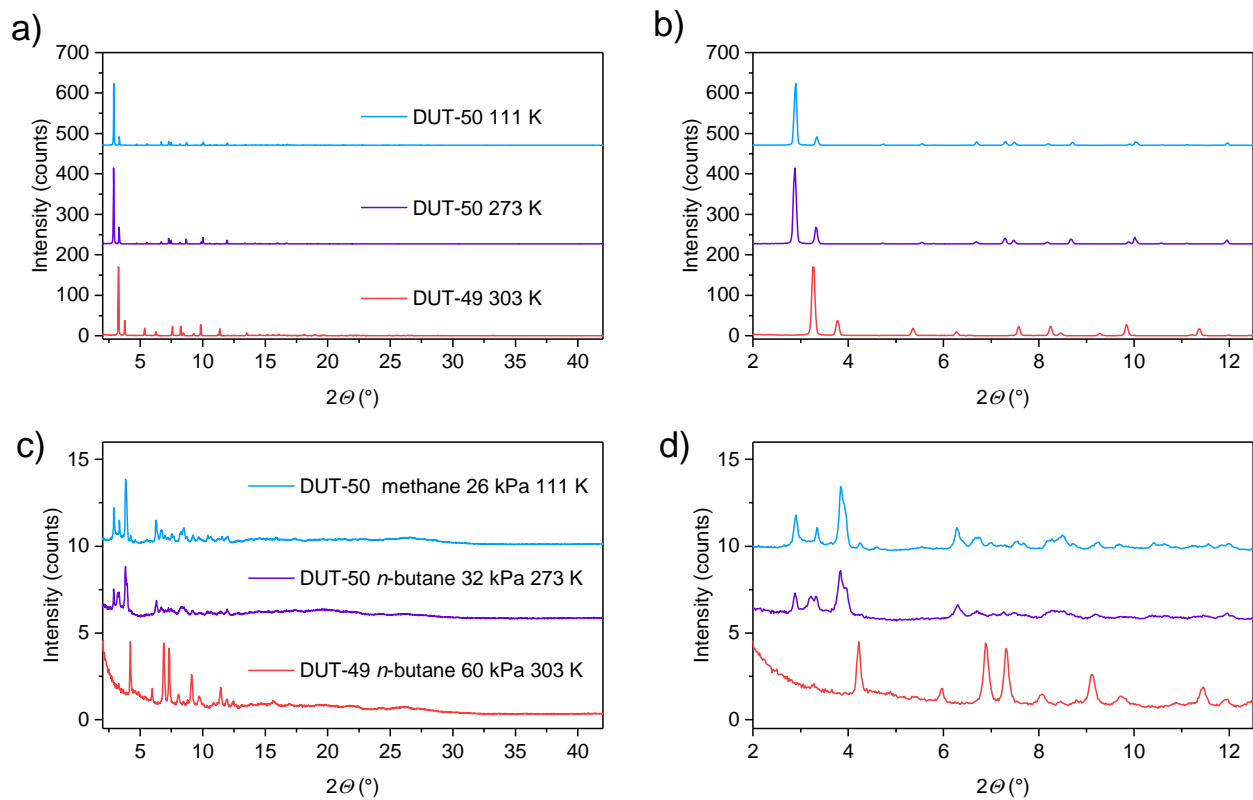
Supplementary Figure 19. DUT-50 *in situ*-PXRD dataset with a) *n*-butane isotherm at 273 K and corresponding PXRD patterns at varying pressures. Filled symbols: adsorption, empty symbols: desorption.



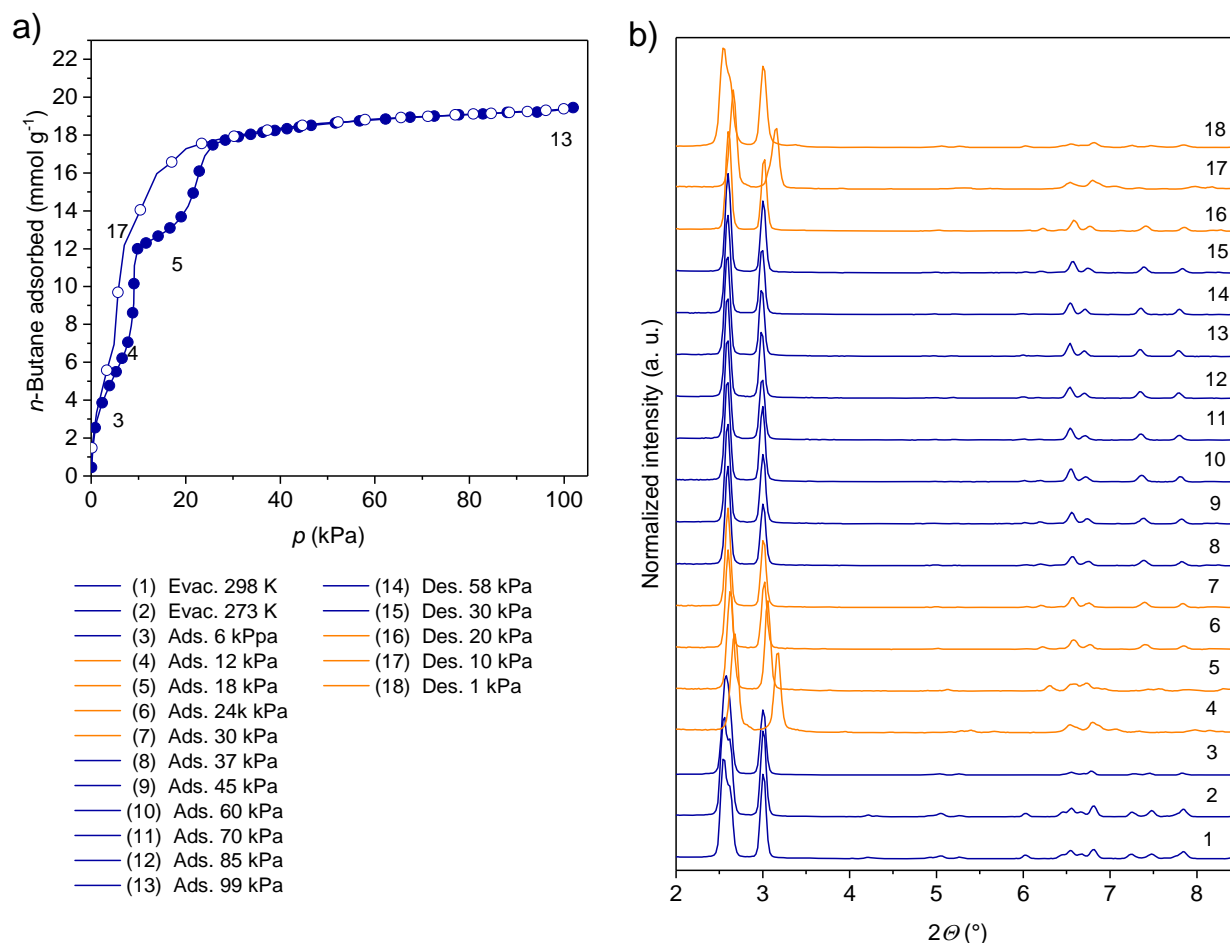
- | | |
|-------------------|-------------------|
| (1) evac. 111 K | (18) 61.3 kPa des |
| (2) 1.2 kPa ads | (19) 49.9 kPa des |
| (3) 5.6 kPa ads | (20) 44.8 kPa des |
| (4) 11.0 kPa ads | (21) 39.9 kPa des |
| (5) 16.1 kPa ads | (22) 36.9 kPa des |
| (6) 27.2 kPa ads | (23) 35.8 kPa des |
| (7) 29.8 kPa ads | (24) 34.7 kPa des |
| (8) 37.3 kPa ads | (25) 32.4 kPa des |
| (9) 42.1 kPa ads | (26) 29.5 kPa des |
| (10) 44.2 kPa ads | (27) 25.1 kPa des |
| (11) 45.8 kPa ads | (28) 20.5 kPa des |
| (12) 47.9 kPa ads | (29) 15.0 kPa des |
| (13) 49.8 kPa ads | (30) 10.2 kPa des |
| (14) 58.0 kPa ads | (31) 7.1 kPa des |
| (15) 63.2 kPa ads | (32) 4.7 kPa des |
| (16) 73.6 kPa ads | (33) 3.2 kPa des |
| (17) 98.8 kPa ads | (34) 2.3 kPa des |
| | (35) 0.8 kPa des |
| | (36) evac. 111 K |
| | (37) evac. 298 K |



Supplementary Figure 20. DUT-50 *in situ*-PXRD dataset with a) methane isotherm at 111 K and corresponding PXRD patterns at varying pressures. Filled symbols: adsorption, empty symbols: desorption.



Supplementary Figure 21. Comparison of PXRD patterns of DUT-49 and DUT-50 in a,b) open pore, and c,d) in contracted pore (offset is 220 counts in a,b and 5 counts in c,d).



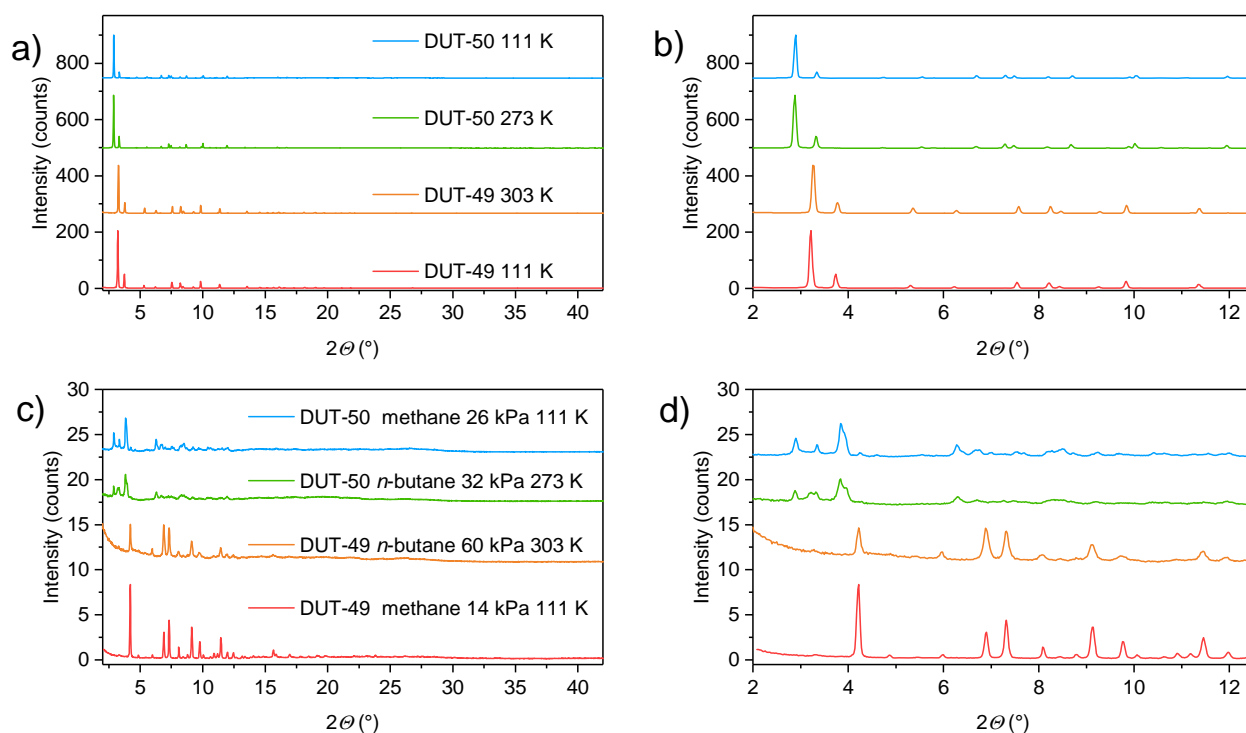
Supplementary Figure 22. DUT-151int *in situ*-PXRD dataset with a) *n*-butane at 273 K and corresponding PXRD patterns at varying pressures. Filled symbols: adsorption, empty symbols: desorption.

3.7.2 Le Bail fit and Rietveld refinement of PXRD Data

3.7.2.1 DUT-50

In situ PXRD pattern of DUT-50 show a peak broadening and reduced crystallinity upon adsorption of *n*-butane at 20 kPa and 273 K indicating the formation of *cp* phase. At elevated pressure the peaks of the pristine *op* phase reappear reflecting the reversible reopening of the structure and indicating a rare crystalline-disordered-crystalline transition. Upon desorption, the *op* phase undergoes contraction at 25 kPa without indications for reopening at lower pressure. The fact that DUT-50*cp* completely reopens at higher pressures suggests that the framework connectivity is preserved and is an evidence for a cooperative transformation within a single crystal.

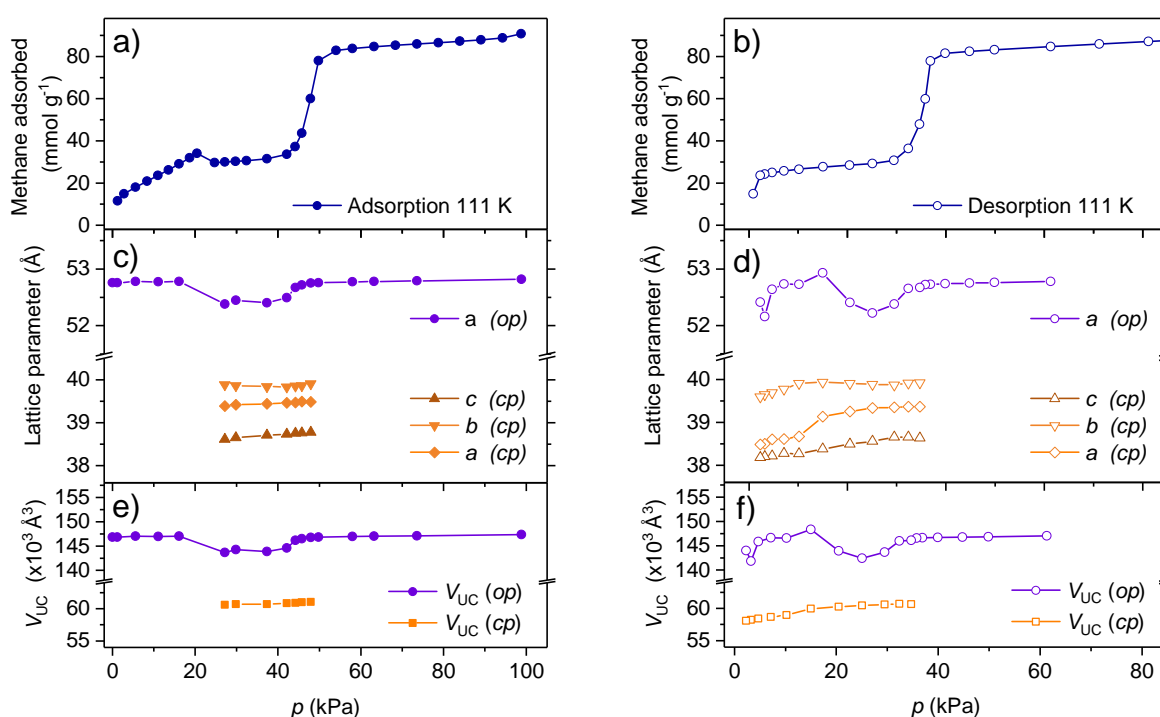
In situ PXRD patterns, measured for DUT-50 during the adsorption of methane at 111 K show enhanced diffraction intensities and improved pattern quality (Supplementary Figure 23) and were thus subjected to detailed analysis involving indexing and full pattern decomposition using Le Bail fit³², implemented into the FullProf software³³.



Supplementary Figure 23. Comparison of PXRD patterns of DUT-49 and DUT-50 in a,b) open pore, and c,d) in contracted pore upon adsorption of *n*-butane and methane at 111 and 303 K. a,c) wide angle diffractogram; b,d) magnification of small angle region.

The presence of a second set of reflections different from that of DUT-50_{op} after contraction could be attributed to DUT-50_{cp}. PXRD patterns measured during adsorption of methane between 0 and 16 kPa show phase pure DUT-50_{op}. After the phase transition and NGA at 20 kPa, the PXRD patterns become more complex in comparison with DUT-49. Firstly, only part of the bulk is transformed into the *cp* phase, with peaks of the *op* phase present in PXRD patterns throughout the whole pressure range. The most probable reason for this behaviour are crystallite size effects which have been shown to result in phase mixtures upon adsorption of nitrogen in DUT-49⁷. Secondly, in the pressure range of 21-45 kPa during adsorption in which the *cp* phase is present, the PXRD patterns reflect low crystallinity and peak broadening at higher 2θ angles in comparison with PXRD patterns of *op* phase at lower pressures. Thirdly, the measured PXRD pattern of DUT-50_{cp} contains two reflections in the 2θ range of $3.7 - 4.1^\circ$ with different splitting dependent on the gas pressure in the cell. *Ab initio* indexing of PXRD patterns was difficult due to the present phase mixture and peak broadening. Therefore, an empirical analysis of the experimental PXRD patterns by using calculated PXRD patterns from simulated DUT-50_{cp} phase in $Pa\bar{3}$ symmetry – the symmetry of DUT-49_{cp} – and lattice parameter of 38.29 Å was performed. The reflection in the range of $3.7-4.1^\circ$ of the simulated cubic unit cell with index (111) represents the interplanar distances between the space diagonals of the cubic unit cell. The splitting of the reflection can be a sign of inequality of the space diagonals in the unit cell which is only possible in non-orthogonal unit cells. Therefore, the symmetry was first reduced to rhombohedral ($R\bar{3}$), however no satisfactory Le Bail fit could be obtained at larger splitting of the peak. Consequently, the symmetry of the space group was

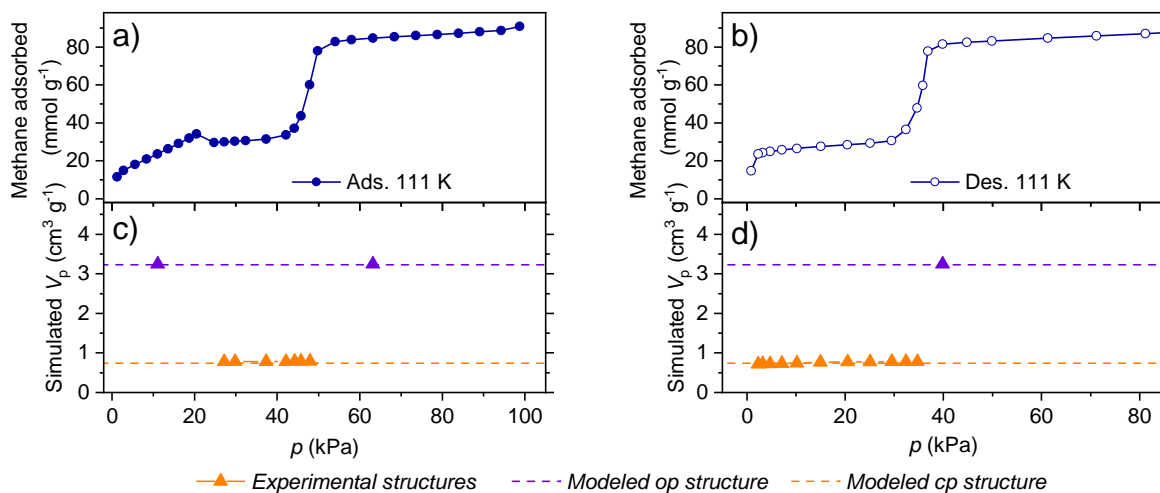
further reduced to monoclinic $P2_1/c$ for which the multiphase Le Bail fit resulted in reasonable reliability factors. Therefore, the whole series of measured *in situ* PXRD patterns of DUT-50 upon adsorption and desorption of methane at 111 K was subjected to profile matching procedure with constant scale factor. The PXRD profile was modelled using pseudo-Voigt function with axial divergence and asymmetry of reflections was additionally treated using Berar-Baldinazzi function in Material Studio³⁴. The background was refined as linear interpolation between a set of background points with reliable heights. No zero-line shift was refined during the fitting. The obtained unit cell parameters are very close to the theoretically predicted model ranging from 38.18 to 39.49 Å. The monoclinic angle, inducing the splitting of (111) and (11-1) reflections is gas pressure-dependent and ranges from 92.2° to 93.9°. The evolution of unit cell parameter is summarized in Supplementary Table 12 and displayed in Supplementary Figure 24.



Supplementary Figure 24. a) Adsorption (filled symbols) and desorption (empty symbols) isotherm of methane at 111 K of DUT-50. c,d) Lattice parameter evolution of DUT-50 upon adsorption (c) and desorption (d) of the *op* phase (cubic symmetry $Fm\bar{3}m$) and *cp* phase (monoclinic symmetry $P2_1/c$). *op* phase is shown as purple circles, *cp* phases as orange triangles and squares.

The evolution of the unit cell volume is very similar to DUT-49 with a decrease of 58% upon structural contraction. In addition, the residual *op* phase undergoes minor contraction in the range of 25 – 45 kPa and a complete reopening of the *cp* phases can be observed at pressures beyond 50 kPa. During desorption, the *op* phase is found to transform into the *cp* phase at 38 kPa and the unit cell parameter and volume is found to decrease with decreasing pressure. Residual *op* phase is observed throughout the whole investigated pressure range. Interestingly, the unit cell volume of the *op* phase is slightly reduced in the range of 20-30 kPa. This indicates that the residual *op* phase also exhibits a structural response to the adsorption-induced stress upon adsorption and desorption but to a minor extent. Rietveld analysis of the experimental PXRD patterns of *cp* phase was not possible due to the poor quality and present phase

mixture. Consequently, structural models on the basis of the symmetry and lattice parameter refined by Le Bail methods were constructed and optimized with Materials Studio³⁴. For this set of quasi-experimental structures the specific pore volume for the simulated structures of DUT-50 op and cp was subsequently calculated using Zeo++¹⁶ software (in detail described below). Comparison of the simulated specific pore volume of the quasi-experimental structures with the modelled structures based on MD simulation show good agreement for both op and cp phase (Supplementary Figure 25).



Supplementary Figure 25. a) Adsorption (filled symbols) and desorption (empty symbols) isotherm of methane at 111 K of DUT-50. c,d) Evolution of simulated pore volume (using Zeo++) of DUT-50 upon adsorption (c) and desorption (d) of the op phase (purple) and cp phase (orange). Simulated pore volumes of the structural models determined by MD simulations are given as horizontal dashed lines.

Supplementary Table 12. Data obtained from Le Bail refinement of PXRD patterns collected during adsorption of methane at 111 K in DUT-50.

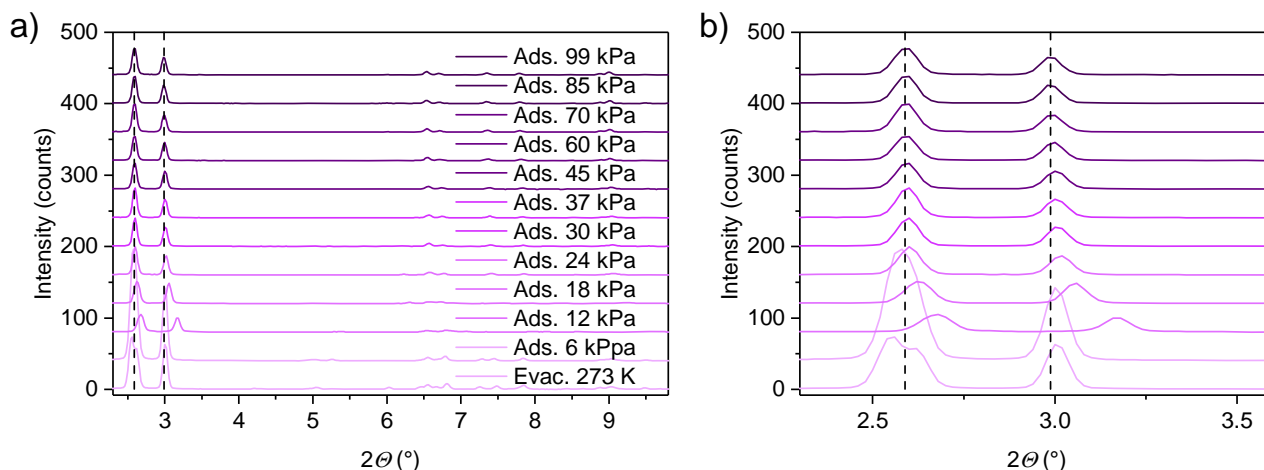
<i>P</i> (kPa)	Pattern No (Supplementary Figure 22)	DUT-50 <i>op</i> (<i>Fm</i> $\bar{3}m$)		DUT-50 <i>cp</i> (<i>P2</i> ₁ / <i>c</i>)					<i>R</i> _p (%)	<i>R</i> _w _p (%)
		<i>a</i> (Å)	<i>V</i> (Å ³)	<i>a</i> (Å)	<i>b</i> (Å)	<i>c</i> (Å)	β (°)	<i>V</i> (Å ³)		
Evac. 111K	1	52.756 (1)	146833	-	-	-	-	-	7.98	12.90
1.2	2	52.756 (1)	146830	-	-	-	-	-	7.68	12.70
5.6	3	52.777(1)	147009	-	-	-	-	-	7.95	12.70
11.1	4	52.775(1)	146988	-	-	-	-	-	8.01	13.10
16.1	5	52.779(1)	147020	-	-	-	-	-	8.43	13.60
27.2	6	52.380(1)	143709	38.611(3)	39.886(2)	39.384(2)	92.12(1)	60611(6)	3.60	5.56
29.8	7	52.445(4)	144252	38.651(3)	39.862 (2)	39.419 (3)	92.03 (1)	60695(6)	3.62	5.36
37.3	8	52.401(5)	143887	38.713(2)	39.841(2)	39.436(2)	92.08(1)	60684(6)	3.50	5.51
42.1	9	52.491(3)	144629	38.728(2)	39.830(2)	39.463(2)	92.08(1)	60832(6)	3.71	5.70
44.2	10	52.674(2)	146151	38.751(3)	39.854(3)	39.470(2)	92.08(1)	60915(6)	3.71	5.81
45.8	11	52.720(1)	146527	38.763(2)	39.863 (2)	39.494(2)	92.04 (1)	60987(6)	3.82	5.87
47.9	12	52.751(1)	146789	38.777 (2)	39.910(3)	39.486 (3)	92.02 (1)	61070(7)	4.05	6.60
49.8	13	52.756(1)	146829	-	-	-	-	-	6.55	10.20
58.0	14	52.773(1)	146974	-	-	-	-	-	7.01	10.80
63.2	15	52.780(1)	147031	-	-	-	-	-	6.08	9.39
73.6	16	52.792(1)	147128	-	-	-	-	-	6.86	10.20
98.8	17	52.816(1)	147335	-	-	-	-	-	7.97	11.40

Supplementary Table 13. Data obtained from Le Bail refinement of PXRD patterns collected during desorption of methane at 111 K in DUT-50.

<i>p</i> (kPa)	Pattern No (Supplementary Figure 22)	DUT-50 <i>op</i> (<i>Fm</i> $\bar{3}$ <i>m</i>)		DUT-50 <i>cp</i> (<i>P2</i> ₁ / <i>c</i>)					<i>R_p</i> (%)	<i>R_{wp}</i> (%)
		Lattice parameter <i>a</i> , Å	<i>V</i> (Å ³)	<i>a</i> (Å)	<i>b</i> (Å)	<i>c</i> (Å)	β (°)	<i>V</i> (Å ³)		
61.3	18	52.779 (1)	147026	-	-	-	-	-	7.31	10.3
49.9	19	52.759 (1)	146857	-	-	-	-	-	6.57	9.56
44.8	20	52.749 (1)	146773	-	-	-	-	-	6.35	8.91
39.9	21	52.738(1)	146677	-	-	-	-	-	6.41	9.15
36.9	22	52.729 (1)	146608	-	-	-	-	-	6.65	9.31
35.8	23	52.723 (1)	146555	-	-	-	-	-	6.92	10.6
34.7	24	52.671 (1)	146125	38.633(2)	39.923(2)	39.368(2)	92.18 (1)	60673(3)	4.61	7.77
32.4	25	52.652(1)	145963	38.655(2)	39.918 (2)	39.365(2)	92.18(1)	60697(4)	3.90	6.42
29.5	26	52.377 (4)	143690	38.656 (3)	39.876(3)	39.354(2)	92.18 (1)	60618(6)	4.18	6.78
25.1	27	52.221(8)	142405	38.561(3)	39.887(3)	39.338 (2)	92.23 (1)	60459(7)	4.51	7.78
20.5	28	52.408(6)	143940	38.494(2)	39.907(2)	39.255(2)	92.31 (1)	60252(6)	4.12	7.05
15.0	29	52.933 (6)	148313	38.380 (2)	39.943(2)	39.138 (2)	92.41 (1)	59946(5)	3.98	6.52
10.2	30	52.727 (3)	146590	38.274(1)	39.909(1)	38.671(2)	93.21 (1)	58975(4)	3.32	4.95
7.1	31	52.735(3)	146652	38.281(1)	39.780(1)	38.614(2)	93.57(1)	58687(4)	3.25	4.70
4.7	32	52.637 (3)	145839	38.219 (1)	39.692(1)	38.604(2)	93.68 (1)	58440(4)	3.46	5.18
3.2	33	52.156(5)	141876	38.201 (2)	39.653 (2)	38.504 (2)	93.76(1)	58201(5)	3.59	5.16
2.3	34	52.413 (3)	143988	38.180(1)	39.601(1)	38.487(2)	93.78(1)	58062(4)	3.42	4.93

3.7.2.2 DUT-151int

The PXRD patterns obtained for DUT-151int after supercritical activation (DUT-151int-act) show a shift of peaks in the range of 2-3.5 ° to lower 2θ values and appearance of new reflections in comparison to the as made material are observed.

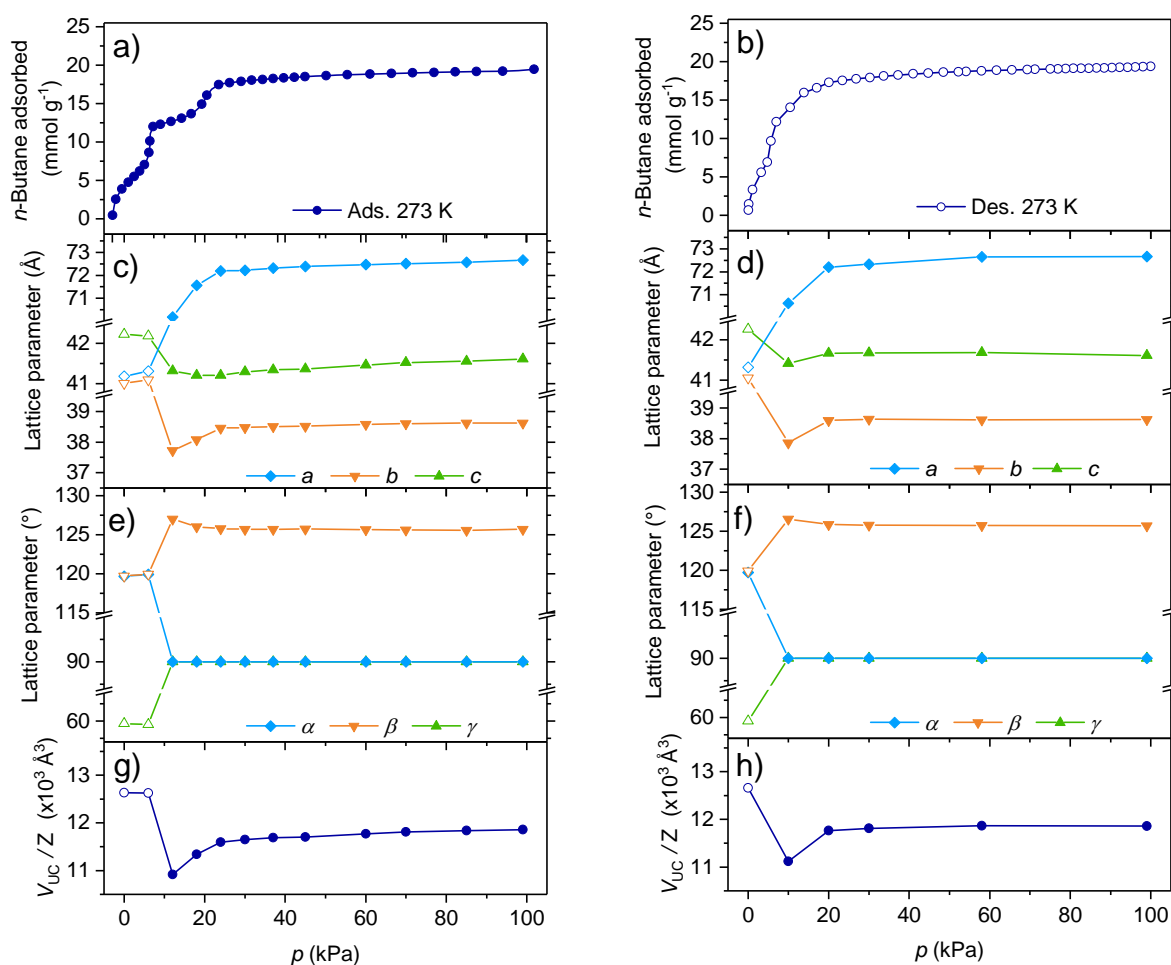


Supplementary Figure 26. a) PXRD patterns of DUT-151int upon loading with *n*-butane at 273 K and b) magnified small angle region. Dashed lines represent peak positions of DUT-151int.

This change can be assigned to a change in symmetry and unit cell volume upon solvent removal from monoclinic $C2/m$ (in solvated DUT-151int) to triclinic $P\bar{1}$ in DUT-151int-act determined by indexing of the PXRD pattern. At intermediate pressures in the range of 8 - 10 kPa, a step and hysteresis in the isotherm are observed. Indexing of *in situ* PXRD patterns in this pressure region shows that the symmetry of the unit cell is transformed to the initial monoclinic $C2/m$ space group, however the structure of DUT-151int-*cp* (87419 \AA^3) is found to be contracted by 14% in unit cell volume in comparison to DUT-151int (101103 \AA^3). The full list of cell parameter refined from the *in situ* PXRD data is displayed in Supplementary Table 14 and further illustrated in Supplementary Figure 27.

Supplementary Table 14. Le Bail fit of PXRD patterns (Supplementary Figure 22), measured *in situ* at 273 K during loading of *n*-butane.

p (kPa)	Space group	a (Å)	b (Å)	c (Å)	α (°)	β (°)	γ (°)	R_p	R_{wp}
Evac 298K	$P\bar{1}$	41.204(2)	40.981(2)	42.234(4)	119.62(1)	119.66(1)	59.66(6)	2.97	4.99
Evac 273	$P\bar{1}$	41.187(2)	41.013(3)	42.221(3)	119.67(1)	119.70(1)	59.64(1)	3.05	4.48
6 ads	$P\bar{1}$	41.313(3)	41.101(3)	42.183(2)	119.92(1)	119.95(1)	59.50(1)	4.44	9.54
12 ads	$C 2/m$	70.1749(62)	37.727(24)	41.3181(19)	90	127.02(1)	90	4.99	8.42
18 ads	$C 2/m$	71.557(3)	38.078(3)	41.207(2)	90	126.04(1)	90	4.90	7.29
24 ads	$C 2/m$	72.185(3)	38.455(3)	41.210(2)	90	125.79 (2)	90	5.49	10.90
30 ads	$C 2/m$	72.224(4)	38.483(4)	41.299(3)	90	125.70 (1)	90	5.87	12.1
37 ads	$C 2/m$	72.322(3)	38.515(3)	41.342(2)	90	125.72(1)	90	5.35	9.74
45 ads	$C 2/m$	72.387(3)	38.518(2)	41.371(2)	90	125.73(1)	90	5.09	9.18
60 ads	$C 2/m$	72.472(3)	38.583(3)	41.461(2)	90	125.67(1)	90	5.07	9.40
70 ads	$C 2/m$	72.512(3)	38.605(2)	41.525(2)	90	125.60(1)	90	5.34	10.10
85 ads	$C 2/m$	72.566(4)	38.623(3)	41.562(2)	90	125.60(1)	90	6.00	12.3
99 ads	$C 2/m$	72.673(2)	38.628(2)	41.613(1)	90	125.70(1)	90	4.87	8.58
58 des	$C 2/m$	72.657(2)	38.615(2)	41.686(1)	90	125.75(1)	90	4.87	8.59
30 des	$C 2/m$	72.336(3)	38.638(3)	41.679(2)	90	125.80(1)	90	5.00	9.86
20 des	$C 2/m$	72.203(3)	38.598(3)	41.671(2)	90	125.89(1)	90	5.07	9.38
10 des	$C 2/m$	70.624(6)	37.866(5)	41.415(3)	90	126.55(1)	90	5.81	9.46
1 des	$P\bar{1}$	41.318(4)	41.057(4)	42.266(4)	119.72(1)	119.91 (1)	59.49(1)	5.41	9.40
Single crystal	$C 2/m$	71.700(14)	41.570(8)	41.450(8)	90	125.08(3)	90	n. a.	n. a.



Supplementary Figure 27. a,b) Adsorption (closed symbols) and desorption (open symbols) isotherms of *n*-butane at 273 K. c-f) Corresponding lattice parameter evolution of the unit cells of DUT-151*int-act* (open symbols) and DUT-151*int-cp* and DUT-151*int-op* (closed symbols). e,f) Evolution of unit cell volume given in V_{UC} / Z to compare the volume evolution independent of the change in symmetry ($Z(int, op, cp) = 8, Z(act) = 4$). Tabulated values can be obtained from Supplementary Table 14.

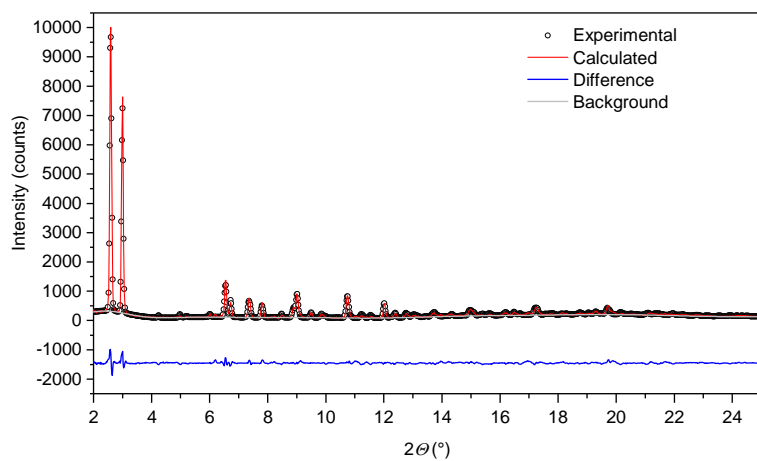
With increasing pressure, the unit cell volume and lattice parameters increase reaching a unit cell volume of DUT-151*int-op* (101740 \AA^3) in the range of the unit cell obtained from the single crystal analysis of solvated DUT-151*int*. Upon desorption of *n*-butane at 273 K and 298 K DUT-151*int-op* is found to transform back to DUT-151*int-cp* which then transforms back to the original structure of DUT-151*int-act*. In contrast to DUT-49 and DUT-50, the structural transitions in DUT-151*int* are found to be fully reversible.

The crystal structures of DUT-151*int-op*, DUT-151*int-cp*, and DUT-151*int-act* could further be refined by Rietveld methods and a procedure previously described for the refinement of DUT-50*cp* from the *in situ* PXRD patterns recorded at 60 kPa, 12 kPa and evacuated, respectively. Because of low symmetry of the structures, adsorbed *n*-butane molecules were not considered in the refinement. The Rietveld plots are displayed in Supplementary Figure 28 - Supplementary Figure 30. The main structural data are

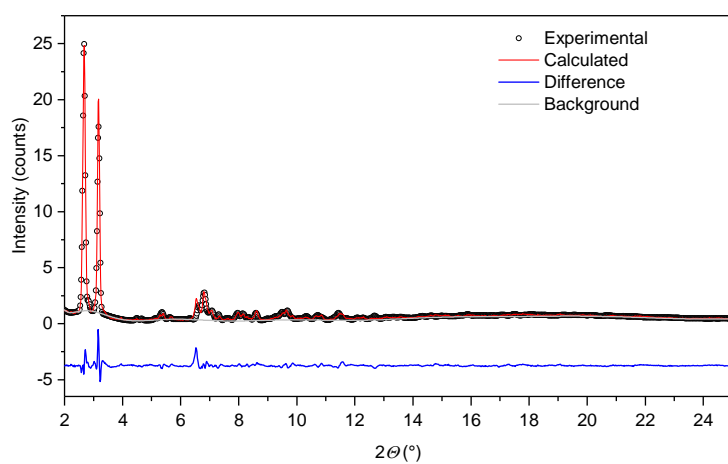
summarized in Supplementary Table 15. CCDC 1890381, 1890382, and 1890383 contain structural data for DUT-151*int-act*, DUT-151*int-cp* and DUT-151*int-op*, respectively.

Supplementary Table 15. Experimental structural data on DUT-151*int-act*, DUT-151*int-cp* and DUT-151*int-op*.

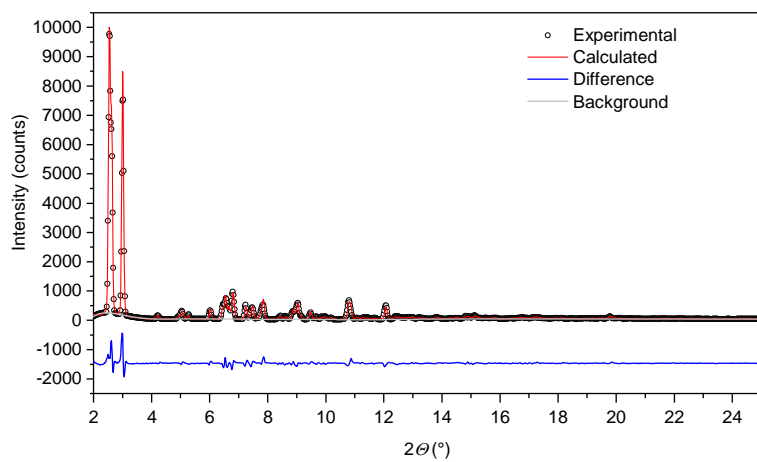
	DUT-151<i>int-act</i>	DUT-151<i>int-cp</i>	DUT-151<i>int-op</i>
Formula unit	C ₅₂ H ₂₈ Cu ₂ N ₂ O ₈	C ₅₂ H ₂₈ Cu ₂ N ₂ O ₈	C ₅₂ H ₂₈ Cu ₂ N ₂ O ₈
<i>Z</i>	12	24	24
Symmetry, space group	triclinic, <i>P</i> $\bar{1}$	monoclinic, <i>C2/m</i>	monoclinic, <i>C2/m</i>
Unit cell parameters			
<i>a</i> (Å)	41.193(1)	69.747(19)	71.598(3)
<i>b</i> (Å)	41.026(1)	37.990(12)	41.628(2)
<i>c</i> (Å)	42.227(1)	41.139(11)	41.667(2)
α , °	119.58(2)	90	90
β , °	119.78(3)	126.68(2)	124.99(2)
γ , °	59.46(2)	90	90
Unit cell volume, (Å ³)	50493(5)	87419(40)	101740(18)
Wave length (Å)		1.5406	
2θ range (°)		2 - 30	
Instrument geometry		Debye-Scherrer	
Zero point line shift (°)	0	0	0
Profile function		Thompson-Cox-Hastings	
<i>U</i>	0.02797	0.81789	0.0206
<i>V</i>	0.00371	0.03867	0.002
<i>W</i>	0.00507	0.00927	0.00447
<i>X</i>	0.01787	0.08439	0.08557
<i>Y</i>	0.00027	-0.00141	0.00105
Asymmetry correction		Berar-Baldinozzi	
<i>P1</i>	0.00280	0.00961	-0.00021
<i>P2</i>	0.00010	-0.00022	0.00018
<i>P3</i>	-0.00359	0.00412	-0.00074
<i>P4</i>	-0.00011	0.00005	-0.00001
Refined motion groups	42	70	70
Refined degrees of freedom	252	388	388
Final <i>R</i> -values			
Final <i>R</i> _{wp} %	14.53	12.56 %	9.42 %
Final <i>R</i> _p %	10.83	8.19 %	6.98 %



Supplementary Figure 28. Rietveld plot for DUT-151*int-act* evacuated at 273 K.

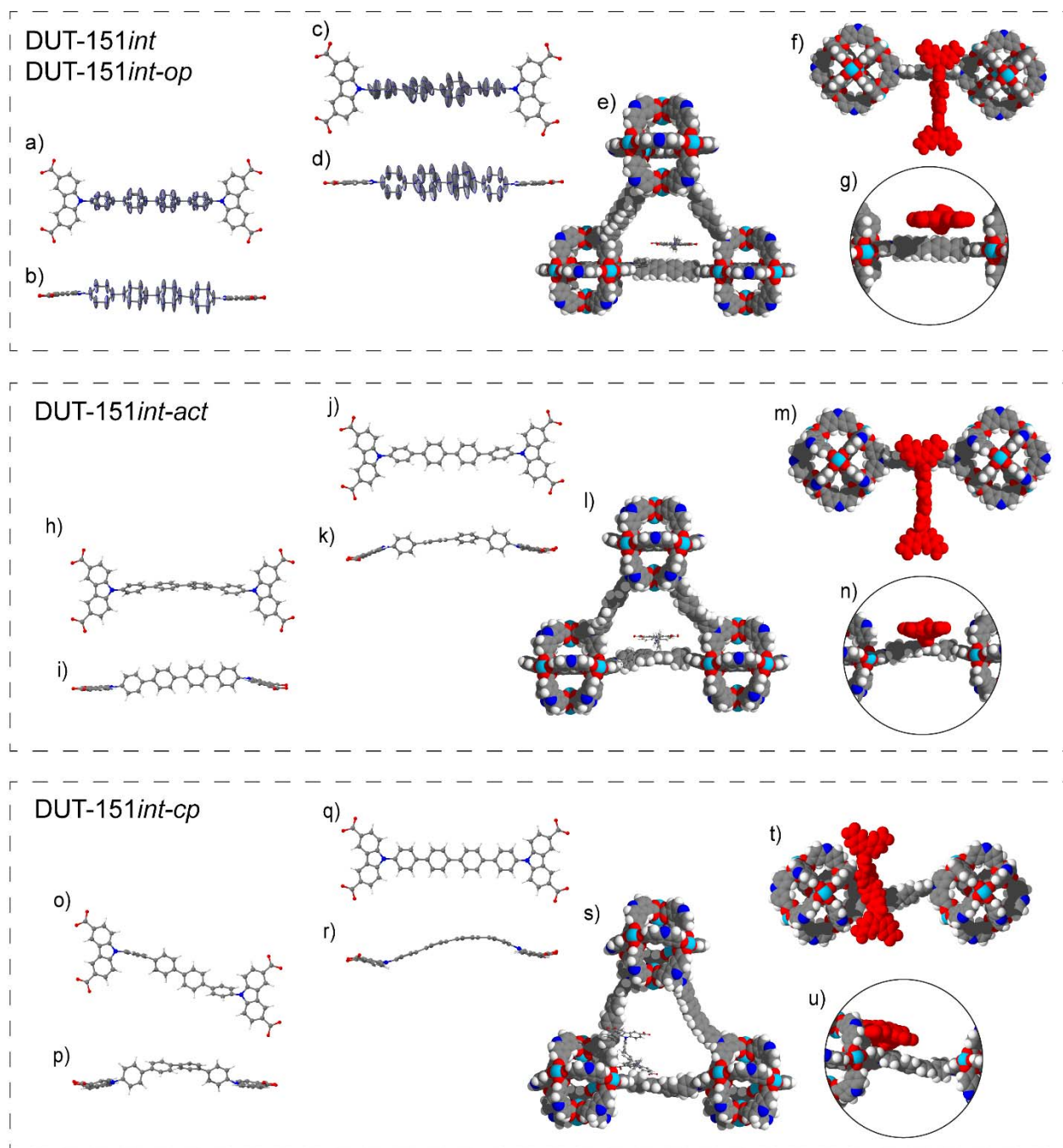


Supplementary Figure 29. Rietveld plot for DUT-151*int-cp* at 12 kPa *n*-butane adsorption at 273 K.



Supplementary Figure 30. Rietveld plot for DUT-151*int-op* at 60 kPa *n*-butane adsorption at 273 K.

Based on the refined structures and the single crystal structure of DUT-151*int* the structural transition in DUT-151*int* upon adsorption of *n*-butane at 273 K can be illustrated (Supplementary Figure 31).



Supplementary Figure 31. a-g) single crystal structure of DUT-151*int* (which is very similar to DUT-151*int-op*), a,c) top-view and b,d) side-view of two symmetrically independent ligands including thermal ellipsoid with 50% probability of occupancy of the bridging unit, e) tetrahedral window with ligand of secondary net in red, f) top-view, g) side-view. h-n) DUT-151*int-act* h,j) top-view and i,k) side-view of two symmetrically independent ligands, l) tetrahedral window with ligand of secondary net in red, m) top-view, n) side-view. o-u) DUT-151*int-cp*, o,q) top-view and p,r) side-view of two symmetrically independent ligands, s) tetrahedral window with ligand of secondary net in red, t) top-view, u) side-view.

The symmetrically independent ligands in DUT-151*int-act* and especially in DUT-151*int-cp* are found to be deformed similar to the ligands in DUT-49*cp* although less severe. It can also be observed that the

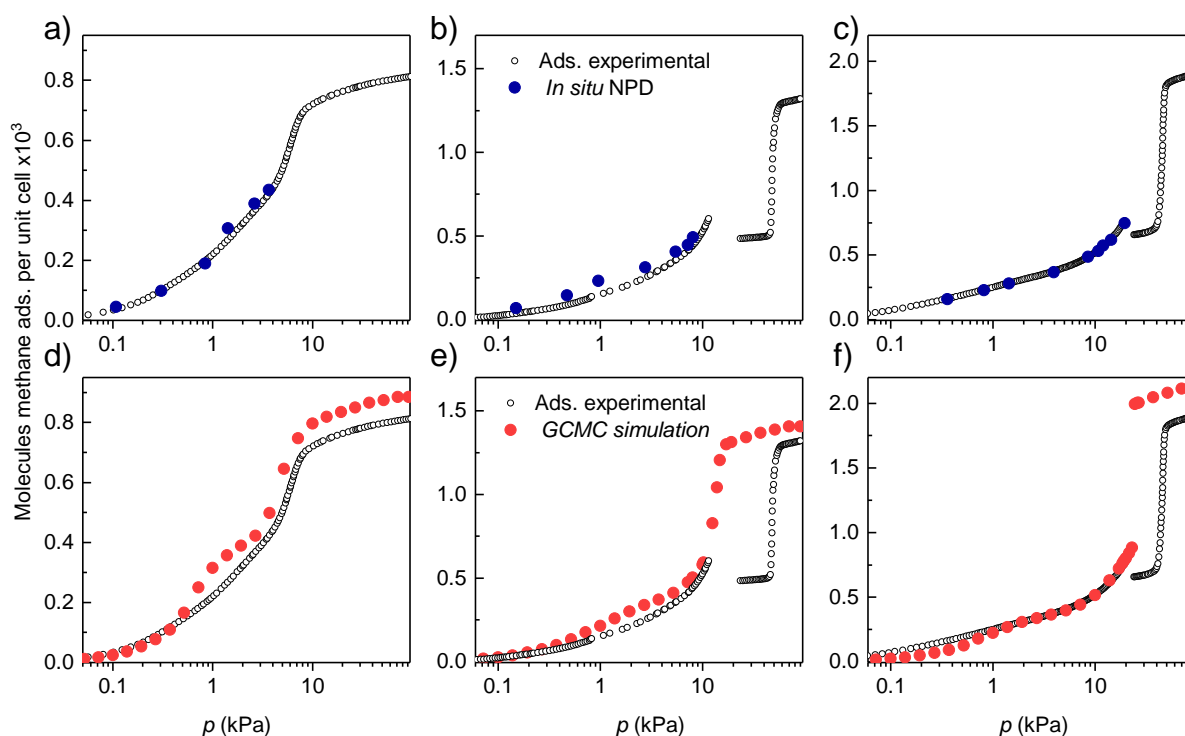
secondary net in DUT-151*int-cp* is oriented differently, mainly due to the deformation of the ligand which results in a shrinkage of the individual nets. This crystallographic information allows to derive a structural mechanism and simulate textural properties such as pore volume and pore size distribution for the different structures in play (Supplementary Figure 74). From the PSD it is obvious that the largest pore diameter in DUT-151*int* is increased from 19 to 22 Å upon activation (DUT-151*int-act*) while maintaining a specific pore volume of 1.09 cm³ g⁻¹. The increase in pore diameter can be explained by interframework dynamics in which the interframework distance is reduced due to dispersive interactions. In contrast, the difference in pore volume between DUT-151*int-op* and *-cp* is 0.32 cm³ g⁻¹, less than 20 % compared with DUT-49 and 50 and in the range of the simulated transitions of DUT-48. Thus, the absence of NGA can be explained by the lack of difference in adsorption energetics and large activation barriers previously derived for DUT-48. The crystallographic analysis can also be set in context to the free energy profiles simulated for DUT-151*int* (Figure 2). A flat slope in the region of 175,000 Å³ indicates the presence of slightly stabilized structures in this range of this unit cell volume. This value is in line with the experimentally observed unit cell volume of DUT-151*int-cp* that needs to be doubled to compare the experimentally obtained structures to the proposed models yielding a unit cell volume of 174,838 Å³. The absence of NGA under any of the various adsorption conditions indicates that the structural contraction in DUT-151*int* lacks the metastable character well reflected by the free energy profile and absence of ligand buckling. Upon contraction, a certain degree of interframework dynamics and bending of the ligands occurs in DUT-151*int*. However, no tilting or concerted rotation of the MOPs is observed - in strong contrast to contraction transitions in DUT-49. The lower degree of ligand deformation and lower extent of reduction in pore volume are the reason for the absence of NGA, however they also enable the reversibility of the transition. Although the structural transition upon adsorption of *n*-butane in DUT-151*int* is well investigated, isotherms recorded using methane and argon show multiple steps and hysteresis that suggest a more complex structural transition compared to the observations made upon adsorption of *n*-butane. The observed structural flexibility in DUT-151*int* presents a unique example of both ligand deformation and interframework dynamics. In conclusion interpenetration suppresses contraction and NGA.

3.8 *In situ*-neutron powder diffraction investigations

3.8.1 *Experimental Details*

In situ NPD experiments were conducted at neutron powder diffractometer E9-FIREPOD at the BER II neutron source of the Helmholtz Zentrum Berlin³⁵ using incoming neutrons with wavelength $\lambda = 2.8172(2)$ Å. A cylindrically-shaped aluminium sample holder with inner diameter of 1 cm and length of 12 cm was filled and sealed under argon atmosphere with 130, 115, and 95 mg of DUT-48, -49, -50, respectively. The sample holder was connected to a gas handling system via a stainless-steel capillary that allowed controlled dosing of methane in the pressure range of 0.001 – 200 kPa with a home-made apparatus. The sample was cooled by a closed cycle helium cryostat system and the temperature was

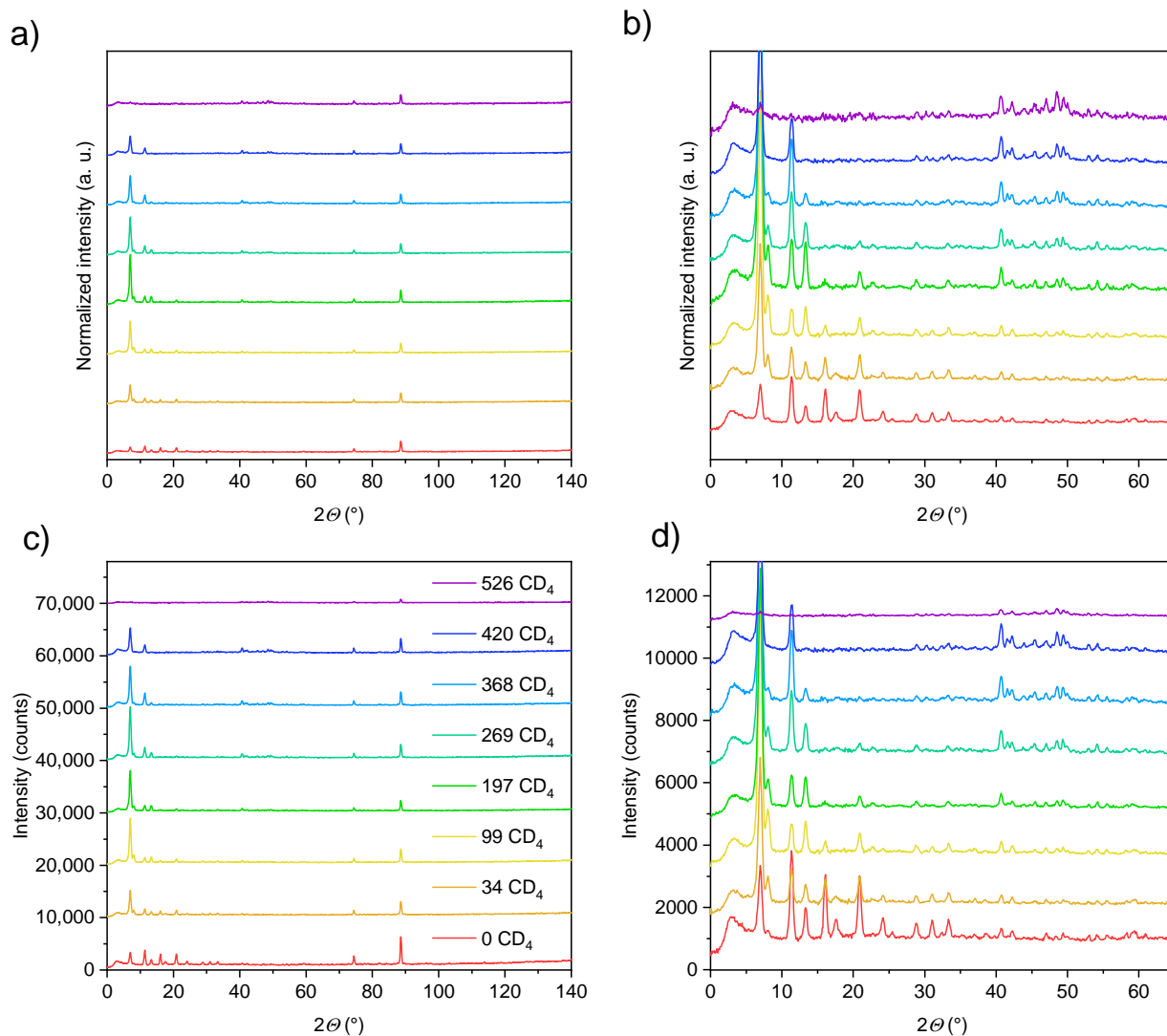
monitored directly at the sample cell with a Lakeshore temperature controller with accuracy of 0.1 K. Prior to the NPD measurement the samples were outgassed in dynamic vacuum (< 0.1 Pa) at 298 K for at least 1 h. Afterwards the samples were cooled to 111 K and diffractograms of the guest-free evacuated MOFs were recorded. Based on the CH_4 isotherms at 111 K, pressures were selected to achieve different loadings of CD_4 . Selected loadings/pressures are displayed in Supplementary Figure 32.



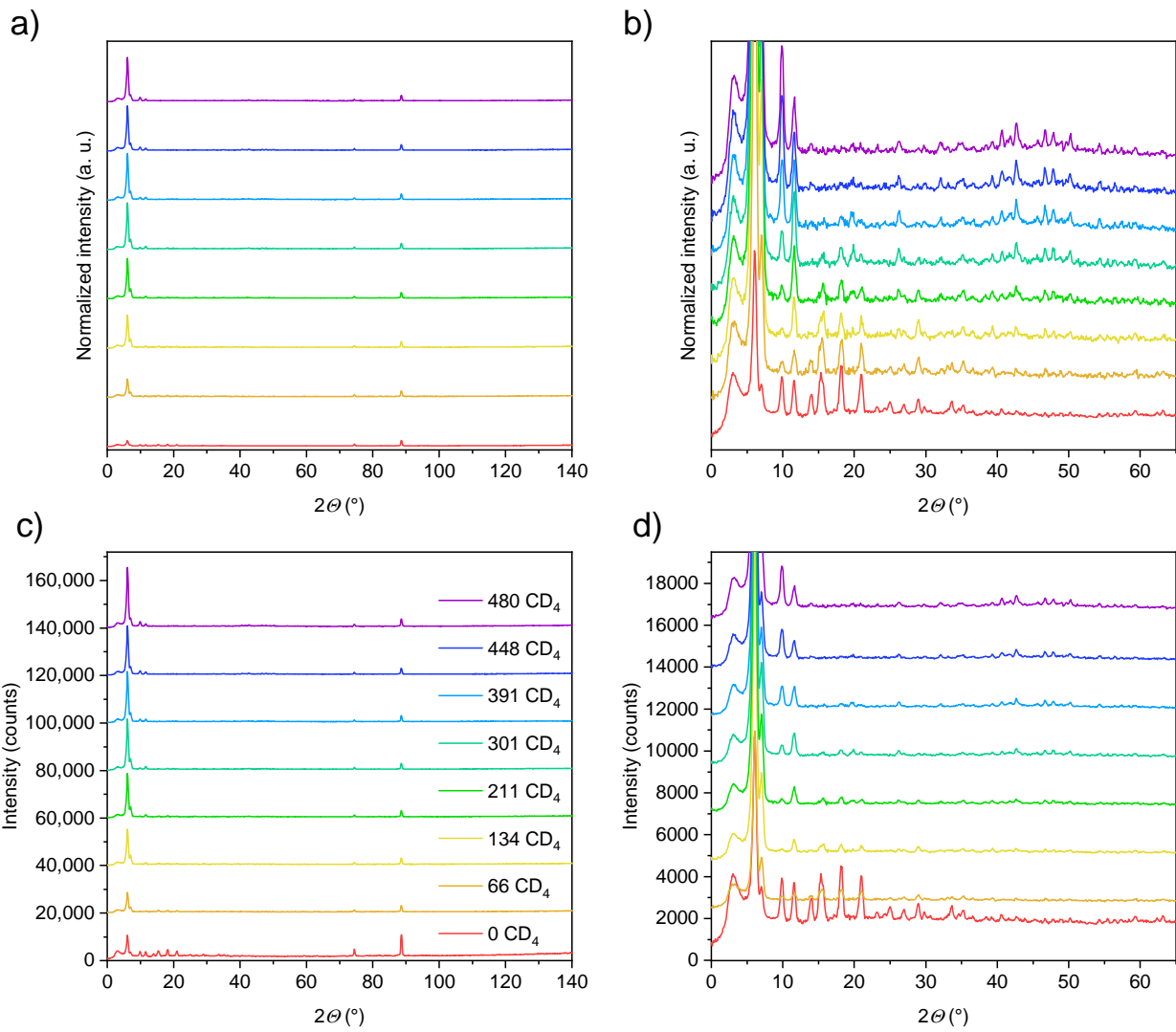
Supplementary Figure 32. Experimental volumetric methane adsorption isotherms at 111 K (open symbols) in comparison to a-c) loadings investigated by NPD (blue) and d-f) GCMC simulations (red) of a,d) DUT-48, b,e) DUT-49 c,f) DUT-50.

Due to the high porosity and large sample amount CD_4 was dosed stepwise to reach the desired loadings without the need of removing CD_4 via evacuation in the case of overdosing. The adsorbed amount of the sample was monitored in parallel by the gas dosing system and showed good agreement with the *ex situ* CH_4 isotherms. Higher loadings required multiple dosing steps and an accurate determination of the loading by the connected gas dosing system was not possible. The loadings of CD_4 were thus determined on the basis of the *ex situ* isotherms and loadings monitored during the *in situ* experiment. Before recording NPD patterns of CD_4 -loaded MOFs, the samples were equilibrated for at least 20 min until the change in pressure was below 1% over 5 min. NPD patterns were recorded in 4-9 scans with 1 - 2.5 h per scan. The detector signals were integrated and calibrated by the in-house Bean software. The final patterns of each loading were obtained by adding the individual scans to obtain good statistics. The obtained patterns for each scan were compared and only summarized to a single pattern if they were identical. For each final pattern, the measuring time and number of scans was selected until the intensity of the main reflection showed at least 10000 counts. Patterns of the evacuated samples with poor scattering were only measured up to 5000 counts. The Al-sample holder shows two reflections at 75° and

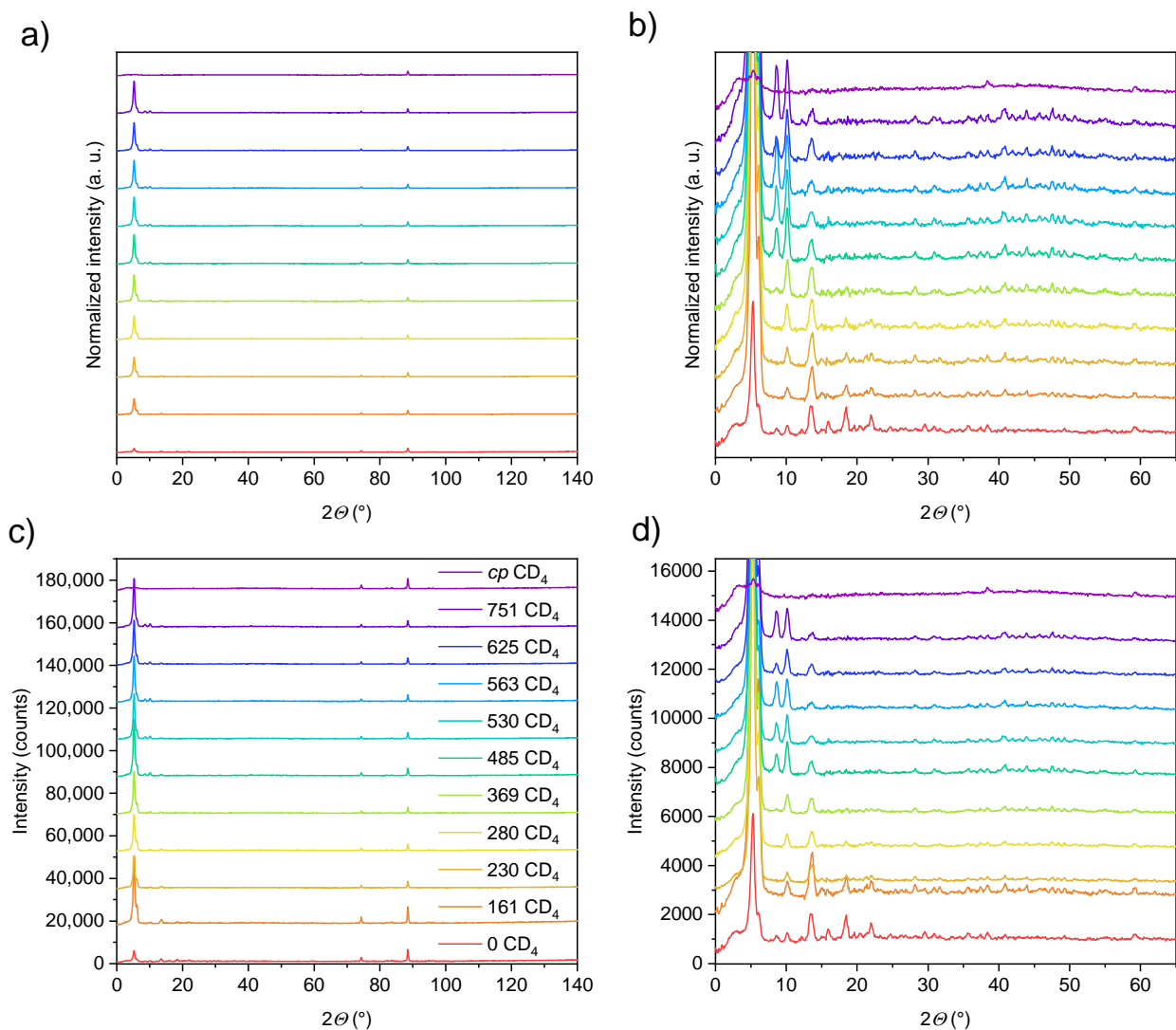
89 ° which were used as an internal standard to normalize the patterns and monitor the increase of intensity of the main reflections in the range of 4 - 20°. These two peaks of the sample holder were omitted from the Rietveld refinement but are shown for clarity in the difference Rietveld plots.



Supplementary Figure 33. NPD patterns for varying loadings with CD₄ in DUT-48: a) normalized NPD patterns with b) magnification of small angle area. c) NPD in absolute scale, and d) magnification of small angle area.



Supplementary Figure 34. NPD patterns for varying loadings with CD₄ in DUT-49: a) normalized NPD patterns with b) magnification of small angle area. c) NPD in absolute scale, and d) magnification of small angle area.



Supplementary Figure 35. NPD patterns for varying loadings with CD₄ in DUT-50: a) normalized NPD patterns with b) magnification of small angle area. c) NPD in absolute scale, and d) magnification of small angle area.

3.8.2 Rietveld refinement of NPD Data

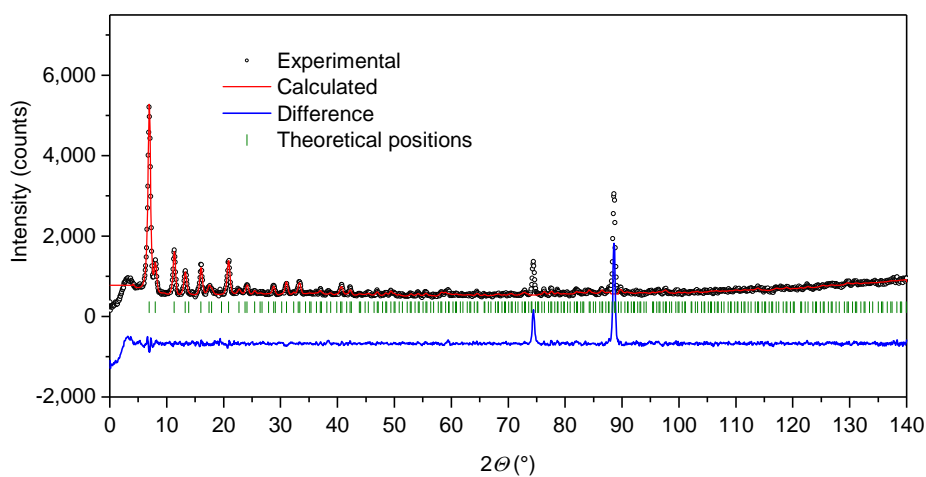
The obtained patterns for DUT-48, 49 and 50 are summarized in Supplementary Figure 33 and were analyzed using FullProf³⁶. Positions and distribution of CD₄ molecules within the unit cell of DUT-48, -49, and -50 were identified using Rietveld refinement in analogy to a recent study on CD₄ adsorption in HKUST-1³⁷. The guest free single crystal structures of DUT-48, -49, and -50 described in Supplementary Table 4 were used as a structural template of the refinement. The oxygen atoms which belong to solvent or water molecules coordinated to the copper paddle-wheels were removed as they are not present in the fully activated MOF. The pseudo-Voigt function with axial divergence (implemented function 12 of FullProf) was used for profile description. Lattice parameters are refined with fixed atom positions of the framework. CD₄ molecules are treated as rigid groups with tetrahedral shape with C-D bond length of 0.999 Å³⁷. For the refinement of CD₄ positions, the experimentally obtained amount of adsorbed CD₄ was introduced at random positions in the unit cell. Within the refinement, the positions of the CD₄ molecules

were refined first. In a second step restriction of translation and rotation of CD₄ were applied to the methane molecules with fixed fractional occupancy of the refined positions. After validating these refinements of the positions further refinement of the fractional occupancy was performed with a fixed scale factor.³⁷ Occupancies of C and D atoms in the CD₄ molecules were assumed to be identical. For each obtained NPD pattern, several refinements were performed starting with slight variations of loading and positions of CD₄. The final refinements of fractional coordinates and occupancies for both, the host lattice and adsorbed CD₄ molecules including background and profile coefficients yielded good agreement with the experimental data. The Rietveld plots, reliability factors, refined amount of loading, fractional coordinates of framework and CD₄ molecules, and lattice parameters are summarized in Supplementary Figure 36 -Supplementary Figure 41, Supplementary Table 16, Supplementary Table 19 (DUT-48), Supplementary Figure 42, Supplementary Figure 48, Supplementary Table 20, Supplementary Table 23 (DUT-49), Supplementary Figure 49, Supplementary Figure 57, Supplementary Table 24, Supplementary Table 27 (DUT-50). Crystallographic files for the refined structures are attached.

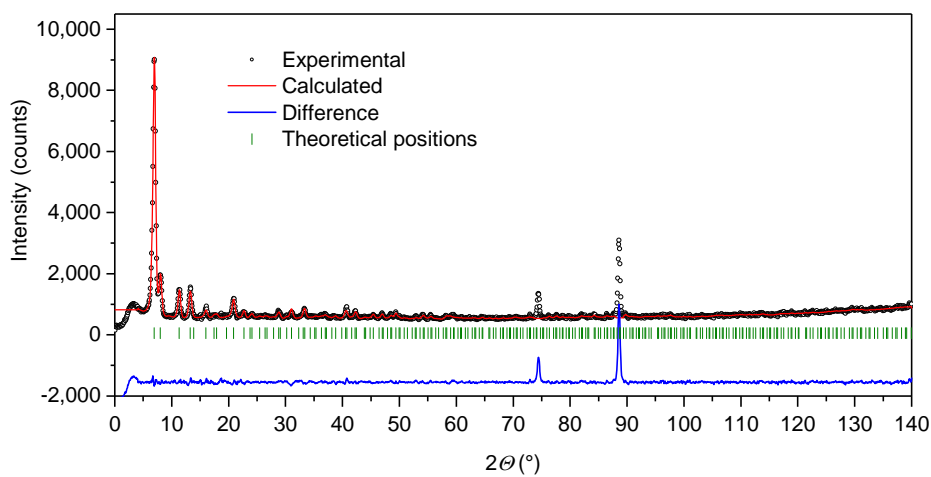
An intrinsic problem of the performed experiments and refinements is the decreased scattering density caused by the high mobility of methane molecules within the pores. Especially at lower loadings CD₄ is more dispersed and exhibits little interactions with other methane molecules, hence occupancies of methane at the pore walls were found below 0.4. Thus, the positions refined only reflect preferential adsorption sites but the methane molecule is not immobilized at this position of the host framework. To reduce the delocalization of methane within the pores, *in situ* NPD experiments with CD₄ adsorption in MOFs are typically performed at low temperature (77 - 4 K)³⁷⁻³⁹ to fix the methane molecules within the pores. Ideally, this will cause immobilization of methane within the pores reflected by refinements of CD₄ positions with high occupancy up to 1 even at lower loadings. However, experiments performed on methane adsorption in ZIF-8 and MOF-5 in the range of 80-3.5 K³⁹ demonstrate, that a phase transition of the fluid at around 60 K occurs. At higher temperatures the adsorption process is found to be different from the adsorption sites at lower temperature. This temperature dependency of the adsorption process was further supported by computational analysis in MOF-5⁴⁰. Consequently, experiments at lower adsorption temperature might yield better refinement of adsorption sites but do not necessarily reflect adsorption sites and mechanism relevant for NGA at intermediate temperatures. The goal of this study was to investigate the adsorption behaviour at 111 K where NGA occurs and thus application of a lower temperature, although fundamentally interesting, would not reflect the conditions of interest for this study. Although this rather high temperature limits the localization of methane adsorption sites, the changes in diffraction intensities show that CD₄ is partly immobilized within the framework especially at higher loadings and consequently gives insights into the adsorption mechanism. Validation of these experimental results by GCMC simulations further supports the findings. Conditions of other *in situ* crystallographic experiments performed in parallel to adsorption of gases on various MOF materials are summarized in an article by Brammer and co-workers⁴¹ and help to set the experiments described in this study in context.

For each refinement of DUT-48, the Rietveld plots are summarized in Supplementary Figure 36 - Supplementary Figure 41, and R-values, refined amount of loading, fractional coordinates of framework and CD₄ molecules, and lattice parameters are summarized in the following.

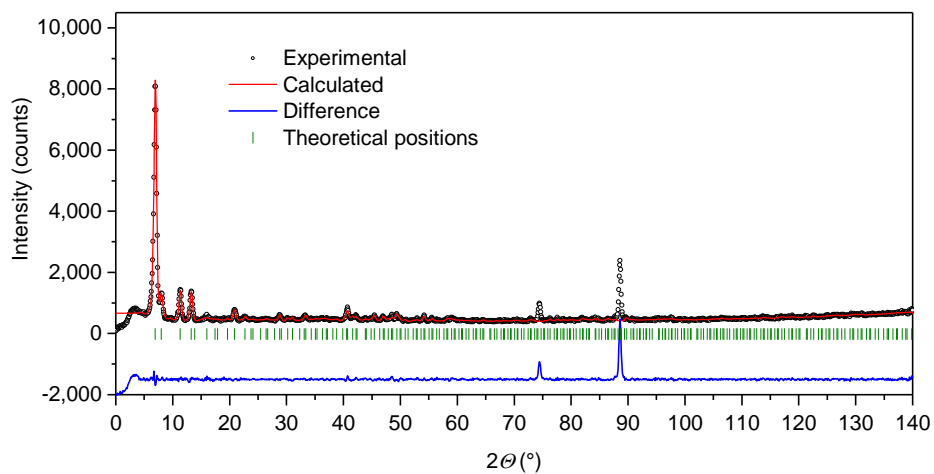
3.8.2.1 Rietveld refinement of CD₄-loaded DUT-48



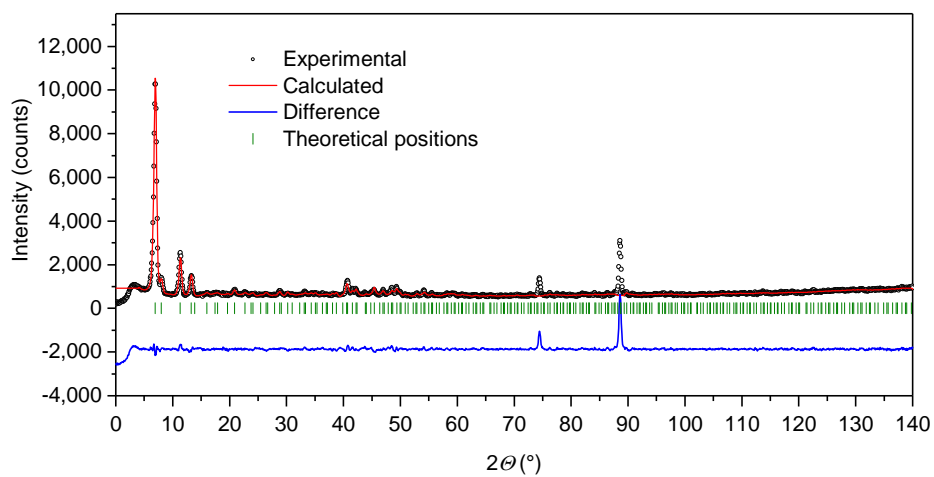
Supplementary Figure 36. Rietveld plot of DUT-48 with a loading of 45 CD₄ molecules per unit cell at 111 K.



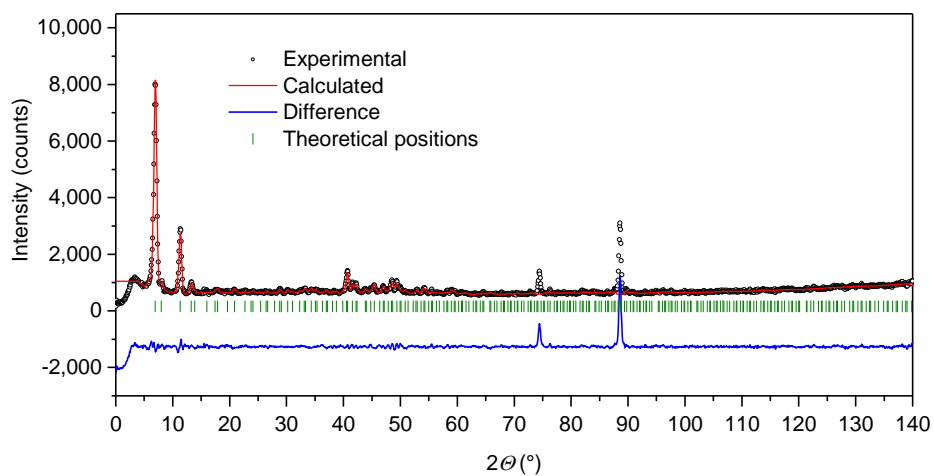
Supplementary Figure 37. Rietveld plot of DUT-48 with a loading of 99 CD₄ molecules per unit cell at 111 K.



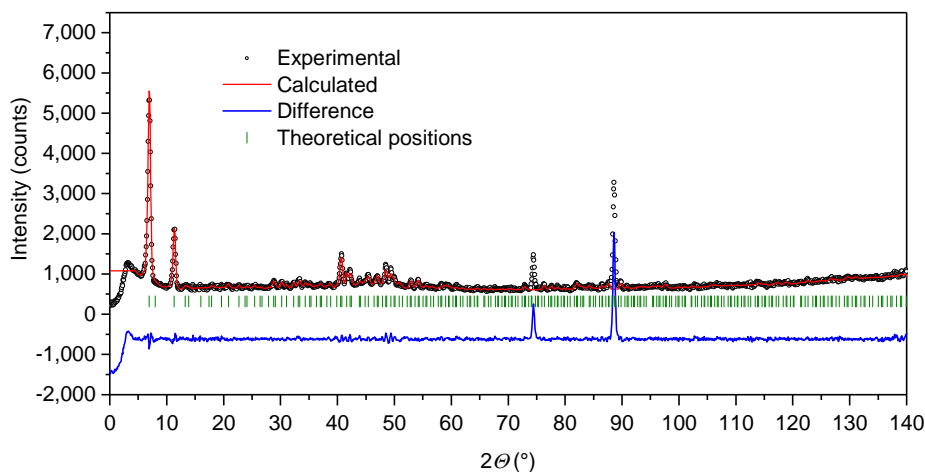
Supplementary Figure 38. Rietveld plot of DUT-48 with a loading of 189 CD₄ molecules per unit cell at 111 K.



Supplementary Figure 39. Rietveld plot of DUT-48 with a loading of 306 CD₄ molecules per unit cell at 111 K.



Supplementary Figure 40. Rietveld plot of DUT-48 with a loading of 389 CD₄ molecules per unit cell at 111 K.



Supplementary Figure 41. Rietveld plot of DUT-48 with a loading of 435 CD₄ molecules per unit cell at 111 K.

Supplementary Table 16. Crystallographic information for DUT-48.

Material ID	DUT-48
Chemical formula, weight	Cu ₂ O ₈ C ₃₄ H ₁₆ N ₂ , 707.6 g mol ⁻¹
Empirical formula, weight	Cu ₄₈ O ₁₉₂ C ₉₆₀ H ₄₈₀ N ₄₈ , 16982.4 g mol ⁻¹
Temperature	111 K
Wavelength	Neutrons; 2.8172(2) Å
Measurement system	E9-FIREPOD at the BER II neutron source, Helmholtz Zentrum Berlin
Crystal system	Cubic
Space group	<i>Fm</i> $\bar{3}$ <i>m</i> (No. 225)
Unit cell dimensions	40.4365(15) Å
Volume	66118(4) Å ³
<i>Z</i>	24
Density	0.426 g cm ⁻³
2 θ range for data collection	-9.40873 ° – 141.79128 °
2 θ resolution	0.075 °
No. of data points	2017
Refinement method, program	Rietveld L.S. refinement, Full Prof

Supplementary Table 17. Lattice and profile parameters for Rietveld refinements of CD₄ loaded DUT-48.

Suppl. Figure	a (Å)	R_p	R_{wp}	R_{exp}	χ^2	R -Bragg	CD ₄ per UC exp.	CD ₄ per UC refined
Supplementary Figure 36	40.435(2)	3.29	4.20	3.80	1.22	4.88	34	45
Supplementary Figure 37	40.436(3)	3.32	4.35	3.72	1.37	4.17	99	99
Supplementary Figure 38	40.446(2)	3.40	4.38	4.20	1.09	4.19	197	189
Supplementary Figure 39	40.453(3)	3.68	4.80	3.59	1.79	4.20	269	306
Supplementary Figure 40	40.450(2)	3.57	4.65	3.55	1.71	4.77	368	389
Supplementary Figure 41	40.4365(16)	3.03	3.81	3.52	1.18	6.97	420	435
No refinement possible due to low diffraction intensities							526	n.a.

Supplementary Table 18. Fractional coordinates of asymmetric unit in guest free DUT-48.

Atom-ID	Atom	Coordinates			U_{iso}	Occupancy
		x	y	z		
CuA	Cu	0.00000	0.00000	0.17184	0.01299	1.00000
CuB	Cu	0.00000	0.00000	0.23683	0.01299	1.00000
OA	O	0.00000	0.04849	0.17676	0.01316	1.00000
OB	O	0.00000	0.04828	0.23210	0.01316	1.00000
NA	N	0.00000	0.20092	0.20092	0.01316	1.00000
CA	C	0.00000	0.06252	0.20440	0.01408	1.00000
CB	C	0.00000	0.09904	0.20453	0.01408	1.00000
CC	C	0.00000	0.11628	0.23485	0.01408	1.00000
HCA	H	0.00000	0.10430	0.25440	0.04711	1.00000
CD	C	0.00000	0.15016	0.23632	0.01408	1.00000
HDA	H	0.00000	0.16120	0.25640	0.04711	1.00000
CE	C	0.00000	0.16728	0.20660	0.01408	1.00000
CF	C	0.00000	0.15079	0.17610	0.01408	1.00000
CG	C	0.00000	0.11657	0.17520	0.01408	1.00000
HGA	H	0.00000	0.10550	0.15510	0.04711	1.00000
CH	C	0.00000	0.22608	0.22608	0.01408	1.00000
CI	C	0.02412	0.24912	0.22658	0.01408	0.50000
HIA	H	0.04070	0.24870	0.21070	0.04713	0.50000
HIA	H	0.04070	0.24870	0.21070	0.04713	0.50000

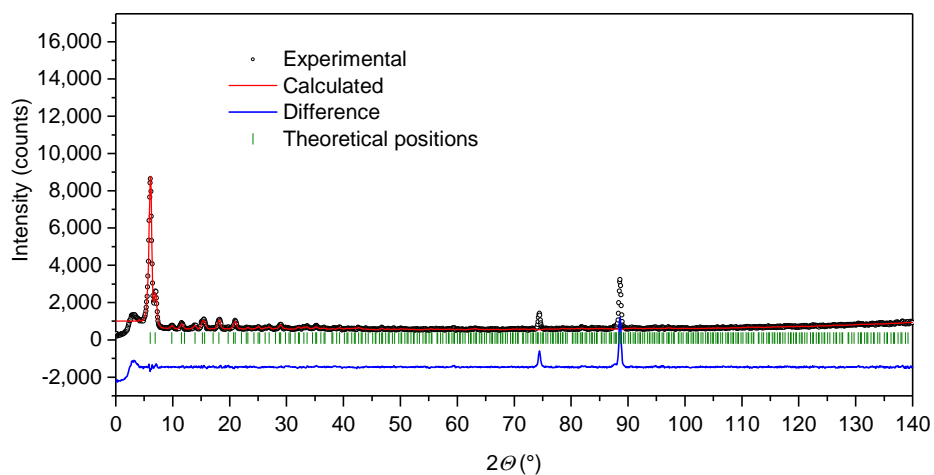
Supplementary Table 19. Fractional coordinates of CD₄ molecules in DUT-48 at varied loadings.

CD ₄ per UC	Atom-ID	Atom	<i>X</i>	<i>y</i>	<i>z</i>	<i>U</i> _{iso}	Occupancy
45	AD1	C	0.00000	0.04235	0.09175	0.01408	0.1821(4)
45	BD1	C	0.09237	0.09237	0.15638	0.01408	0.2841(6)
99	AD1	C	0.00000	0.04665	0.08156	0.01408	0.255(7)
99	BD1	C	0.08911	0.08911	0.16049	0.01408	0.773(14)
189	AD1	C	0.08792	0.08792	0.15818	0.01408	0.85(2)
189	BD1	C	0.09444	0.09444	0.24697	0.01408	0.50(2)
189	CD1	C	0.07189	0.07189	0.00000	0.01408	0.644(17)
189	DD1	C	0.17883	0.17883	0.08643	0.01408	0.30(2)
306	AD1	C	0.09571	0.09571	0.16643	0.01408	1.00000
306	BD1	C	0.07523	0.07523	0.26657	0.01408	1.00000
306	CD1	C	0.07822	0.07822	0.00000	0.01408	1.00000
306	DD1	C	0.20002	0.20002	0.09155	0.01408	0.69(2)
389	AD1	C	0.09354	0.09354	0.17899	0.01408	0.721(20)
389	BD1	C	0.08081	0.08081	0.26427	0.01408	0.65(2)
389	CD1	C	0.10955	0.32467	0.21599	0.01408	0.338(13)
389	DD1	C	0.17104	0.17104	0.53480	0.01408	0.596(20)
389	ED1	C	0.19243	0.19243	0.10024	0.01408	0.91(2)
389	FD1	C	0.08635	0.08635	0.00000	0.01408	1.000(12)
435	AD1	C	0.09117	0.09117	0.16207	0.01408	0.87(3)
435	BD1	C	0.07462	0.07462	0.30334	0.01408	0.57(4)
435	CD1	C	0.21012	0.21011	0.40755	0.01408	0.57(3)
435	DD1	C	0.16780	0.16780	0.46469	0.01408	0.48(3)
435	ED1	C	0.19111	0.19111	0.10157	0.01408	0.91(3)

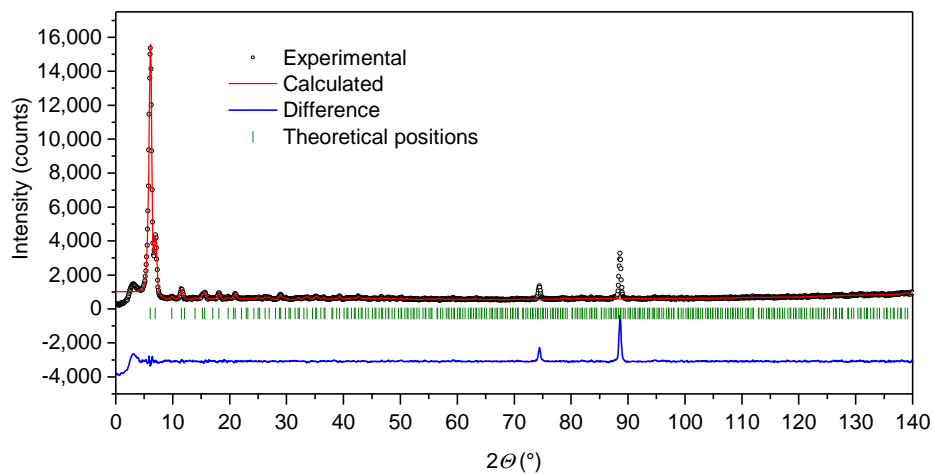
Recently, Rowland *et al.* presented *in situ* NPD analysis of CD₄ adsorption in PCN-81³ previously demonstrated as isostructural to DUT-48. In their work the authors used the synthesis and activation procedure described by Zhou and co-workers⁴. The NPD experiments were performed at 7 K and the lower *Pa* $\bar{3}$ symmetry refined for PCN-81 was used for Rietveld refinement of the obtained NPD pattern to obtain primary adsorption sites of methane within the porous structure of PCN-81. Loadings of 48, 92, 192 CD₄ molecules per unit cell were analysed only covering the low-pressure region of the adsorption isotherm. Their report supports the findings of the present study on DUT-48 in which only open metal sites and the cub voids are filled with methane at these low loadings.

3.8.2.2 Rietveld refinement of CD₄-loaded DUT-49

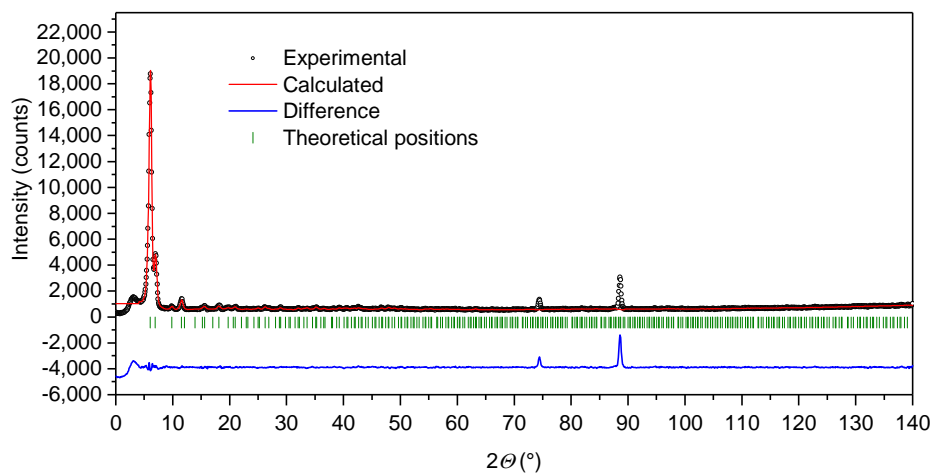
For each refinement of DUT-49, the Rietveld plots are summarized in Supplementary Figure 42- Supplementary Figure 48, and R-values, refined amount of loading, fractional coordinates of framework and CD₄ molecules, and lattice parameters are summarized in the following.



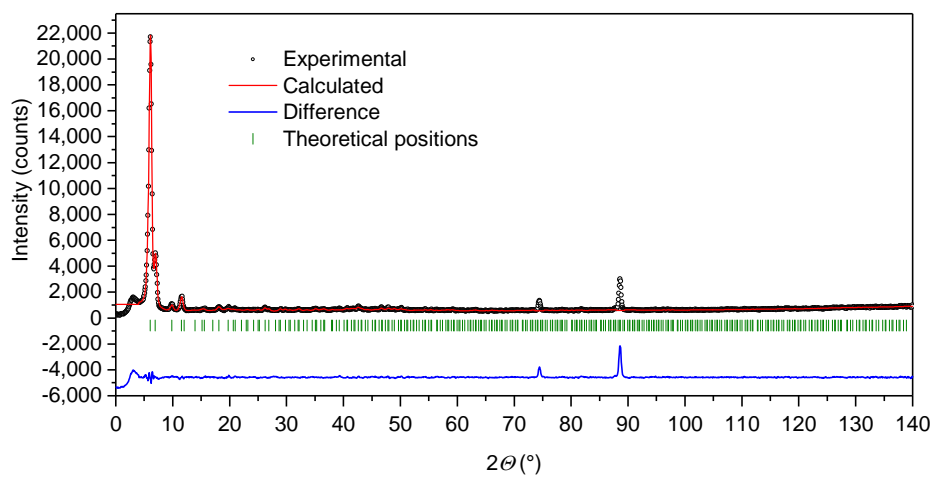
Supplementary Figure 42. Rietveld plot of DUT-49 with a loading of 68 CD₄ molecules per unit cell at 111 K.



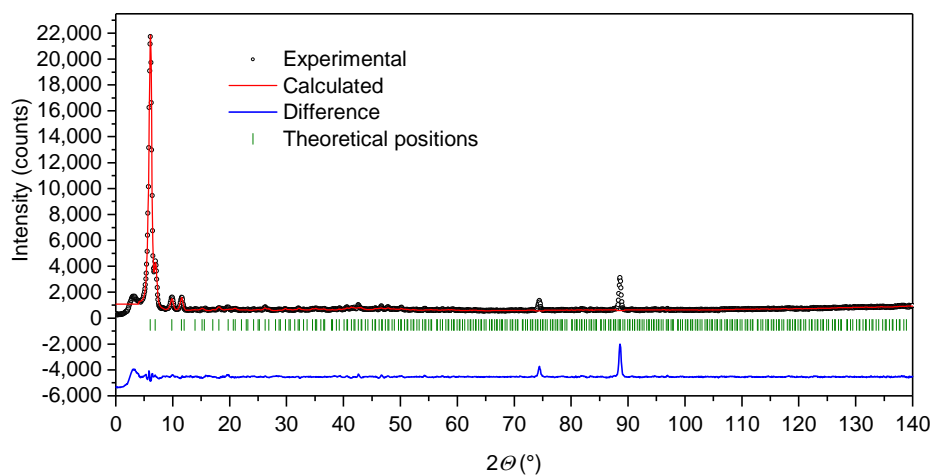
Supplementary Figure 43. Rietveld plot of DUT-49 with a loading of 145.5 CD₄ molecules per unit cell at 111 K.



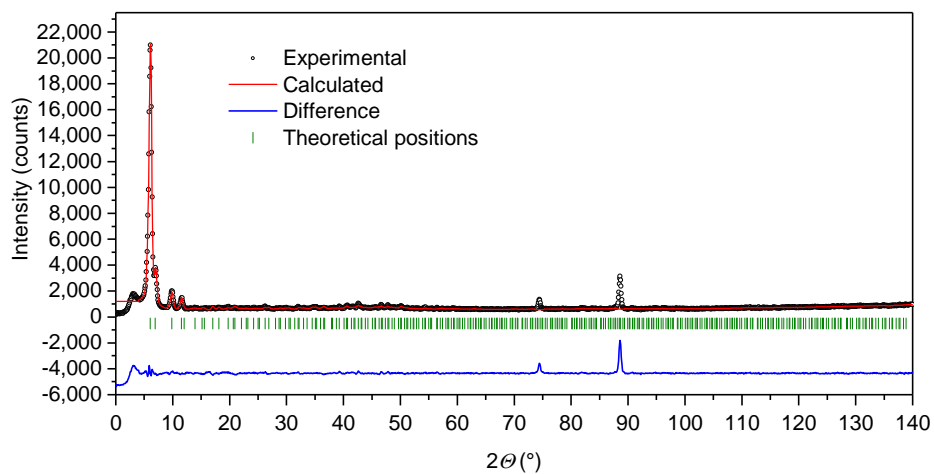
Supplementary Figure 44. Rietveld plot of DUT-49 with a loading of 231 CD₄ molecules per unit cell at 111 K.



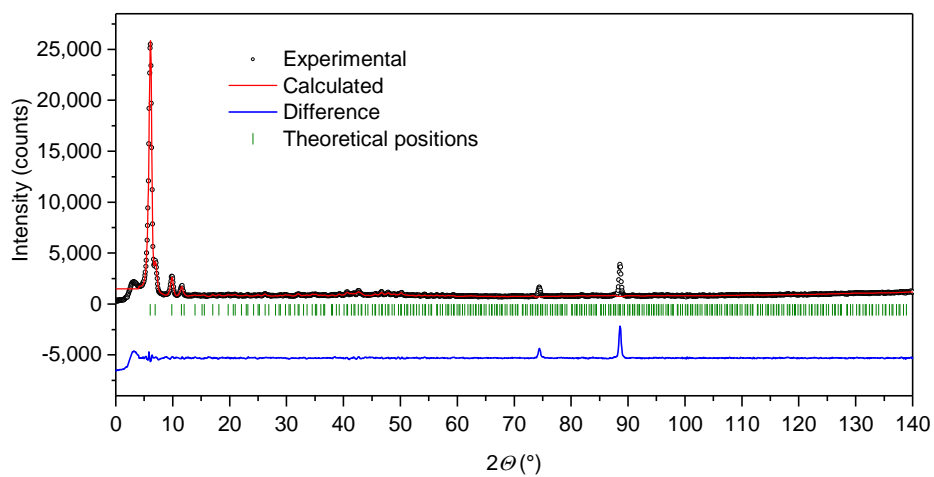
Supplementary Figure 45. Rietveld plot of DUT-49 with a loading of 311 CD₄ molecules per unit cell at 111 K.



Supplementary Figure 46. Rietveld plot of DUT-49 with a loading of 405 CD₄ molecules per unit cell at 111 K.



Supplementary Figure 47. Rietveld plot of DUT-49 with a loading of 446.5 CD₄ molecules per unit cell at 111 K.



Supplementary Figure 48. Rietveld plot of DUT-49 with a loading of 492 CD₄ molecules per unit cell at 111 K.

Supplementary Table 20. Crystallographic information for DUT-49.

Material ID	DUT-49
Chemical formula, weight	$\text{Cu}_2\text{O}_8\text{C}_{40}\text{H}_{20}\text{N}_2$, 783.7 g mol ⁻¹
Empirical formula, weight	$\text{Cu}_{48}\text{O}_{192}\text{C}_{960}\text{H}_{480}\text{N}_{48}$, 18808.8 g mol ⁻¹
Temperature	111 K
Wavelength	Neutrons; 2.8172(2) Å
Measurement system	E9-FIREPOD at the BER II neutron source, Helmholtz Zentrum Berlin
Crystal system	Cubic
Space group	$Fm\bar{3}m$ (No. 225)
Unit cell dimensions	46.391(7) Å
Volume	99836(26) Å ³
Z	24
Density	0.312821 g cm ⁻³
2 θ range for data collection	-9.40873 ° – 141.79128 °
2 θ resolution	0.075 °
No. of data points	2017
Refinement method, program	Rietveld L.S. refinement, Full Prof

Supplementary Table 21. Lattice and profile parameters for Rietveld refinements of CD₄ loaded DUT-49.

Suppl. Figure	a (Å)	R_p	R_{wp}	R_{exp}	χ^2	R-Bragg	CD ₄ per UC exp.	CD ₄ per UC refin.
Supplementary Figure 42	46.425(4)	2.91	3.71	3.71	1.00	5.38	66	68
Supplementary Figure 43	46.436(4)	3.02	3.95	3.60	1.20	2.84	134	145.5
Supplementary Figure 44	46.447(5)	3.12	4.07	3.54	1.32	2.98	211	231
Supplementary Figure 45	46.473(5)	3.22	4.30	3.48	1.53	3.23	301	311
Supplementary Figure 46	46.469(4)	3.42	4.65	3.45	1.82	3.33	391	405
Supplementary Figure 47	46.477(5)	3.39	4.56	3.42	1.77	4.19	448	446.5
Supplementary Figure 48	46.472(4)	2.82	3.75	3.05	1.51	2.61	480	492

Supplementary Table 22. Fractional coordinates of asymmetric unit in guest free DUT-49.

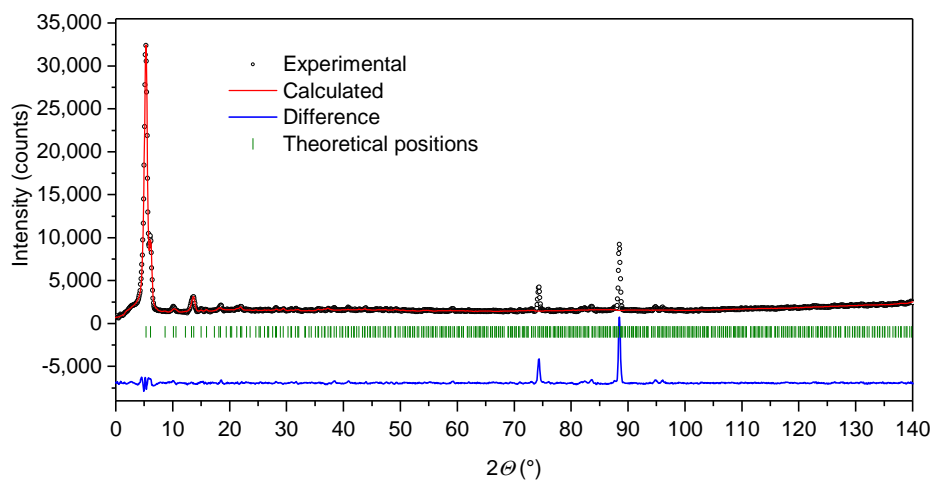
Atom-ID	Atom	Coordinates			U_{iso}	Occupancy
		x	y	z		
CuA	Cu	0.00000	0.00000	0.35040	0.01299	1.00000
CuB	Cu	0.00000	0.00000	0.29560	0.01299	1.00000
OA	O	0.00000	0.04041	0.34750	0.01316	1.00000
OB	O	0.00000	0.04240	0.29930	0.01316	1.00000
CA	C	0.00000	0.05550	0.32360	0.01408	1.00000
CB	C	0.00000	0.08810	0.32440	0.01408	1.00000
CC	C	0.00000	0.10400	0.34990	0.01408	1.00000
HC	H	0.00000	0.09437	0.36818	0.04711	1.00000
CD	C	0.00000	0.13410	0.34850	0.01408	1.00000
CE	C	0.00000	0.14640	0.32100	0.01408	1.00000
CF	C	0.00000	0.13100	0.29500	0.01408	1.00000
HF	H	0.00000	0.14059	0.27663	0.04711	1.00000
CG	C	0.00000	0.10110	0.29720	0.01408	1.00000
HG	H	0.00000	0.08949	0.28016	0.04711	1.00000
NA	N	0.00000	0.17690	0.32310	0.01316	1.00000
CH	C	0.00000	0.19870	0.30130	0.01408	1.00000
CI	C	0.02410	0.21690	0.29970	0.01408	0.50000
HI	H	0.03991	0.21474	0.31282	0.04711	0.50000
CJ	C	0.02410	0.23820	0.27850	0.01408	0.50000
HJ	H	0.04005	0.25122	0.27643	0.04711	0.50000
CK	C	0.00000	0.23980	0.26020	0.01408	1.00000

Supplementary Table 23. Fractional coordinates of CD₄ molecules in DUT-49 at varied loadings.

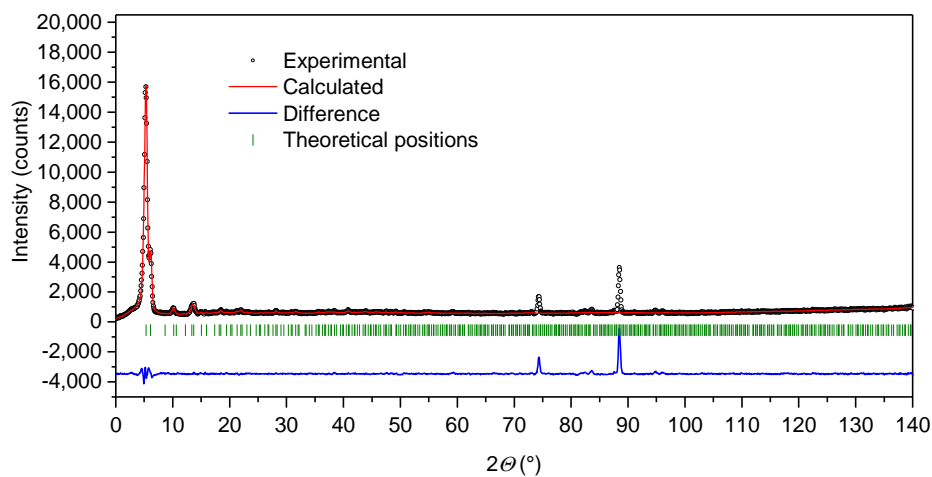
CD ₄ per UC	Atom-ID	Atom	<i>x</i>	<i>y</i>	<i>z</i>	<i>U</i> _{iso}	Occupancy
68	AD1	C	0.02078	0.02078	0.41049	0.01408	0.307(8)
68	BD1	C	0.08155	0.08155	0.34879	0.01408	0.399(14)
145.5	AD1	C	0.02182	0.02182	0.41981	0.01408	0.324(13)
145.5	BD1	C	0.08702	0.08702	0.43858	0.01408	0.2803(9)
145.5	CD1	C	0.07616	0.16468	0.39687	0.01408	0.386(10)
145.5	DD1	C	0.00374	0.00374	0.22505	0.01408	0.1384(5)
231	AD1	C	0.02459	0.02459	0.41011	0.01408	0.522(11)
231	BD1	C	0.11533	0.11533	0.44070	0.01408	0.686(17)
231	CD1	C	0.08399	0.18661	0.37417	0.01408	0.400(12)
231	DD1	C	0.04710	0.04710	0.23536	0.01408	0.396(16)
311	AD1	C	0.04097	0.04097	0.41978	0.01408	0.652(13)
311	BD1	C	0.12171	0.12171	0.43375	0.01408	0.81(2)
311	CD1	C	0.08444	0.19053	0.36756	0.01408	0.397(17)
311	DD1	C	0.06153	0.06153	0.27431	0.01408	0.99(3)
405	AD1	C	0.04447	0.04447	0.40690	0.01408	0.898(16)
405	BD1	C	0.13369	0.13369	0.43118	0.01408	1.000
405	CD1	C	0.06705	0.23219	0.36328	0.01408	0.661(18)
405	DD1	C	0.06492	0.06492	0.27173	0.01408	1.000
446.5	AD1	C	0.02117	0.06317	0.40297	0.01408	0.542(9)
446.5	BD1	C	0.03565	0.14019	0.25011	0.01408	0.687(17)
446.5	CD1	C	0.13325	0.07868	0.33728	0.01408	0.596(16)
446.5	DD1	C	0.07827	0.07827	0.27634	0.01408	1.000
492	AD1	C	0.01530	0.05400	0.40869	0.01408	0.386(7)
492	BD1	C	0.08305	0.08305	0.35000	0.01408	1.000
492	CD1	C	0.07386	0.07386	0.27129	0.01408	1.000
492	DD1	C	0.02622	0.19969	0.13841	0.01408	0.415(15)
492	ED1	C	0.06947	0.16414	0.28080	0.01408	0.572(17)
492	FD1	C	0.12357	0.12357	0.29867	0.01408	0.38(3)

3.8.2.3 Rietveld refinement of CD₄-loaded DUT-50

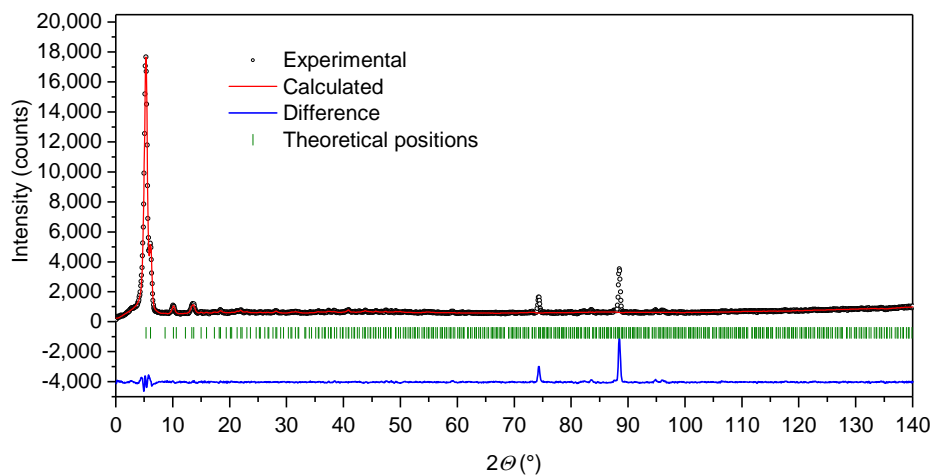
For each refinement of DUT-50, the Rietveld plots are summarized in Supplementary Figure 49- Supplementary Figure 57, and R-values, refined amount of loading, fractional coordinates of framework and CD₄ molecules, and lattice parameters are summarized in the following.



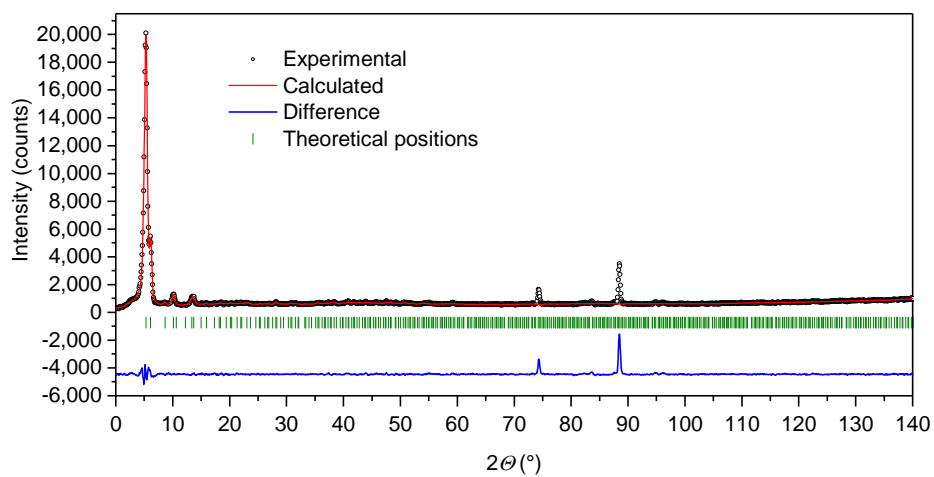
Supplementary Figure 49. Rietveld plot of DUT-50 with a loading of 159 CD₄ molecules per unit cell at 111 K.



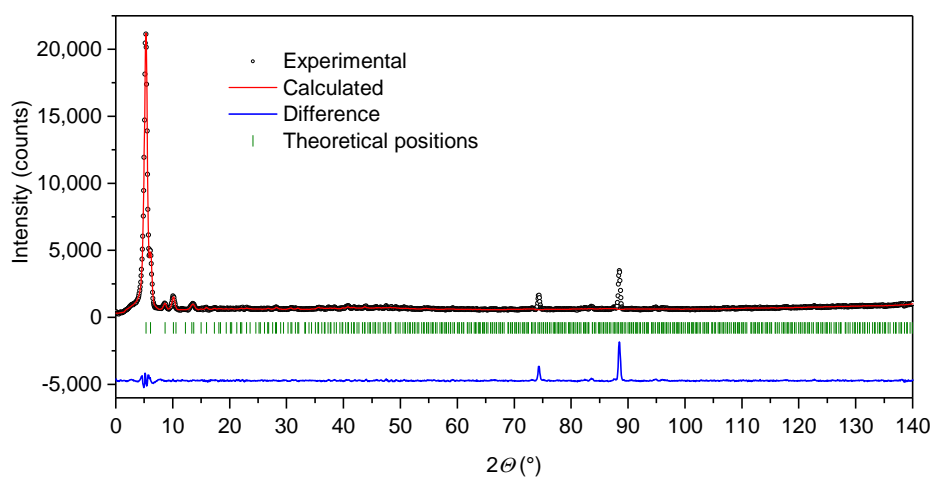
Supplementary Figure 50. Rietveld plot of DUT-50 with a loading of 228.5 CD₄ molecules per unit cell at 111 K.



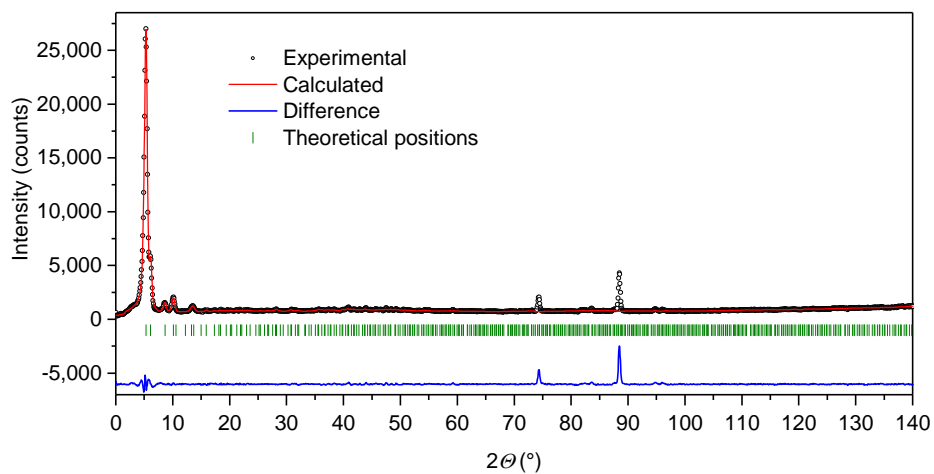
Supplementary Figure 51. Rietveld plot of DUT-50 with a loading of 280 CD₄ molecules per unit cell at 111 K.



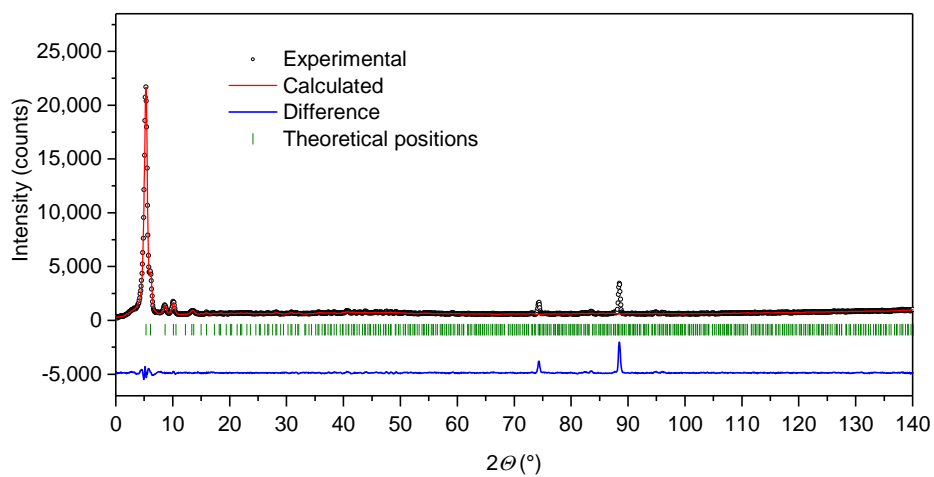
Supplementary Figure 52. Rietveld plot of DUT-50 with a loading of 370 CD₄ molecules per unit cell at 111 K.



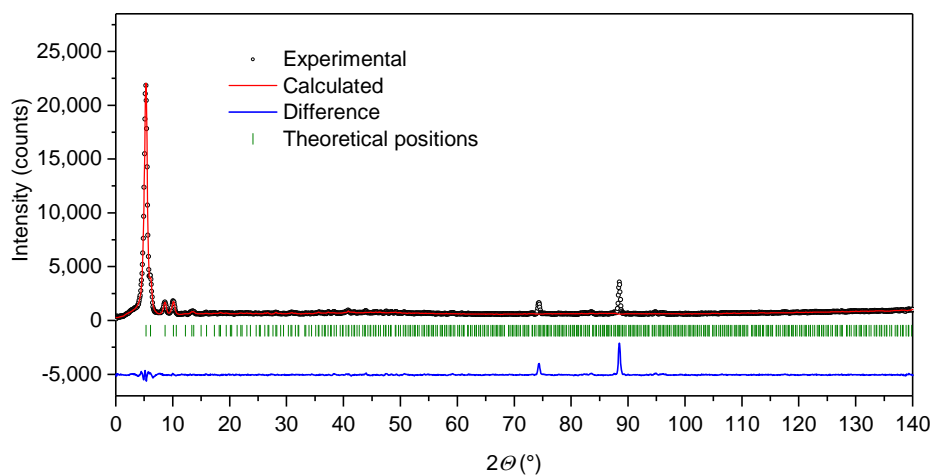
Supplementary Figure 53. Rietveld plot of DUT-50 with a loading of 488 CD₄ molecules per unit cell at 111 K.



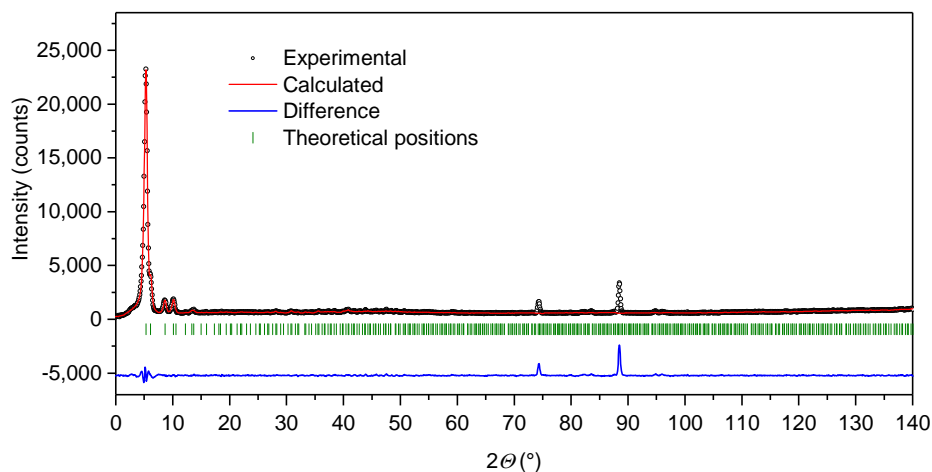
Supplementary Figure 54. Rietveld plot of DUT-50 with a loading of 529 CD₄ molecules per unit cell at 111 K.



Supplementary Figure 55. Rietveld plot of DUT-50 with a loading of 569 CD₄ molecules per unit cell at 111 K.



Supplementary Figure 56. Rietveld plot of DUT-50 with a loading of 683 CD₄ molecules per unit cell at 111 K.



Supplementary Figure 57. Rietveld plot of DUT-50 with a loading of 756 CD₄ molecules per unit cell at 111 K.

Supplementary Table 24. Crystallographic information for DUT-50.

Material ID	DUT-50
Chemical formula, weight	Cu ₂ O ₈ C ₄₆ H ₂₄ N ₂ , 859.7 g mol ⁻¹
Empirical formula, weight	Cu ₄₈ O ₁₉₂ C ₉₆₀ H ₄₈₀ N ₄₈ , 20632.8 g mol ⁻¹
Temperature	111 K
Wavelength	Neutrons; 2.8172(2) Å
Measurement system	E9-FIREPOD at the BER II neutron source, Helmholtz Zentrum Berlin
Crystal system	Cubic
Space group	<i>Fm</i> $\bar{3}$ <i>m</i> (No. 225)
Unit cell dimensions	52.744(6) Å
Volume	146,731(30) Å ³
Z	24
Density	0.234 g cm ⁻³
2 θ range for data collection	-9.40873 ° – 141.79128 °
2 θ resolution	0.075 °
No. of data points	2017
Refinement method, program	Rietveld L.S. refinement, Full Prof

Supplementary Table 25. Lattice and profile parameters for Rietveld refinements of CD₄ loaded DUT-50.

Suppl. Figure	a (Å)	R_p	R_{wp}	R_{exp}	χ^2	R -Bragg	CD ₄ per UC exp.	CD ₄ per UC refined
Supplementary Figure 49	52.852(9)	3.16	4.35	2.29	3.61	4.83	161	159
Supplementary Figure 50	52.852(9)	3.58	4.79	3.58	1.79	3.66	230	228.5
Supplementary Figure 51	52.785(8)	3.57	4.84	3.53	1.88	3.09	280	280
Supplementary Figure 52	52.803(8)	3.71	4.90	3.50	1.96	3.19	369	370
Supplementary Figure 53	52.839(8)	3.51	4.62	3.46	1.78	2.80	485	488
Supplementary Figure 54	52.855(8)	3.42	4.61	3.08	2.24	2.41	530	529
Supplementary Figure 55	52.808(7)	3.68	4.87	3.44	2.01	3.37	563	569
Supplementary Figure 56	52.789(5)	3.46	4.75	3.43	1.92	2.60	625	683
Supplementary Figure 57	52.814(5)	3.62	4.81	3.42	1.97	2.64	751	756

Supplementary Table 26. Fractional coordinates of asymmetric unit in guest-free DUT-50 from NPD data.

Atom-ID	Atom	Coordinates			U_{iso}	Occupancy
		x	y	z		
CuA	Cu	0.00000	0.00000	0.36786	0.01299	1.00000
CuB	Cu	0.00000	0.00000	0.31786	0.01299	1.00000
OA	O	0.00000	0.03667	0.36410	0.01316	1.00000
OB	O	0.00000	0.03640	0.32170	0.01316	1.00000
NA	N	0.00000	0.15413	0.34587	0.01316	1.00000
CA	C	0.00000	0.04761	0.34295	0.01408	1.00000
CB	C	0.00000	0.07581	0.34276	0.01408	1.00000
CC	C	0.00000	0.08978	0.36513	0.01408	1.00000
HC	H	0.00000	0.08142	0.38070	0.04711	1.00000
CD	C	0.00000	0.11591	0.36464	0.01408	1.00000
CE	C	0.00000	0.12848	0.34150	0.01408	1.00000
CF	C	0.00000	0.11548	0.31819	0.01408	1.00000
HF	H	0.00000	0.12408	0.30280	0.04711	1.00000
CG	C	0.00000	0.08972	0.31925	0.01408	1.00000
HG	H	0.00000	0.08069	0.30410	0.04711	1.00000
CH	C	0.00000	0.17419	0.32582	0.01408	1.00000
CI	C	0.01959	0.19147	0.32550	0.01408	0.50000
HI	H	0.03271	0.19067	0.33730	0.04711	0.50000
CJ	C	0.01923	0.21045	0.30646	0.01408	0.50000
HJ	H	0.03198	0.22260	0.30580	0.04711	0.50000
CK	C	0.00000	0.21100	0.28901	0.01408	1.00000
CL	C	0.00000	0.23071	0.26927	0.01408	1.00000
CM	C	0.01898	0.24811	0.26740	0.01408	0.50000
HM	H	0.03229	0.24750	0.27900	0.04711	0.50000

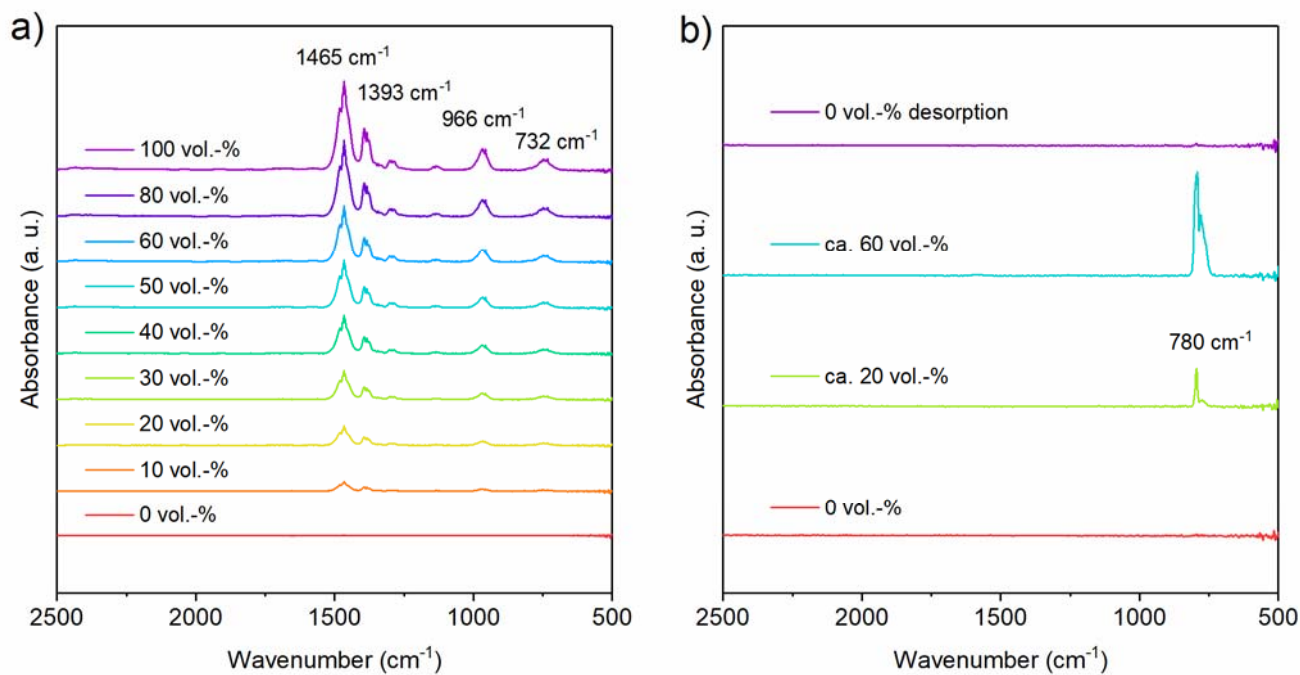
Supplementary Table 27. Fractional coordinates of CD₄ molecules in DUT-50 at varied loadings.

CD ₄ per UC	Atom-ID	Atom	<i>x</i>	<i>Y</i>	<i>z</i>	<i>U</i> _{iso}	Occupancy
159	AD1	C	0.11968	0.11967	0.56437	0.01408	0.96(3)
159	BD1	C	0.07280	0.07280	0.47208	0.01408	0.69(3)
218.5	AD1	C	0.14298	0.14297	0.56304	0.01408	0.57(5)
218.5	BD1	C	0.06427	0.06427	0.47982	0.01408	0.45(2)
218.5	CD1	C	0.04005	0.04005	0.27431	0.01408	0.55(4)
218.5	DD1	C	0.07279	0.07279	0.36556	0.01408	0.81(6)
280	AD1	C	0.14736	0.14735	0.56155	0.01408	0.76(3)
280	BD1	C	0.06517	0.06517	0.50000	0.01408	1.000(16)
280	CD1	C	0.04064	0.04064	0.27612	0.01408	0.66(4)
280	DD1	C	0.07366	0.07366	0.36343	0.01408	1.000(19)
370	AD1	C	0.03285	0.03285	0.39258	0.01408	0.81(2)
370	BD1	C	0.11573	0.11573	0.43472	0.01408	1.000(12)
370	CD1	C	0.12766	0.06434	0.29850	0.01408	0.56(3)
370	DD1	C	0.23252	0.03077	0.42897	0.01408	0.46(2)
488	AD1	C	0.02736	0.06837	0.40339	0.01408	0.592(17)
488	BD1	C	0.12289	0.06805	0.34789	0.01408	0.66(3)
488	CD1	C	0.13594	0.05012	0.27364	0.01408	0.54(7)
488	DD1	C	0.22437	0.04370	0.41114	0.01408	0.75(7)
529	AD1	C	0.02705	0.06656	0.39994	0.01408	0.61(2)
529	BD1	C	0.11927	0.07254	0.34550	0.01408	0.65(4)
529	CD1	C	0.14860	0.04684	0.26776	0.01408	0.67(5)
529	DD1	C	0.22223	0.04669	0.41533	0.01408	0.83(5)
569	AD1	C	0.02565	0.06478	0.39720	0.01408	0.651(20)
569	BD1	C	0.12241	0.07566	0.34224	0.01408	0.67(4)
569	CD1	C	0.14852	0.04426	0.26688	0.01408	0.79(5)
569	DD1	C	0.22133	0.04777	0.41810	0.01408	0.86(5)
683	AD1	C	0.03463	0.03463	0.39225	0.01408	1.00000
683	BD1	C	0.11483	0.11483	0.42957	0.01408	1.00000
683	CD1	C	0.02847	0.18312	0.23351	0.01408	0.5592(12)
683	DD1	C	0.03934	0.03934	0.26322	0.01408	1.0000(12)
683	ED1	C	0.12497	0.12497	0.30003	0.01408	1.0000(12)

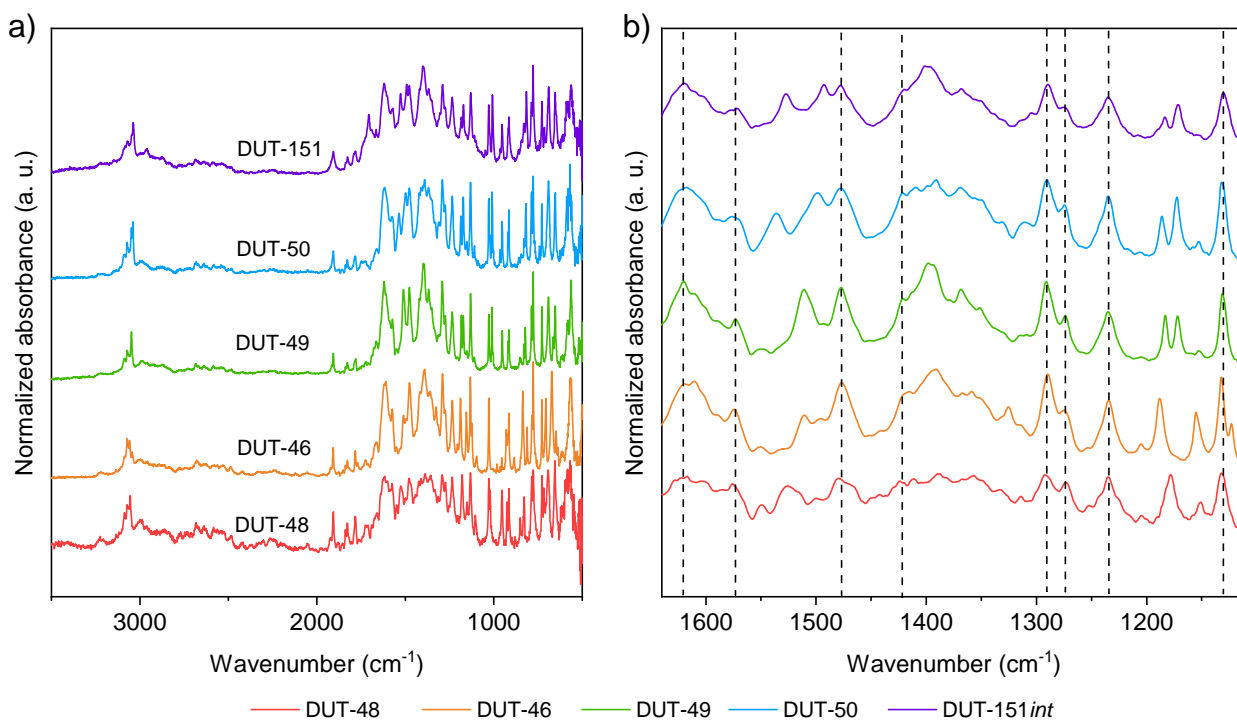
683	FD1	C	0.29528	0.39076	0.45415	0.01408	1.0000(12)
756	AD1	C	0.04137	0.04137	0.39096	0.01408	1.0
756	BD1	C	0.10866	0.10866	0.43153	0.01408	1.0
756	CD1	C	0.04163	0.14674	0.23557	0.01408	0.94(3)
756	DD1	C	0.04855	0.04855	0.25574	0.01408	1.00(3)
756	ED1	C	0.12880	0.12880	0.29711	0.01408	1.00(3)
756	FD1	C	0.31567	0.39142	0.44913	0.01408	1.00(3)

3.9 *In situ*-DRIFT spectroscopy

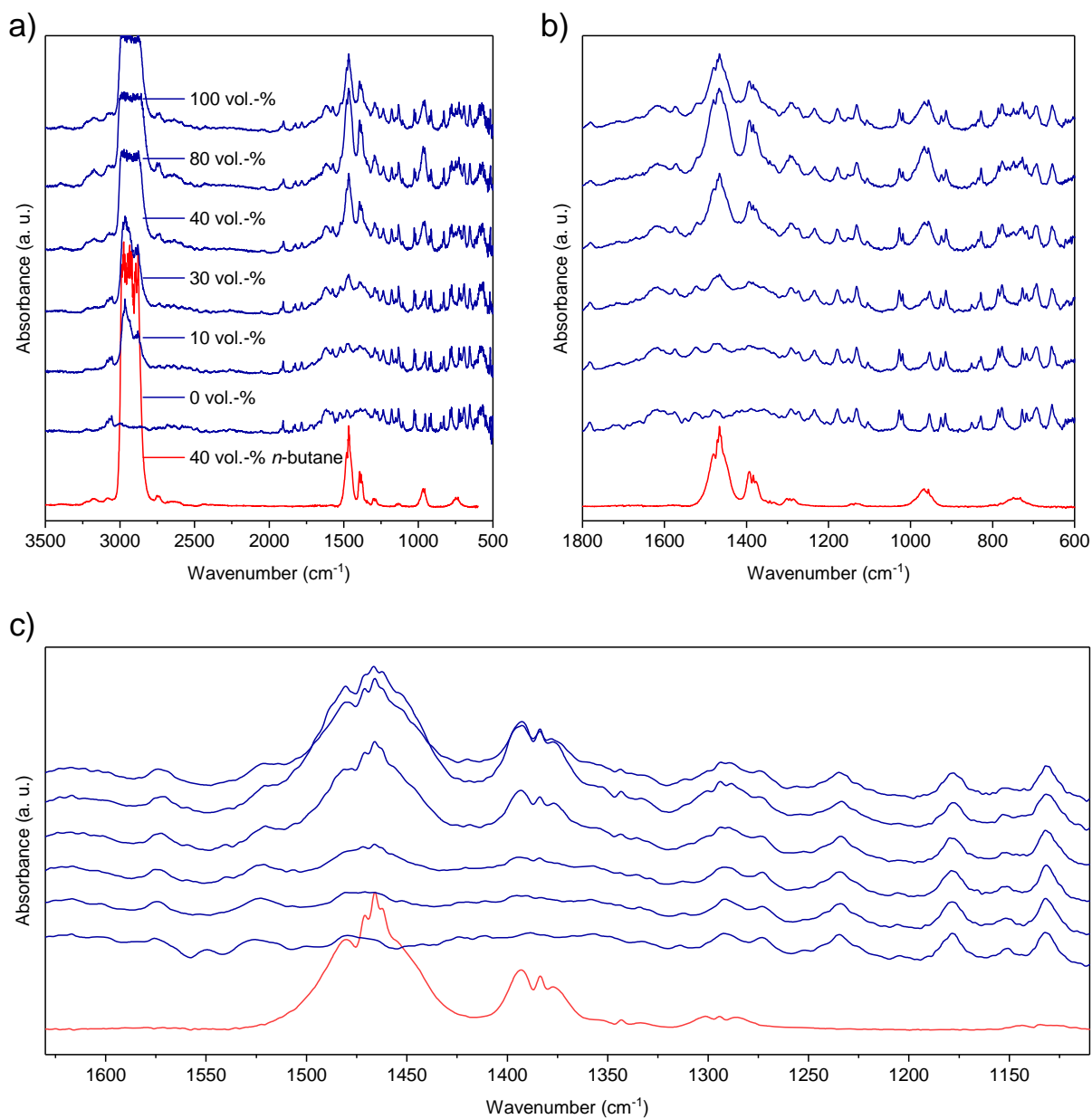
Assignment of vibrational modes of each individual peak in the IR spectra of DUT-48, -46, -49, -50, and -151*int* is difficult and elaborate DFT analysis is beyond the scope of this study. However, each MOF and ligand contains the same 9*H*-carbazole-3,6-dicarboxylate building-block and a C-N bond to an aromatic bridging unit. Vibrational modes of these units will show the same peak positions in the IR spectra. In fact, several peaks with minor variation in wave number can be found in the spectra of all compounds analysed. Peaks which are found for all materials and can be assigned to vibrational modes of C-H, C-C, and C-N vibrations in the ligand backbone are of special interest as they are expected to be impacted by ligand buckling upon structural transition. These peaks are summarized in Supplementary Table 28. Air sensitive samples were analysed in a HARRICK Praying Mantis reaction chamber sealed by a removable dome with IR-transparent ZnSe windows. The same setup was used to perform *in situ* DRIFT analysis by applying a constant flow of a mixture of inert carrier gas (N₂) and adsorptive (*n*-butane or vaporized CCl₄). For the analysis of *n*-butane adsorption, the gas composition was controlled via two mass flow controllers (MFC). The composition during *in situ* adsorption of vaporized CCl₄ was estimated by two valves controlling the flux of inert and CCl₄ saturated inert gas.



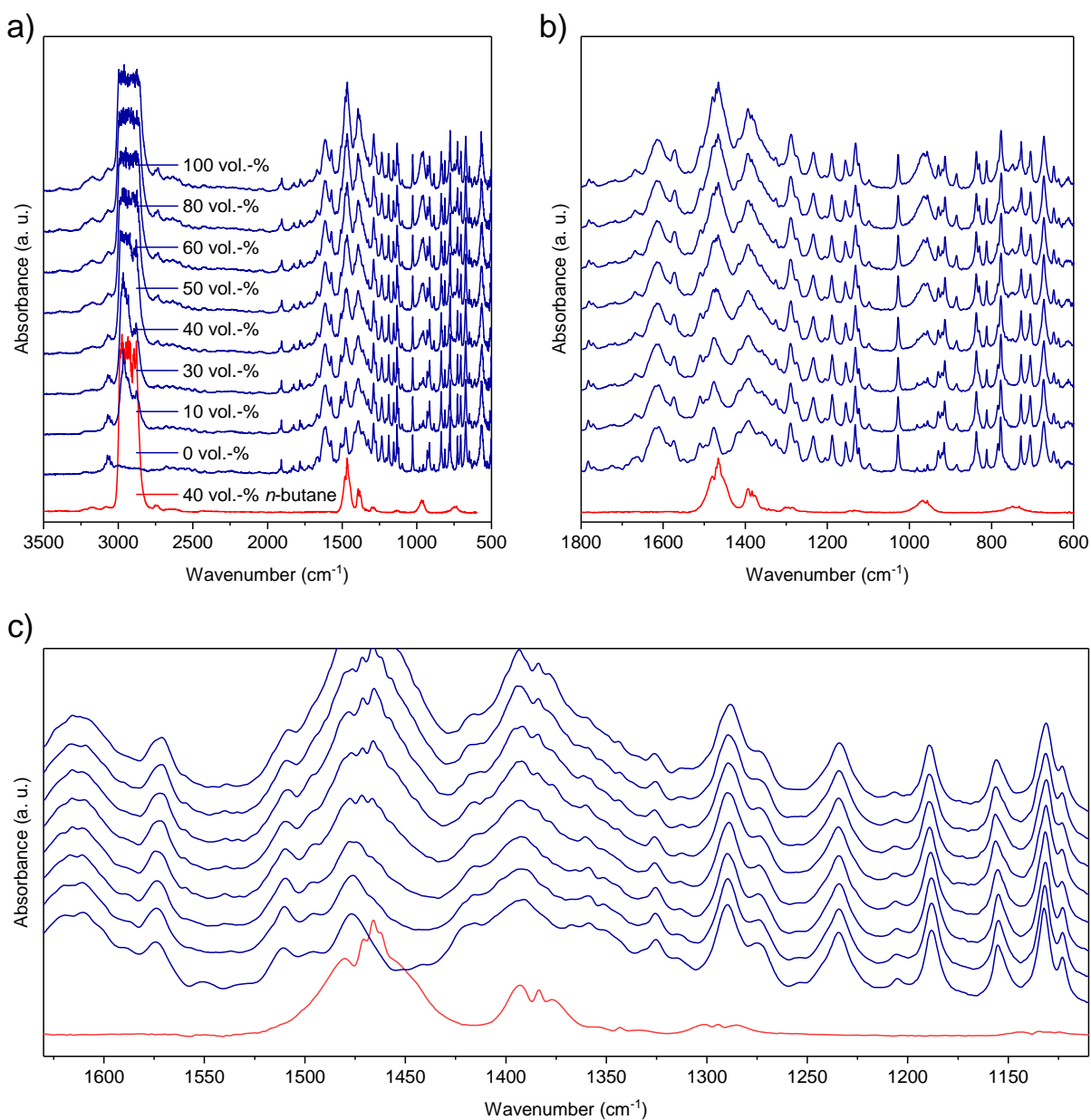
Supplementary Figure 58. a) DRIFT spectra of KBr filled sample holder at different concentrations of *n*-butane at 299 K and b) varying concentrations of CCl₄ vapour in nitrogen.



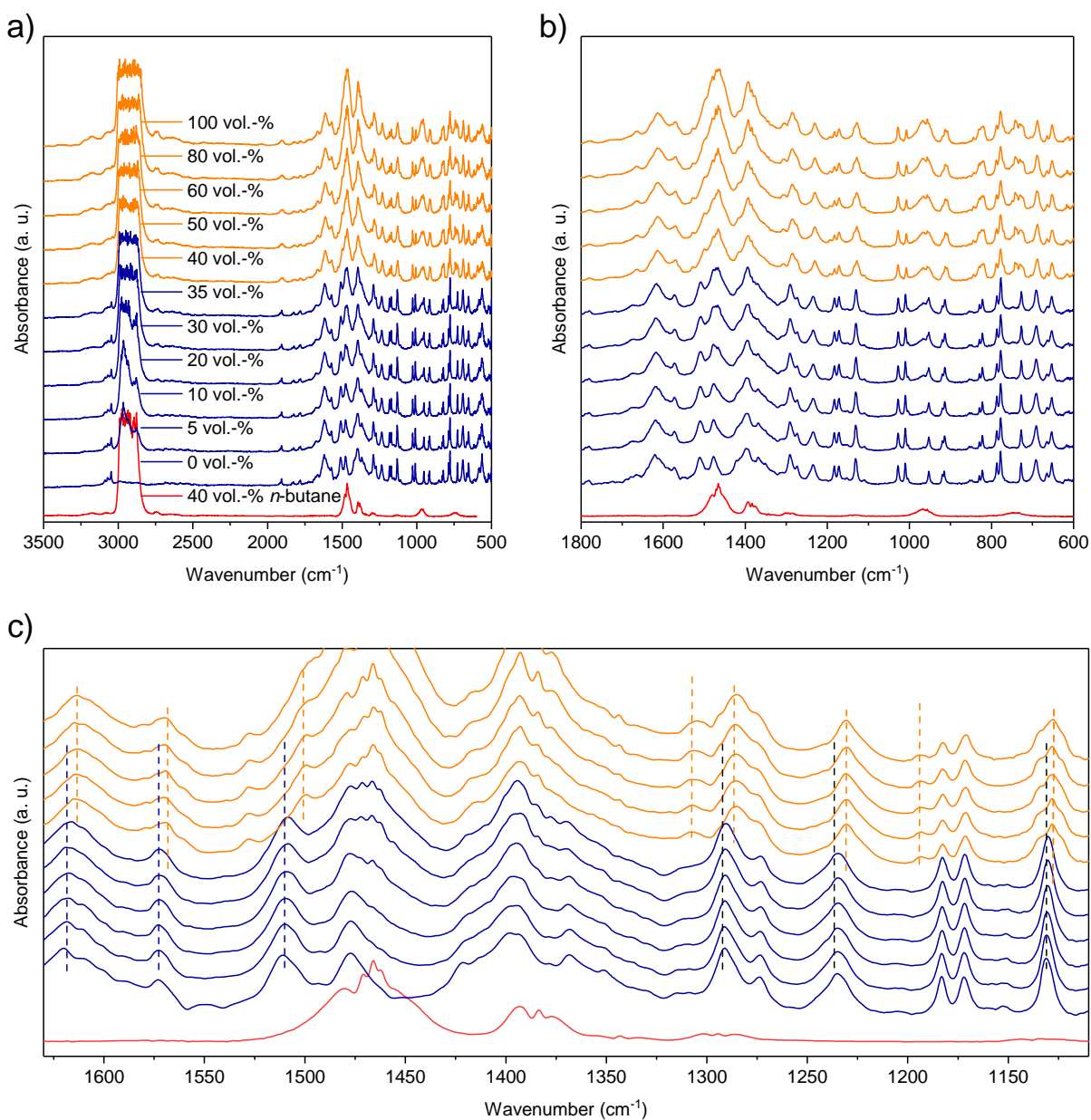
Supplementary Figure 59. a) DRIFT spectra of DUT-48 (red), DUT-46 (orange), DUT-49 (green), DUT-50 (blue), and DUT-151_{int} (purple). b) magnified region of vibrations assigned to the ligand backbone. Vertical dashed lines indicate vibrations found in all materials which are thus assigned to the carbazole cores.



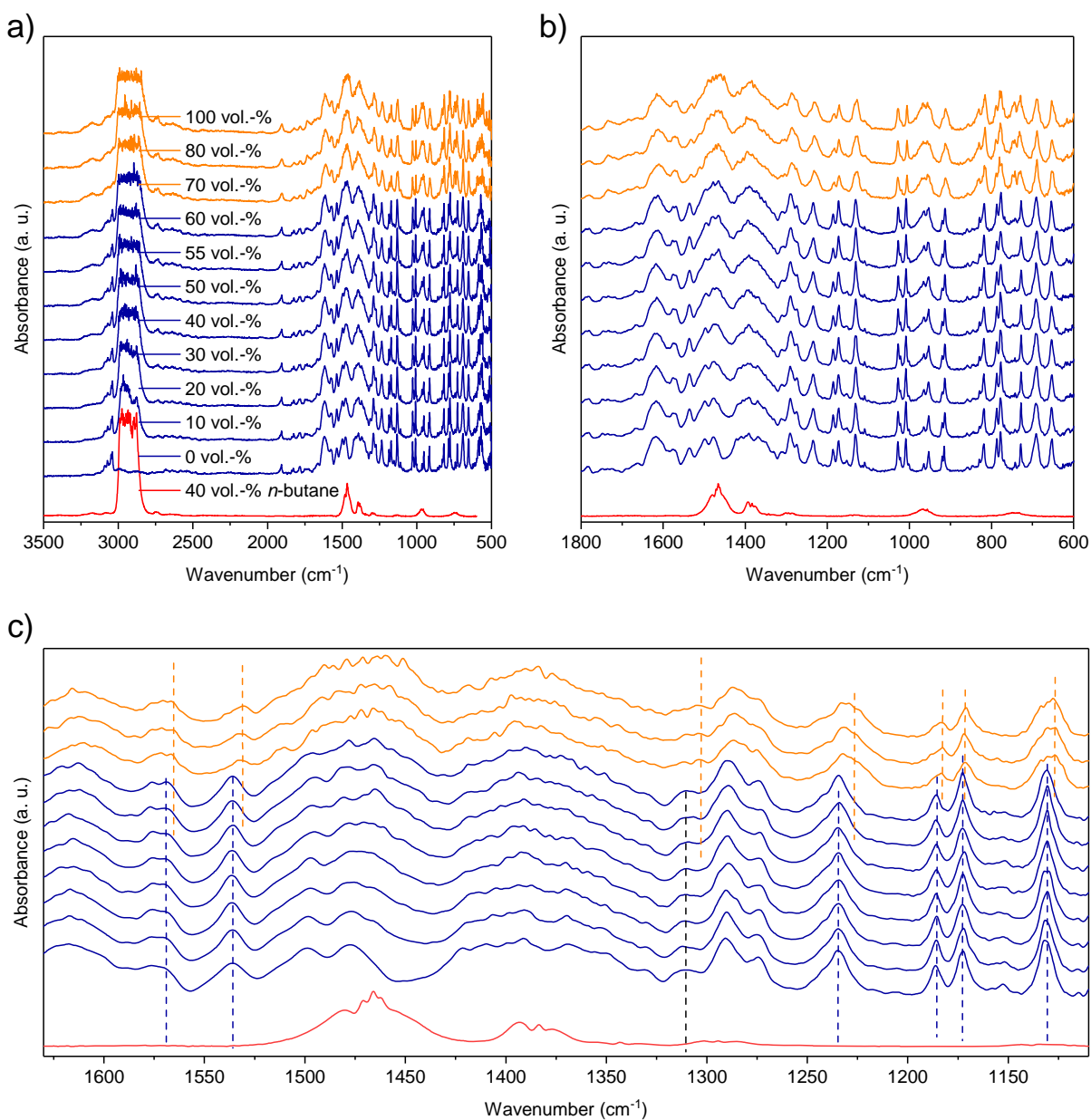
Supplementary Figure 60. a) *In situ*-DRIFT spectra of DUT-48 at varied loadings of *n*-butane at 299 K and b,c) magnifications of fingerprint region.



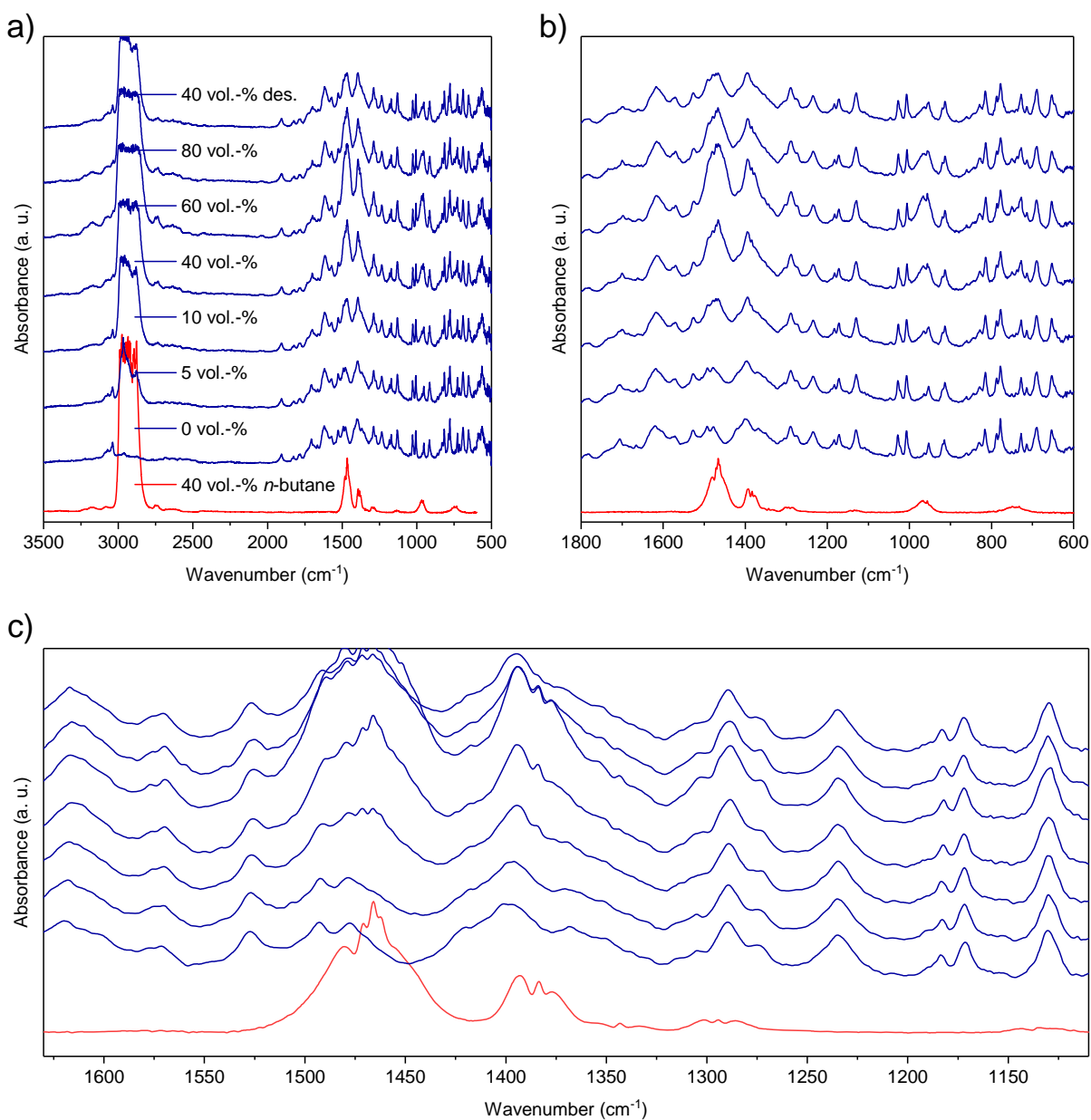
Supplementary Figure 61. a) *In situ*-DRIFT spectra of DUT-46 at varied loadings of *n*-butane at 299 K and b,c) magnifications of fingerprint region.



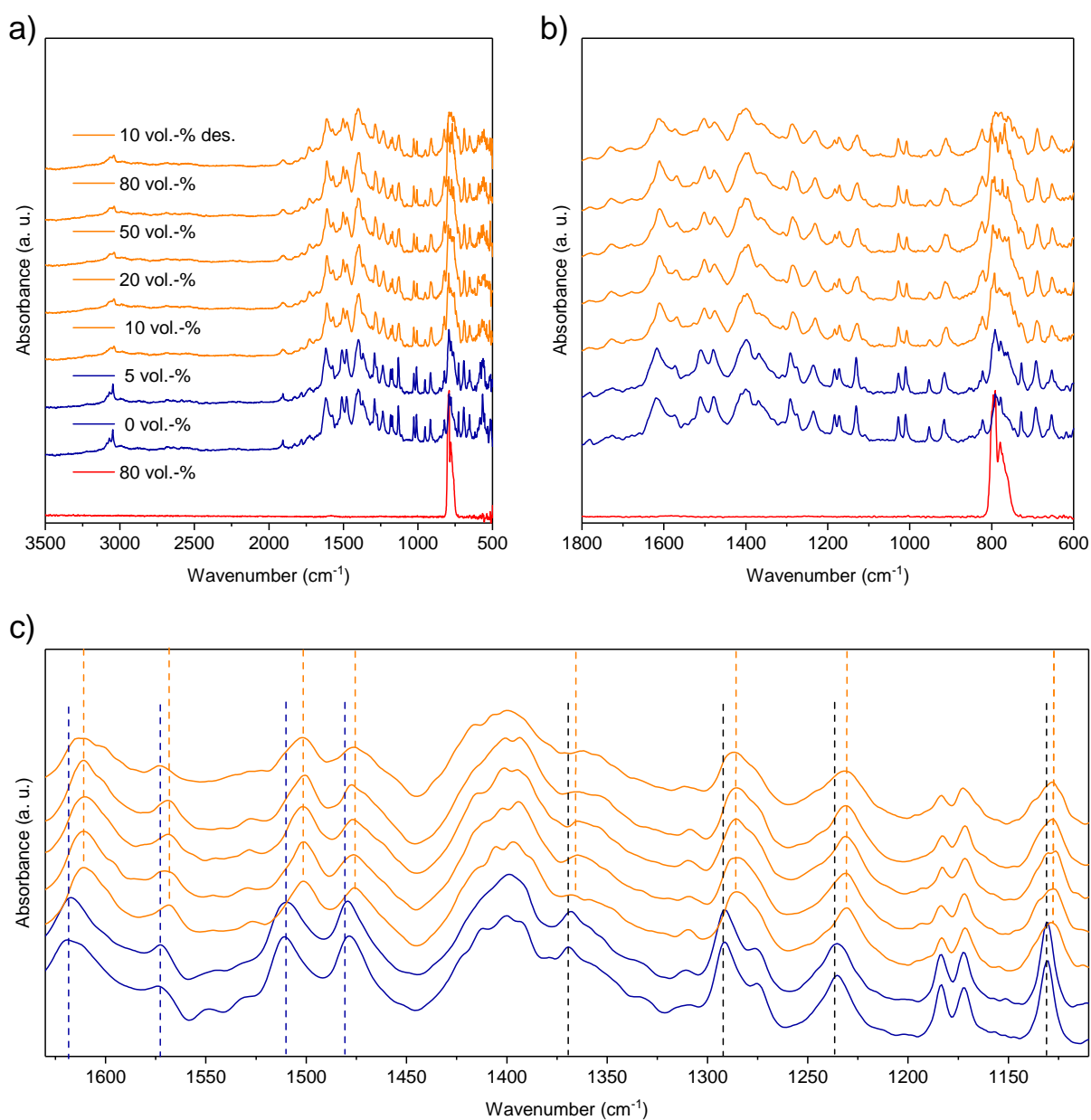
Supplementary Figure 62. a) *In situ*-DRIFT spectra of DUT-49 at varied loadings of *n*-butane at 299 K and b,c) magnifications of fingerprint region. Color code: blue: before transition, orange: after transition, dashed lines indicate shifts of peaks.



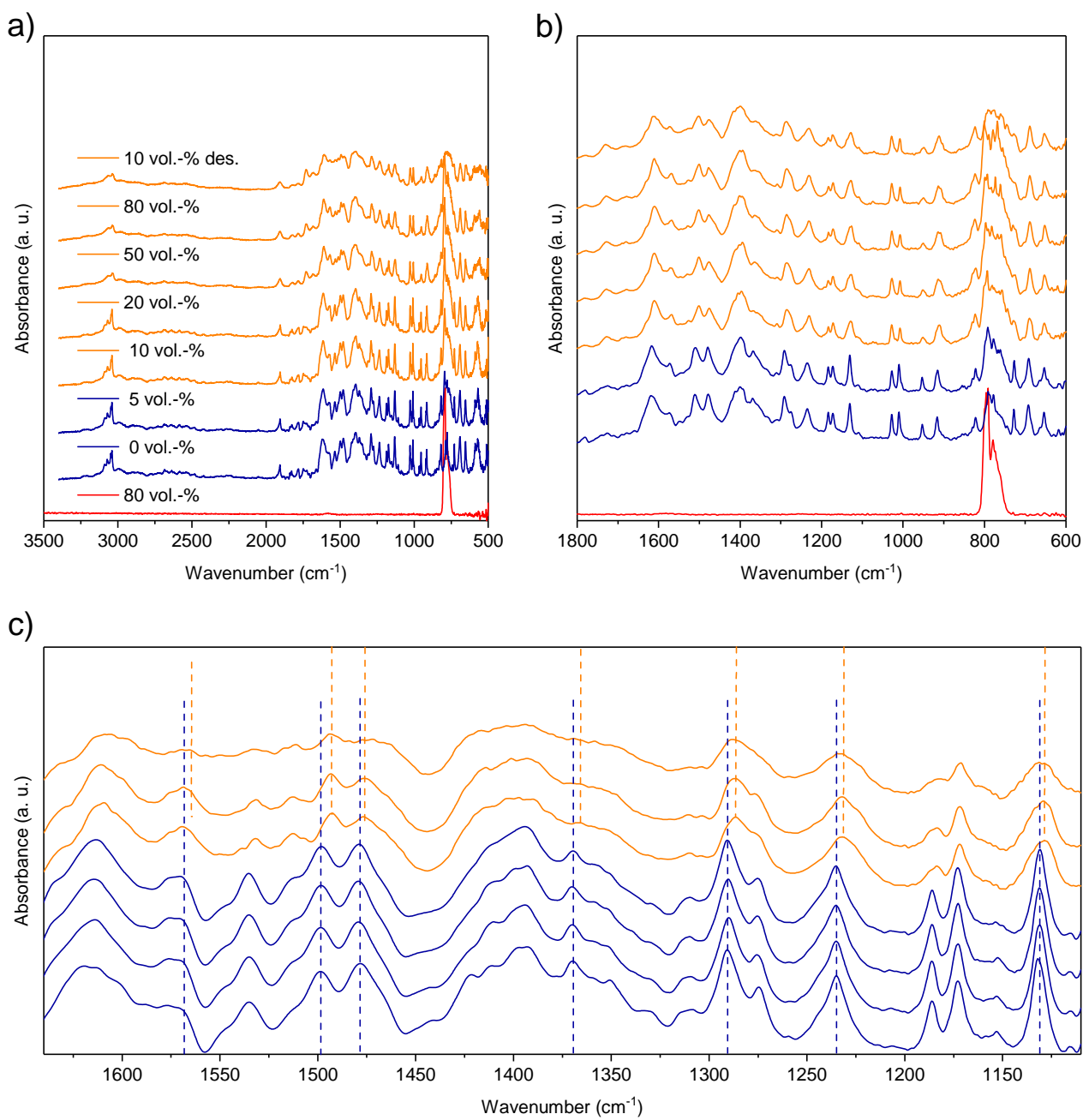
Supplementary Figure 63. a) *In situ*-DRIFT spectra of DUT-50 at varied loadings of *n*-butane at 299 K and b,c) magnifications of fingerprint region. Color code: blue: before transition, orange: after transition, dashed lines indicate shifts of peaks.



Supplementary Figure 64. a) *In situ*-DRIFT spectra of DUT-151 at varied loadings of *n*-butane at 299 K and b,c) magnifications of fingerprint region.



Supplementary Figure 65. a) *In situ*-DRIFT spectra of DUT-49 at varied loadings of CCl_4 at 299 K and b,c) magnifications of fingerprint region. Color code: blue: before transition, orange: after transition, dashed lines indicate shifts of peaks.



Supplementary Figure 66. a) *In situ*-DRIFT spectra of DUT-50 at varied loadings of CCl₄ at 299 K and b,c) magnifications of fingerprint region. Color code: blue: before transition, orange: after transition, dashed lines indicate shifts of peaks.

For DUT-49 and DUT-50, a shift in peak position to lower wavenumbers is observed upon adsorption of *n*-butane and CCl₄ which can be assigned to the structural contraction previously analysed by *in situ* PXRD. Several peaks are found to be affected in the spectra of DUT-49 in Supplementary Figure 62 (*n*-butane), Supplementary Figure 65 (CCl₄) and for DUT-50 in Supplementary Figure 63 (*n*-butane), Supplementary Figure 66 (CCl₄), respectively. The peaks which are shifted upon structural contraction are mostly different from the peaks found to be identical for the whole series of MOFs summarized in Supplementary Table 28. Consequently, they can most likely be assigned to changes of vibrational modes in the bridging units of the linkers and not the carbazole core.

Supplementary Table 28. Experimental peaks observed by *in situ* DRIFT spectroscopy in comparison with assigned peaks from reference ⁴².

Material ID	Wave number (cm ⁻¹)							
DUT-48	1610 (br)	1575	1478	1423	1291	1272	1234	1132
DUT-46	1620	1573	1476	1418	1289	1273	1234	1132
DUT-49	1619	1572	1508	1289	1234	n. a.	n. a.	1131
DUT-49 (CCl ₄)	1610	1558	1501	1284	1230	n. a.	n. a.	1127
DUT-49 (<i>n</i> -butane)	1613	1569	1499	1286	1229	n. a.	n. a.	1128
DUT-50	1569	1479	1311	1290	1234	1185	1172	1131
DUT-50 (CCl ₄)	1566	1475	1302	1285	1231	1182	1170	1128
DUT-50 (<i>n</i> -butane)	1565	1477	1303	1285	1231	1182	1170	1127
DUT-151	1619	1571	1477	1420	1289	1274	1233	1128
Reference ⁴²	1620	1497	1442	1364	1343	1299	1217	n. a.
Reference ⁴² - assignment [#]	$\nu(\text{C-C})_{\text{b}}$, $\delta(\text{C-H})_{\text{ip}}$	$\delta(\text{C-H})_{\text{ip,b}}$, $\nu(\text{C-N})$	$\delta(\text{C-H})_{\text{ip,c}}$	$\delta(\text{C-H})_{\text{ip}}$, $\nu(\text{C-N})$	$\delta(\text{C-H})_{\text{ip}}$, $\nu(\text{C-N}), \nu(\text{C-C})$	$\delta(\text{C-H})_{\text{ip}}$	$\delta(\text{C-H})_{\text{ip,c}}$	n. a.

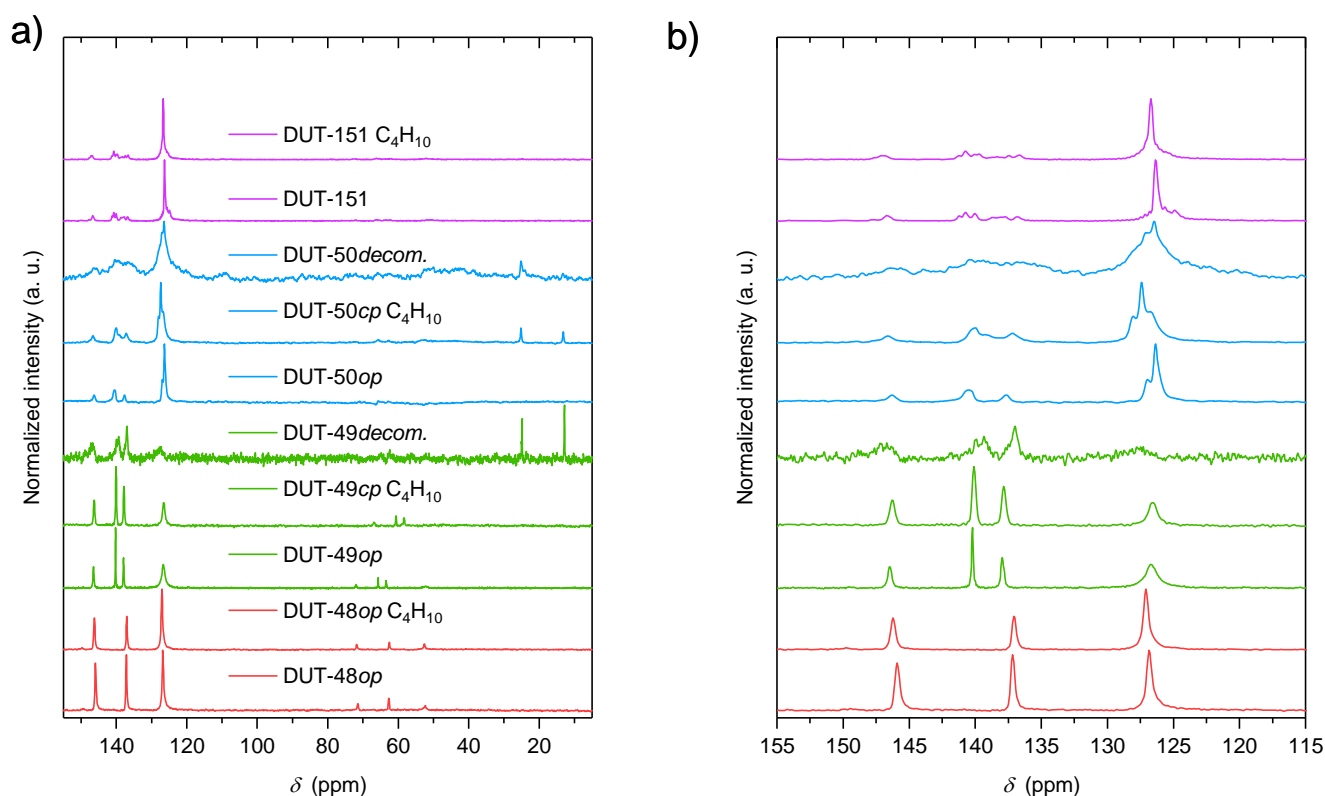
[#] δ and ν refer to deformation and stretching modes, respectively. 'ip' indicate in plane modes. 'c' and 'b' indicate a dominant localization on the carbazole groups or biphenyl, respectively.

3.10 Solid state MAS NMR studies

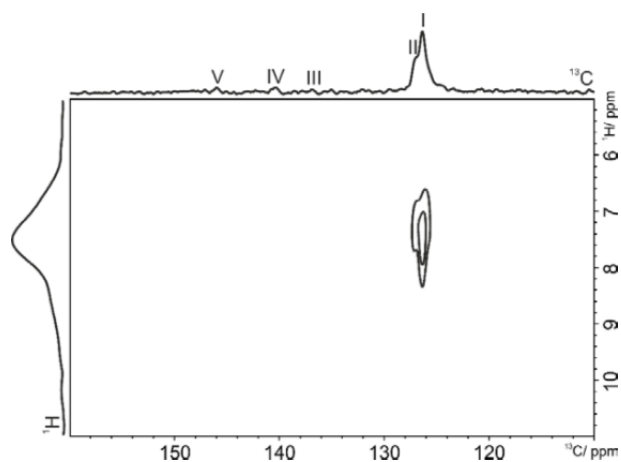
Solid-state NMR measurements were carried out on a Bruker Ascend 800 spectrometer equipped with a 3.2 mm HX probe. The ¹H-¹³C cross polarization experiments were performed at a resonance frequency of 800.2 MHz for protons and 201.2 MHz for carbon. The contact time was 4 ms and the relaxation delay

was 3 s. A sample rotation of 15 kHz was chosen. The ^{13}C chemical shift was referenced using adamantane.

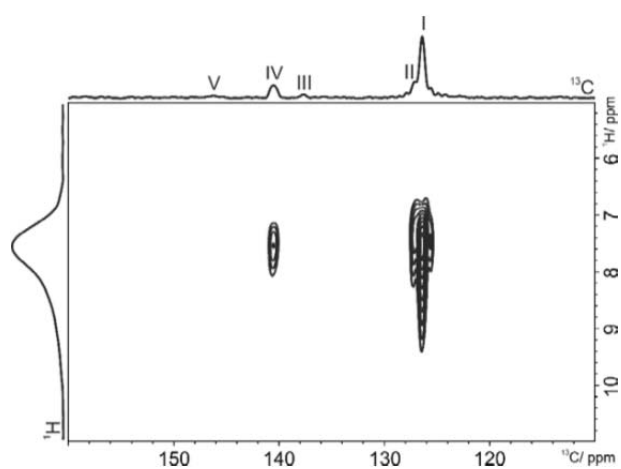
The rotor was filled with the activated material (*op*-phase) under argon atmosphere. After NMR analysis of argon-filled DUT-49*op*, the rotor was opened under *n*-butane atmosphere and equilibrated for 2 min to obtain the *cp*-phase of the MOF. Formation of the *cp*-phase under these conditions was confirmed in a separate experiment by *in situ* PXRD. After sealing the rotor, the measurements of the butane filled *cp*-phase were carried out. Subsequently, the rotor was re-opened allowing the sample to have extended contact to ambient conditions and moisture which is known to initiate decomposition of the material. For these samples no reflections in the PXRD patterns could be observed.



Supplementary Figure 67. Solid state ^{13}C CP MAS NMR spectra for DUT-48, DUT-49, DUT-50 and DUT-151 filled with argon and *n*-butane at 298K.



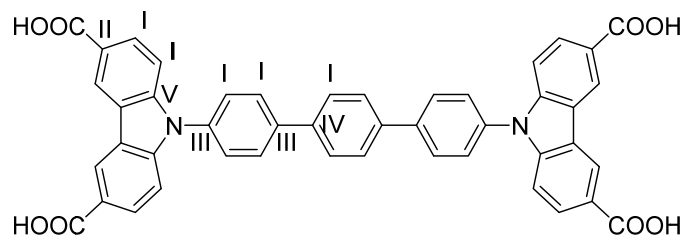
Supplementary Figure 68. ^{13}C - ^1H -HETCOR- spectrum of Ar-filled DUT-50op at a contact time of 0.7 ms ($\nu_{\text{rot}} = 15$ kHz).



Supplementary Figure 69. ^{13}C - ^1H -HETCOR spectrum of Ar-filled DUT-50op at a contact time of 4 ms ($\nu_{\text{rot}} = 15$ kHz).

Supplementary Table 29. Peak assignment of ^{13}C NMR signals in DUT-50.

Signal	δ (ppm)	Assignment
I	126.3	CH
II	127.0	C
III	137.7	C
IV	140.5	C
V	146.3	C



Supplementary Figure 70. Chemical structure of L_4 and assignment of ^{13}C NMR signals. The assignment of signal I to the CH groups and II-V to quaternary could be further corroborated by solid-state APT (attached proton test) experiments (data not shown). The assignment of signals II-V observed for intact DUT-50 to the designated carbon positions in the linker is suggested based on chemical shift predictions calculated with the computer program ChemDraw.

4 Computational Methods

4.1 Simulation of structural models of MOFs

The structural models were simulated using Material Studio 5.0 software package³⁴. Initial structural models for DUT-46, DUT-50 and DUT-151 are based on the experimental single crystal structures of DUT-49⁴³ and DUT-48². Because these experimental crystal structures contain disordered phenylene backbones, disorder-free models were obtained by reducing the crystal symmetry from $Fm\bar{3}m$ to $Pa\bar{3}$ and subsequent removal of the disordered positions. For simulation of DUT-46 the phenylene group in DUT-48 was substituted by a 2,6-naphthylene unit. DUT-50 was modelled by adding an additional phenylene unit to the ligand in DUT-49. For the non-interpenetrated structure of DUT-151, which could not be obtained experimentally, an additional phenyl ring was inserted in the ligand backbone of DUT-50. The geometry of the structure and lattice parameters including the disorder free structures of DUT-48 and DUT-49 were optimized using UFF force field, integrated into Material Studio 5.0. Subsequently, the simulated structural models were reduced in symmetry to $P1$, optimized using the MOF-FF force field⁴⁴ as described in section 4.3. Final lattice parameters were taken from (N , V , T) simulations of the *op* and *cp* minima (see Figure 1 main text) and the energy and structures were minimized iteratively adjusting the coordinates and cell parameters using the lammmps minimize and box/relax commands with default convergence criteria.

Cif files of the structural models for *op* phases can be obtained from the supplementary information.

Supplementary Table 30. Unit cell parameter derived from structural modelling for the disorder free *op* phases in $Pa\bar{3}$ space group.

	DUT-48	DUT-46	DUT-49	DUT-50	DUT-151
Simulated unit cell volume (\AA^3)	63570.67	79761	97153	141092	199196
Simulated lattice parameter, a (\AA)	39.91	43.045	45.971	52.059	58.55
Experimental unit cell volume (\AA^3)	66381(14)	82597(28)	101117(19)	145781(51)	n. a.
Experimental lattice parameter, a (\AA)	40.490(5)	43.550(5)	46.588(5)	52.630(6)	n. a.

4.2 Density Functional Theory Simulations

Ligands $L_1 - L_5$ were simulated as the corresponding acids using density functional theory (DFT) employed by the CRYSTAL14 software. Localized TZVP basis sets and the hybrid exchange-correlation functional PBE0 were used. Dispersion corrections were included using the Grimme “D2” approach. Ligand structures were strained by a decrease in the N–N length from the local minimum to a compressive strain of 0.06, in 40 steps. For each step, the structure was optimized with the N–N length fixed. Subsequently, a stress-strain curve relative to this axial compressive deformation of the ligand was generated; stress is defined by the gradient of the energy, and strain is the relative decrease in N–N length.

4.3 Molecular dynamics simulations

Molecular dynamics simulations to produce equations of states for DUT-46, DUT-48, DUT-49, DUT-50, DUT-151*int* and DUT-151 used a modified MOF-FF force field⁴⁴ adapted to lammmps to describe the bonds, angles, dihedrals and improper dihedrals present in the frameworks. Further details can be found in the supporting information. Representative input files for molecular simulations are available online in our data repository at <https://github.com/fxcoudert/citable-data>

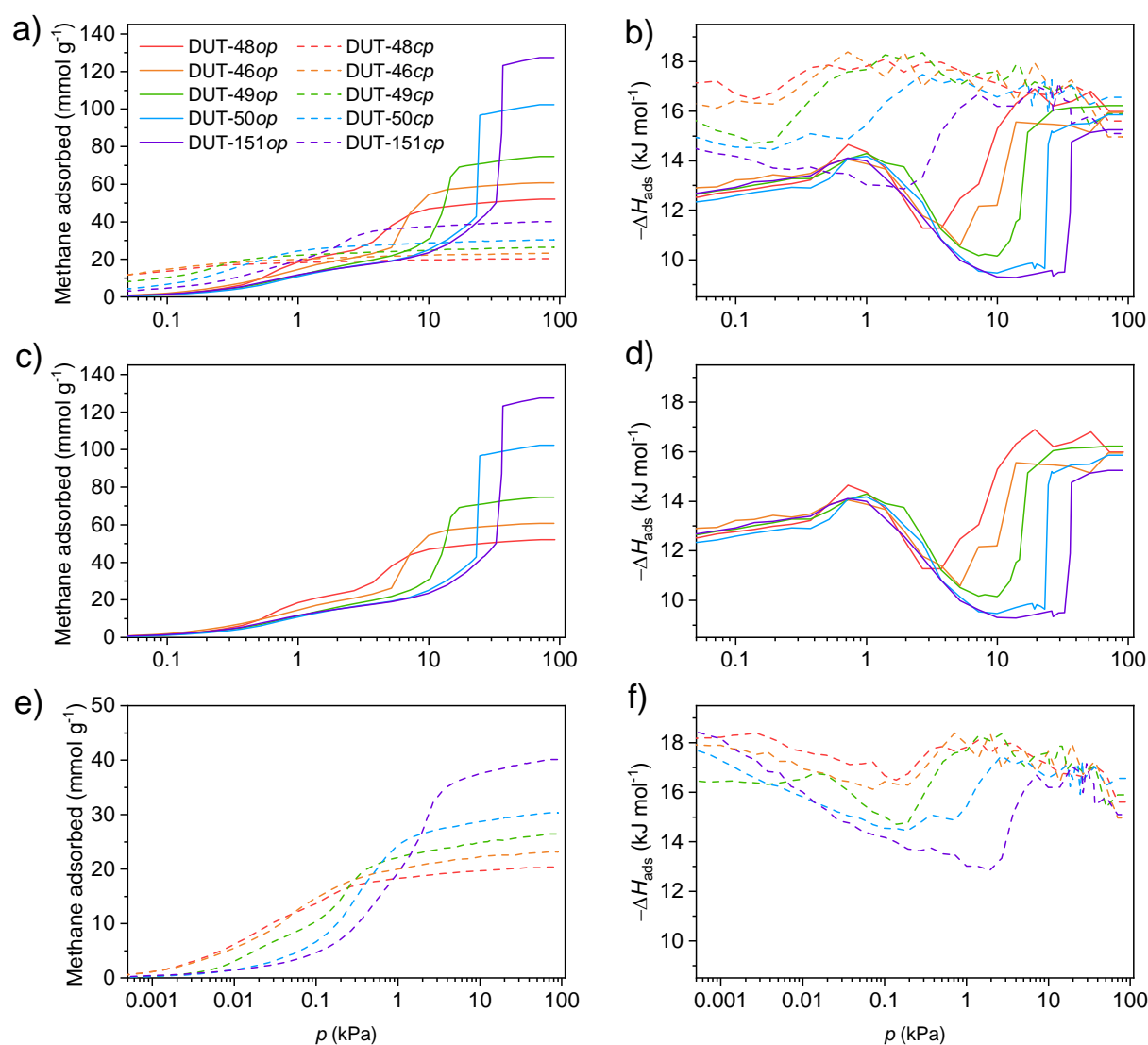
Supplementary Table 31. Structure parameter derived from the MD simulations.

	DUT-48	DUT-46	DUT-49	DUT-50	DUT-151
Global minimum (Unit cell volume <i>op</i>) (\AA^3)	63044	78402	96071	142645	197645
Local minimum (Unit cell volume <i>cp</i>) (\AA^3)	35287	41421	45882	58185	74988
Unit cell volume structural model <i>cp</i> (\AA^3)	36674	41501	47360	57858	76227
Simulated transition pressure (MPa)	145	84	65	38	22
Free energy difference <i>op-cp</i> ($\text{kJ mol}_{\text{uc}}^{-1}$)	892	793	768	598	336

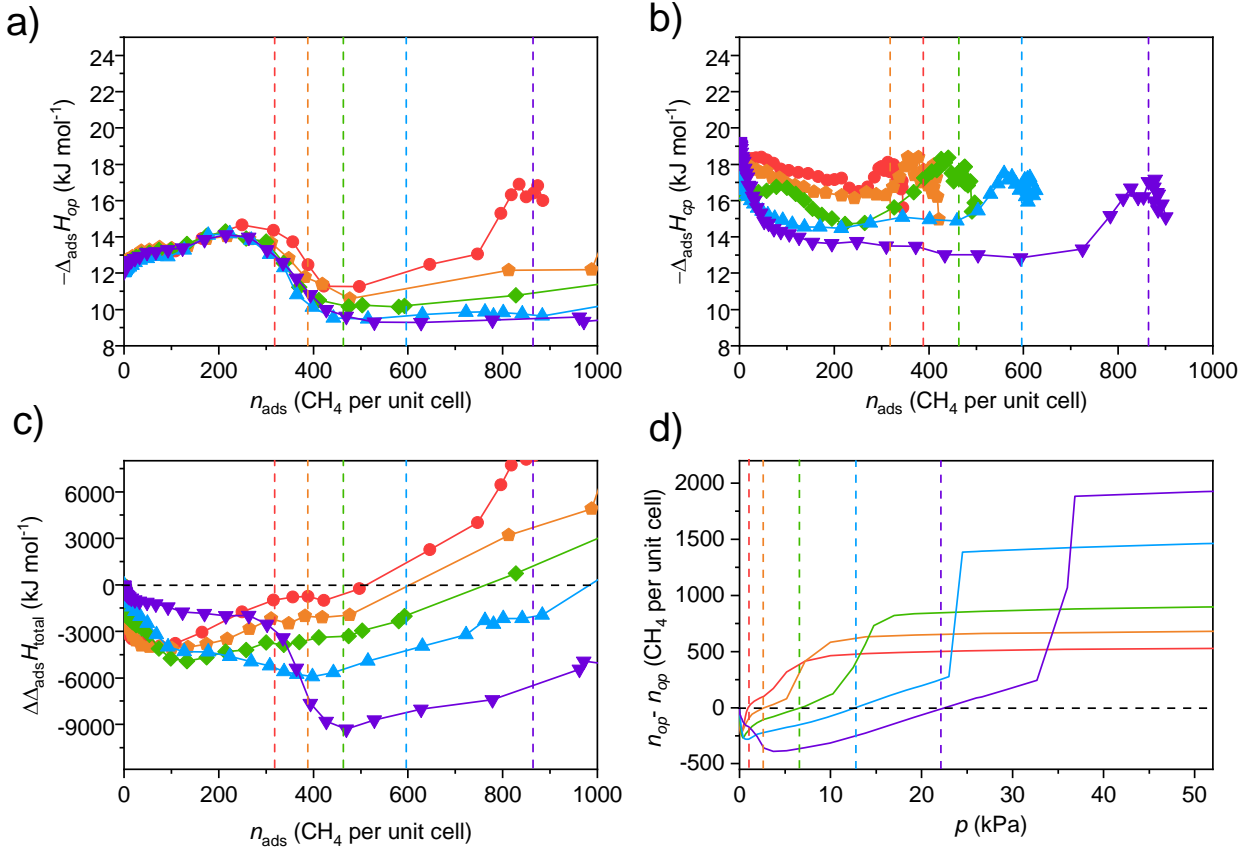
Structural models of the *cp* phase were obtained from the MD simulation at the local minimum of reduced unit cell volume. The final structural models are based on geometrical optimization using the above described force fields in the space group *P1*.

4.4 Grand Canonical Monte Carlo Simulations

Grand Canonical Monte Carlo (GCMC) simulations using the RASPA2.0 code.³⁴ Equilibration used 5×10^5 cycles and the subsequent 1×10^6 cycles were sampled, for each pressure point. Temperature was set to 111 K. The van der Waals interactions for the framework used the UFF force field and methane the united-atom TraPPE force field. Parameters for framework-gas interactions were obtained by Lorentz-Berthelot mixing rules. No charges were considered for the framework atoms.



Supplementary Figure 71. a,c,e) Simulated methane adsorption isotherms at 111 K. b,d,f) Corresponding enthalpy profiles. Color code: DUT-48 (red), DUT-46 (orange), DUT-49 (green), DUT-50 (blue), DUT-151 (purple), *op* (full lines) and *cp* (dashed lines).



Supplementary Figure 72. a,b) Adsorption enthalpies for methane adsorption at 111 K plotted against the loading in the *op* (a) and *cp* phases (b) of DUT-48 (red), DUT-46 (orange), DUT-49 (green), DUT-50 (blue), DUT-151 (purple). c) evolution of $\Delta\Delta_{\text{ads}}H_{\text{total}}$ with loading and d) the difference in uptake between the *op* and *cp* phase plotted against pressure. Intersections of the *op*-*cp* isotherms are indicated as vertical dashed lines.

At the intersection of the isotherms, $n_{\text{ads}} = n_{\text{ads},op} = n_{\text{ads},cp}$, indicated as dashed lines in Supplementary Figure 72, the difference in adsorption enthalpy of methane adsorbed in the *op* and *cp* phase increases from 3.7 kJ mol^{-1} methane in DUT-48 to 7.4 kJ mol^{-1} methane in DUT-50. The total gain in adsorption enthalpy upon structural contraction per unit cell, $\Delta\Delta_{\text{ads}}H_{\text{total}}$, at the intersection of the isotherms of *op* and *cp* phase can be estimated by multiplying the difference of adsorption enthalpy in the *op* and *cp* phase, $\Delta\Delta_{\text{ads}}H = \Delta_{\text{ads}}H_{cp} - \Delta_{\text{ads}}H_{op}$ with the amount of gas adsorbed per unit cell, n_{ads} .

$$\Delta\Delta_{\text{ads}}H_{\text{total}} = (\Delta_{\text{ads}}H_{cp} - \Delta_{\text{ads}}H_{op}) \cdot n_{\text{ads}} \quad (4)$$

Estimations of $\Delta\Delta_{\text{ads}}H_{\text{total}}$ for the series of materials are $-1177 \text{ kJ mol}^{-1}$ (DUT-48), $-2289 \text{ kJ mol}^{-1}$ (DUT-46), $-3491 \text{ kJ mol}^{-1}$ (DUT-49), $-4458 \text{ kJ mol}^{-1}$ (DUT-50), $-6290 \text{ kJ mol}^{-1}$ (DUT-151).

Supplementary Table 32. Adsorption enthalpy estimations for *op-cp* transitions derived from the GCMC simulations.

	DUT-48	DUT-46	DUT-49	DUT-50	DUT-151
p at intersection (kPa)	1.05	2.6	6.8	12.9	22.3
$n_{ads} = n_{ads,op} = n_{ads,cp}$ (molecules CH ₄ per unit cell)	318	388	463	596	864
$\Delta\Delta_{ads}H = \Delta_{ads}H_{cp} - \Delta_{ads}H_{op}$ (kJ mol ⁻¹)	-3.7	-5.9	-7.54	-7.48	-7.28
$\Delta\Delta_{ads}H_{total} = (\Delta_{ads}H_{cp} - \Delta_{ads}H_{op}) \cdot n_{ads}$ (kJ mol ⁻¹)	-1177	-2289	-3491	-4458	-6290

Equation (4) can be generalized to reflect the adsorptive part of the energetic driving force for the entire pressure range $n_{ads,op} \neq n_{ads,cp}$. $\Delta\Delta_{ads}H_{total}$ is the total difference in adsorption enthalpy for the *op-cp* transition of one unit cell.

$$\Delta\Delta_{ads}H_{total} = \Delta_{ads}H_{cp} \cdot n_{ads,cp} - \Delta_{ads}H_{op} \cdot n_{ads,op} \quad (5)$$

The quantity

$$\Delta\Delta_{ads}H = \Delta_{ads}H_{cp} - \Delta_{ads}H_{op} < 0 \quad (6)$$

is the difference in adsorption enthalpies for the *op* and *cp* phase. Equation (5) can be rearranged to reflect the total adsorptive enthalpy difference with respect to $\Delta n = n_{op} - n_{cp}$.

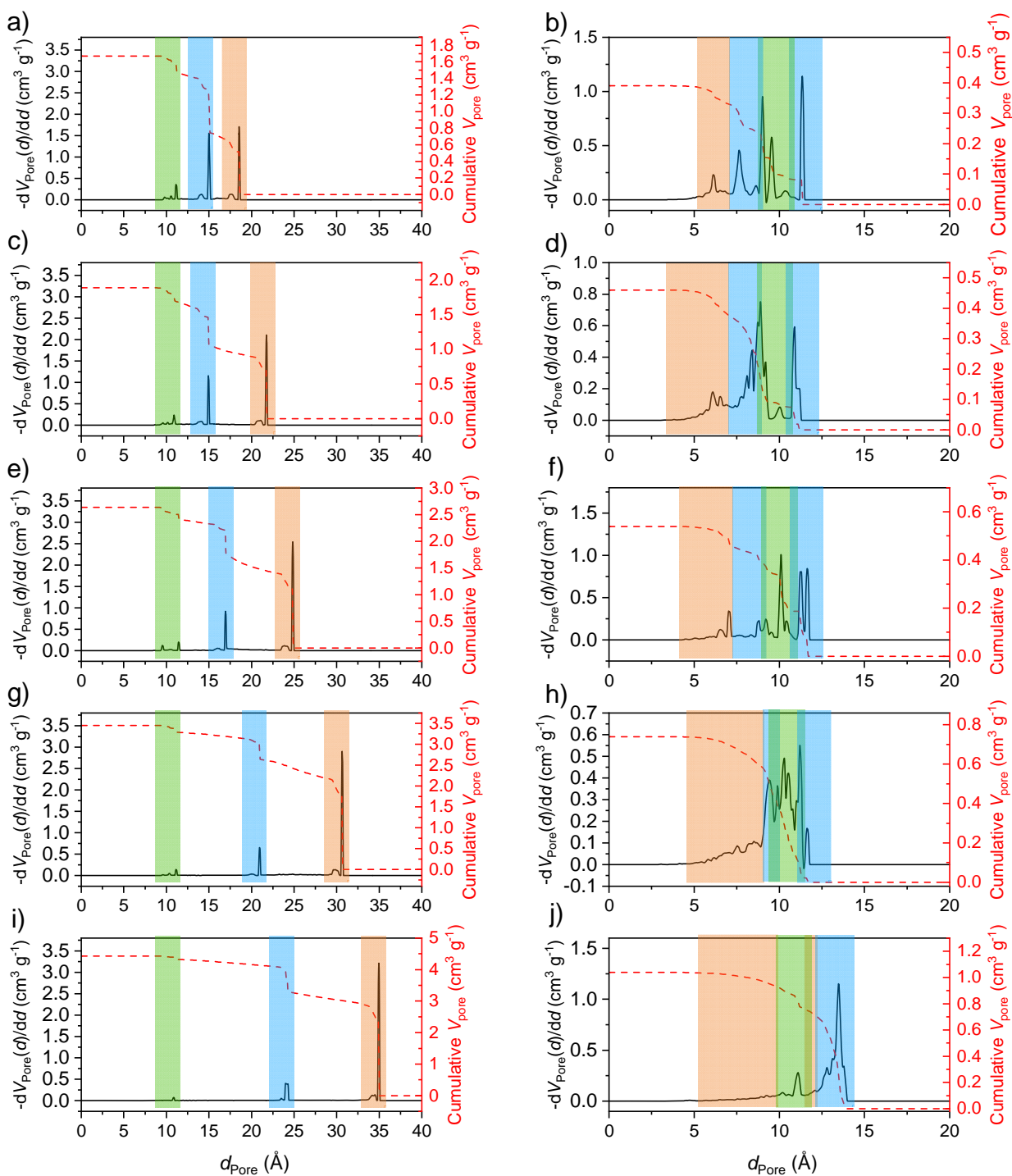
$$\Delta\Delta_{ads}H_{total} = \Delta_{ads}H_{cp} \cdot n_{ads,cp} - \Delta_{ads}H_{op} \cdot (\Delta n + n_{ads,cp}) \quad (7)$$

$$\Delta\Delta_{ads}H_{total} = \Delta\Delta_{ads}H \cdot n_{ads,cp} - \Delta_{ads}H_{op} \cdot \Delta n \quad (8)$$

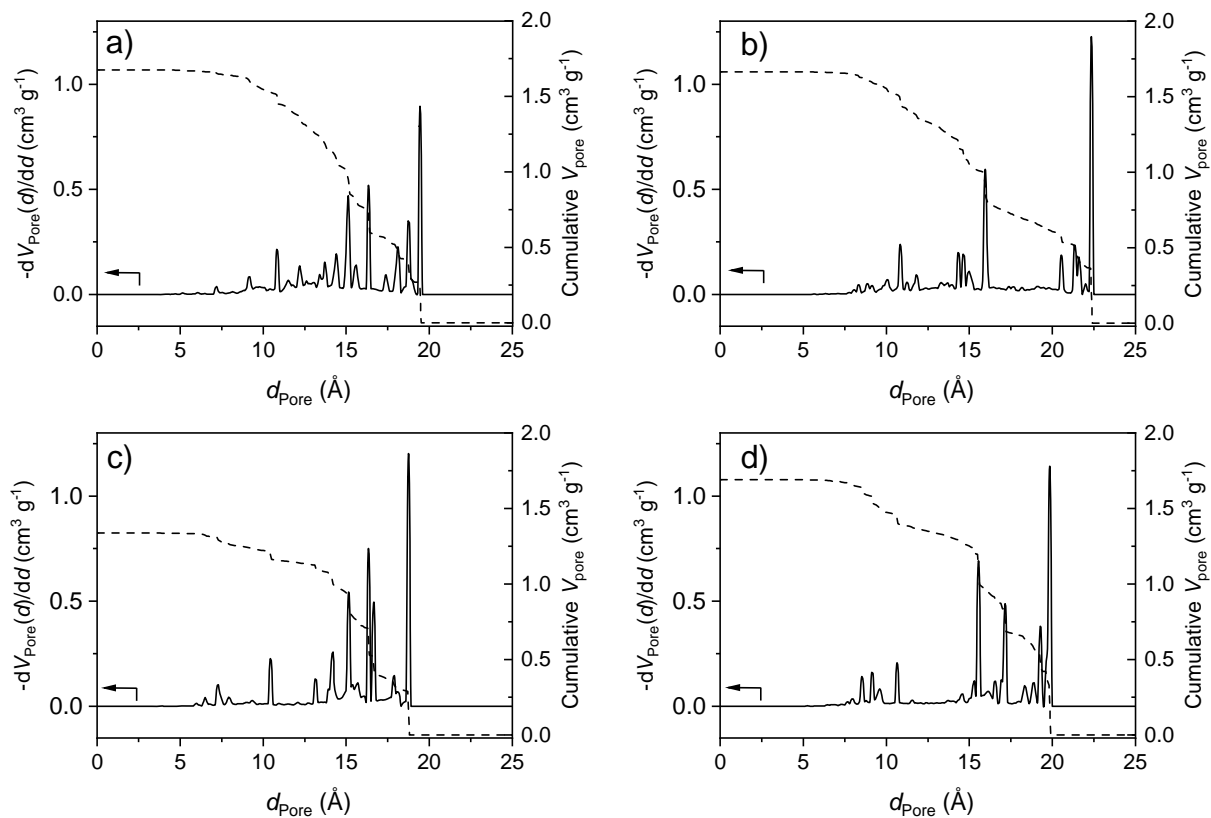
For the negative gas adsorption transition: $\Delta n = \Delta n_{NGA}$. In equation (8) $\Delta\Delta_{ads}H \cdot n_{ads,cp}$ represents the adsorptive driving force for the contraction and $\Delta_{ads}H_{op} \cdot \Delta n$ the driving force for the expansion.

4.5 Pore size distribution

Pore size distributions (PSD) were simulated for these structures using the Zeo++ code¹⁶ on the basis of *in silico* determined crystal structures for the *op* and *cp* phases for DUT-48-151 (Supplementary Figure 73). In addition, PSD for various refined phases of DUT-151*int* were performed on the experimentally refined crystal structures (Supplementary Figure 74). Pore volume and pore sizes are summarized in Supplementary Table 33 and surface area and pore volume in comparison to experimental results are summarized in Supplementary Table 7.



Supplementary Figure 73. Simulated pore size distributions (black lines) and cumulative pore volumes (red dashed lines) of a) DUT-48 op , b) DUT-48 cp , c) DUT-46 op , d) DUT-46 cp , e) DUT-49 op , f) DUT-49 cp , g) DUT-50 op , h) DUT-50 cp , i) DUT-151 op , and j) DUT-151 cp . Colour code trimodal pore system: octahedral (oct, orange), tetrahedral (tet, blue), cuboctahedral (cub, green).



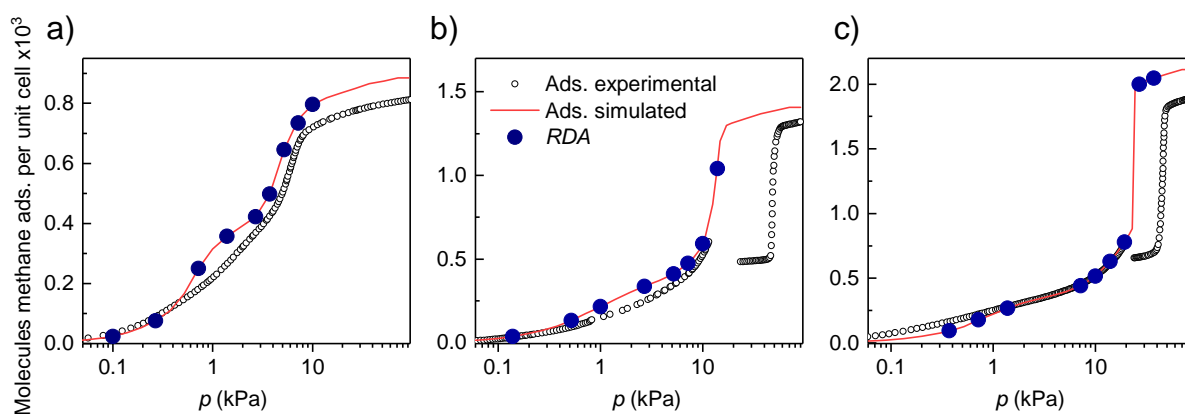
Supplementary Figure 74. Simulated pore size distributions (black lines) and cumulative pore volumes (red dashed lines) of a) DUT-151 int , b) DUT-151 $int-act$, c) DUT-151 $int-cp$, and d) DUT-151 $int-op$. Cumulative pore volume is given as dashed black line.

Supplementary Table 33. Pore size distributions and fractional pore volumes extracted from Supplementary Figure 73. Values for the *cp* phases were only partially estimated due to overlapping.

Material ID	Pore	V_{Pore} (cm ³ g ⁻¹)	Open pore		Contracted pore		
			d_{Pore} (Å)	V_{Pore} fract. (cm ³ g ⁻¹)	V_{Pore} (cm ³ g ⁻¹)	d_{Pore} (Å)	V_{Pore} fract. (cm ³ g ⁻¹)
DUT-48	Cub	total	10.8	0.27	total	10.9	n. a.
	Tet	1.67	15	0.62		n. a.	n. a.
	Oct		18.5	0.78		6.1	0.05
DUT-46	Cub	total	10.8	0.19	total	10.9	n. a.
	Tet	1.89	14.9	0.74		n. a.	n. a.
	Oct		21.7	0.96		6.1-6.5	0.08
DUT-49	Cub	total	10.8	0.23	total	10.9	n. a.
	Tet	2.64	16.9	0.87		n. a.	n. a.
	Oct		24.9	1.54		6.5-7	0.09
DUT-50	Cub	total	10.8	0.19	total	11	n. a.
	Tet	3.45	21	0.84		n. a.	n. a.
	Oct		30.7	2.43		6.5-8.5	0.13
DUT-151	Cub	total	10.8	0.14	total	11.1	n. a.
	Tet	4.43	24	1.16		n. a.	n. a.
	Oct		34.9	3.13		8.7-10.3	0.14

4.5.1 Adsorbate distribution and radial distribution analysis

Configuration snapshots from GCMC simulations were used to construct methane distribution for each of the three pores present in DUT-48, DUT-49 and DUT-50 at selected loadings (Supplementary Figure 75).



Supplementary Figure 75. Comparison of experimental (open symbols) and simulated (red line) methane adsorption isotherm at 111 K including selected loadings for radial distribution analysis (RDA) of a) DUT-48, b) DUT-49, and c) DUT-50.

Attributing each methane molecule to each of the pores was achieved via a python script using the pymatgen structure object (Supplementary Figure 76).

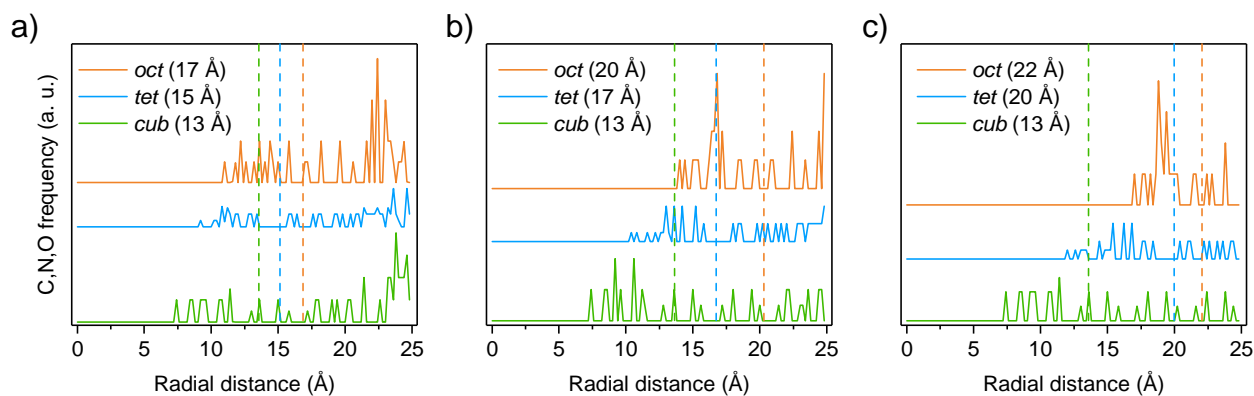
```
pore_label = []
for index_methane in methane_indices:
    methane_cub_dist = []
    for index_cub in cub_indices:
        methane_cub_dist.append(structure.get_distance(index_cub, index_methane))
    methane_tet_dist = []
    for index_tet in tet_indices:
        methane_tet_dist.append(structure.get_distance(index_tet, index_methane))
    methane_oct_dist = []
    for index_oct in oct_indices:
        methane_oct_dist.append(structure.get_distance(index_oct, index_methane))

    if min(methane_cub_dist) < cub_cut:
        pore_label.append("cub")
        continue
    if min(methane_oct_dist) < oct_cut:
        pore_label.append("oct")
        continue
    if min(methane_tet_dist) < tet_cut:
        pore_label.append("tet")
        continue

amount_cub.append(pore_label.count("cub"))
amount_tet.append(pore_label.count("tet"))
amount_oct.append(pore_label.count("oct"))
```

Supplementary Figure 76. Python script using the pymatgen structure object for radial distribution analysis.

The script uses distance criteria between the adsorbate and the center of each pore to identify which pore the adsorbate is present within. We note that due to the aspherical nature of the pores the distributions are dependent on the sequence of applying the distance criteria. We choose to label in the order: cuboctahedral, octahedral and tetrahedral. This as the tetrahedral pore volume is both part of the cuboctahedral and octahedral pore volume. The key lines of the python code are displayed in Supplementary Figure 76 and a minimal working example is deposited in the supporting information. The amount of methane in each pore was further averaged over 100 snapshots. This was also repeated for structures resulting from the *in situ* CD₄ neutron diffraction experiments. The choice of cut-off for each of the pores was chosen by analysing the radial distribution of the framework atoms from the centre of each of the pores.



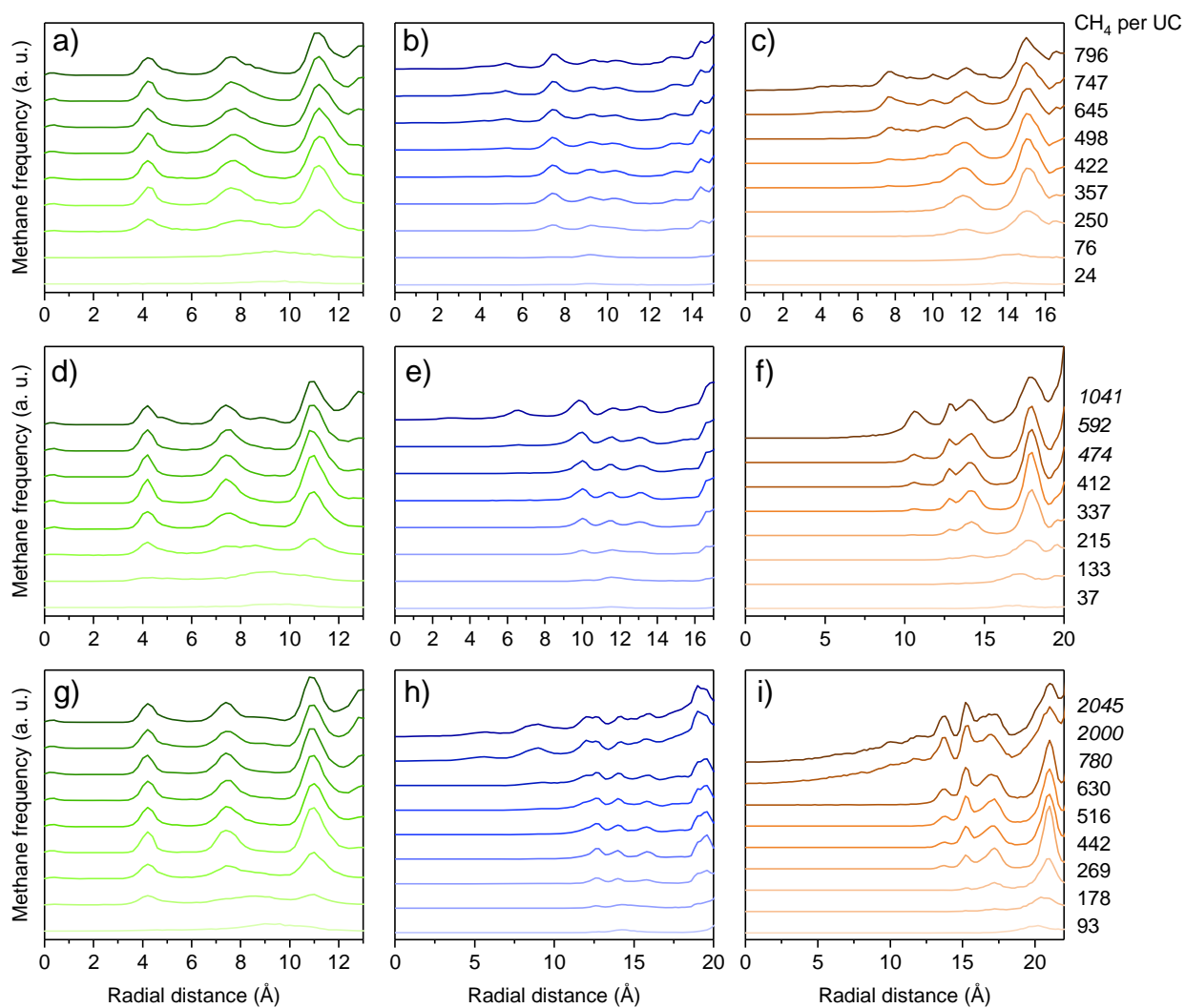
Supplementary Figure 77. Radial distribution of carbon, nitrogen, and oxygen atoms in the guest free framework of a) DUT-48, b) DUT-49, and c) DUT-50. Crystallographic origin of the octahedral pore (0.5,0.5,0.5), tetrahedral pore (0.25,0.25,0.25), and cuboctahedral pore (0,0,0). Dashed lines indicate cut off radius for the radial distribution analysis of methane filled MOFs.

Values of the chosen cut offs are displayed in Supplementary Figure 77 and summarized in Supplementary Table 34.

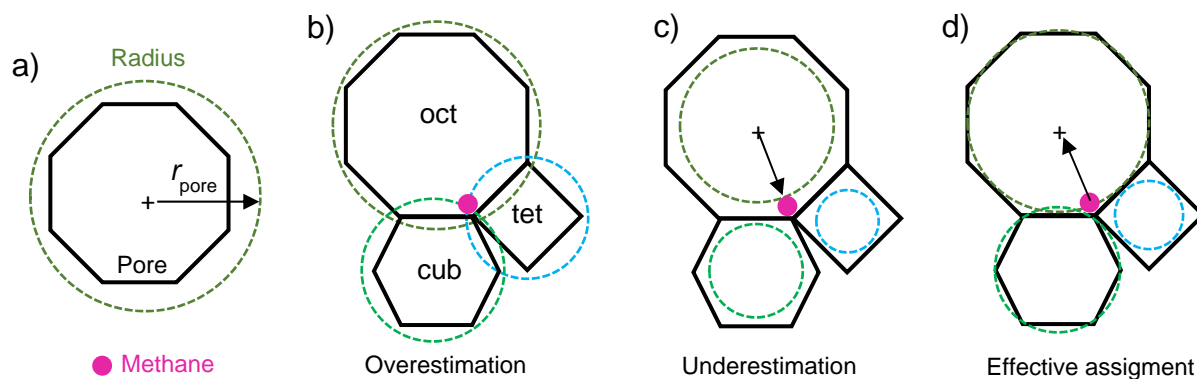
Supplementary Table 34. Cut-off radii for radial distribution analysis.

Material ID	<i>Cub</i> (Å)	<i>Tet</i> (Å)	<i>Oct</i> (Å)
DUT-48	10.6	12.4	14.4
DUT-49	10.6	14.6	17.2
DUT-50	10.6	17.4	19.8

To visualise the distribution of the adsorbates within each of the pores, the radial distribution relative to the pore was computed. This is similar to computing a radial distribution function but is not normalised to the radial volume as it is calculated from centre of the pore and at higher loadings the center point can contain a significant density of gas. The radial frequency of adsorbates and C, N, O atoms of the framework for each of the pores in DUT-48, DUT-49 and DUT-50 for increasing loading are displayed in Supplementary Figure 77 and Supplementary Figure 78, respectively



Supplementary Figure 78. Radial distribution of methane in the pores of a-c) DUT-48, d-f) DUT-49, and g-i) DUT-50. Crystallographic origin of the octahedral pore (orange, c,f,i) (0.5,0.5,0.5), tetrahedral pore (blue, b,e,h) (0.25,0.25,0.25), and cubo-octahedral pore (green, a,d,g) (0,0,0). Loadings of the corresponding distribution curves are indicated at the right.



Supplementary Figure 79. Scheme of radial distribution analysis in a trimodal pore structure similar to DUT-49.

5 Supplementary References

- 1 Schindelin, J. *et al.* Fiji: an open-source platform for biological-image analysis. *Nat. Methods* **9**, 676-682 (2012).
- 2 Krause, S. *et al.* Adsorption Contraction Mechanics: Understanding Breathing Energetics in Isorecticular Metal–Organic Frameworks. *J. Phys. Chem. C* **122**, 19171-19179 (2018).
- 3 Rowland, C. A. *et al.* Methane Storage in Paddlewheel-Based Porous Coordination Cages. *J. Am. Chem. Soc.* **140**, 11153-11157 (2018).
- 4 Lu, W. *et al.* Highly porous metal-organic framework sustained with 12-connected nanoscopic octahedra. *Dalton Trans.* **42**, 1708-1714 (2013).
- 5 Weseliński, L. J., Luebke, R. & Eddaoudi, M. A Convenient Preparation of 9H-Carbazole-3,6-dicarbonitrile and 9H-Carbazole-3,6-dicarboxylic Acid. *Synthesis* **46**, 596-599 (2014).
- 6 Stoeck, U. *et al.* Assembly of metal-organic polyhedra into highly porous frameworks for ethene delivery. *Chem. Commun.* **51**, 1046-1049 (2015).
- 7 Krause, S. *et al.* The effect of crystallite size on pressure amplification in switchable porous solids. *Nat. Commun.* **9**, 1573 (2018).
- 8 Krause, S. *et al.* A pressure-amplifying framework material with negative gas adsorption transitions. *Nature* **532**, 348-352 (2016).
- 9 Helmholtz-Zentrum Berlin für Materialien und Energie. The MX beamlines BL14.1-3 at BESSY II. *Journal of large-scale research facilities* **2**, 1-6 (2016).
- 10 Battye, T. G. G. *et al.* iMOSFLM: a new graphical interface for diffraction-image processing with MOSFLM. *Acta Cryst. D* **67**, 271-281 (2011).
- 11 Winn, M. D. *et al.* Overview of the CCP4 suite and current developments. *Acta Cryst. D* **67**, 235-242 (2011).
- 12 Sparta, K. M. *et al.* XDSAPP2.0. *J. Appl. Crystallogr.* **49**, 1085-1092 (2016).
- 13 Sheldrick, G. A short history of SHELX. *Acta Cryst. A* **64**, 112-122 (2008).
- 14 Sheldrick, G. Crystal structure refinement with SHELXL. *Acta Cryst. C* **71**, 3-8 (2015).
- 15 Spek, A. Structure validation in chemical crystallography. *Acta Cryst. D* **65**, 148-155 (2009).
- 16 Willems, T. F. *et al.* Algorithms and tools for high-throughput geometry-based analysis of crystalline porous materials. *Microporous Mesoporous Mater.* **149**, 134-141 (2012).
- 17 Gómez-Gualdrón, D. A. *et al.* Application of Consistency Criteria To Calculate BET Areas of Micro- And Mesoporous Metal–Organic Frameworks. *J. Am. Chem. Soc.* **138**, 215-224 (2016).
- 18 Farha, O. K. *et al.* Metal–Organic Framework Materials with Ultrahigh Surface Areas: Is the Sky the Limit? *J. Am. Chem. Soc.* **134**, 15016-15021 (2012).
- 19 Hönicke, I. *et al.* Balancing Mechanical Stability and Ultrahigh Porosity in Crystalline Framework Materials. *Angew. Chem. Int. Ed.* **57**, 13780-13783 (2018).
- 20 Llewellyn, P. L. & Maurin, G. Gas adsorption microcalorimetry and modelling to characterise zeolites and related materials. *C. R. Chimie* **8**, 283-302 (2004).
- 21 NIST REFPROP (National Institute of Standards and Technology, 2018).
- 22 Beurroies, I. *et al.* Using Pressure to Provoke the Structural Transition of Metal–Organic Frameworks. *Angew. Chem. Int. Ed.* **49**, 7526-7529 (2010).

- 23 Ramaswamy, P. *et al.* Mechanical properties of a gallium fumarate metal-organic framework: a joint experimental-modelling exploration. *J. Mater. Chem. A* **5**, 11047-11054 (2017).
- 24 Yot, P. G. *et al.* Metal-organic frameworks as potential shock absorbers: the case of the highly flexible MIL-53(Al). *Chem. Commun.* **50**, 9462-9464 (2014).
- 25 Yot, P. G. *et al.* Exploration of the mechanical behavior of metal organic frameworks UiO-66(Zr) and MIL-125(Ti) and their NH₂ functionalized versions. *Dalton Trans.* **45**, 4283-4288 (2016).
- 26 Yot, P. G. *et al.* Impact of the Metal Centre and Functionalization on the Mechanical Behaviour of MIL-53 Metal–Organic Frameworks. *Eur. J. Inorg. Chem.* **2016**, 4424-4429 (2016).
- 27 Henke, S. *et al.* Pore closure in zeolitic imidazolate frameworks under mechanical pressure. *Chem. Sci.* (2018).
- 28 Helmholtz-Zentrum Berlin für Materialien und Energie. KMC-2: an X-ray beamline with dedicated diffraction and XAS endstations at BESSY II. *Journal of large-scale research facilities* **2**, A49 (2016).
- 29 Bon, V. *et al.* In situ monitoring of structural changes during the adsorption on flexible porous coordination polymers by X-ray powder diffraction: Instrumentation and experimental results. *Microporous Mesoporous Mater.* **188**, 190-195 (2014).
- 30 Datasqueeze 2.2.9 Graphical Tool for X-ray Data Analysis v. 2.2.9 (2012).
- 31 Wojdyr, M. Fityk: a general-purpose peak fitting program. *J. Appl. Crystallogr.* **43**, 1126-1128 (2010).
- 32 Bail, A. L. Whole powder pattern decomposition methods and applications: A retrospection. *Powder Diffr.* **4**, 316-326 (2005).
- 33 FULLPROF (Laboratoire Le'on Brillouin (CEA–CNRS), France, 2006).
- 34 Material Studio 5.0 (Accelrys Software Inc., San Diego, USA, 2009).
- 35 Helmholtz-Zentrum Berlin für Materialien und Energie. E9: The Fine Resolution Powder Diffractometer (FIREPOD) at BER II. *Journal of large-scale research facilities* **3**, A103 (2017).
- 36 Roisnel, T. & Rodríguez-Carvajal, J. WinPLOTR: A Windows Tool for Powder Diffraction Pattern Analysis. *Mater. Sci. Forum* **378-381**, 118-123 (2001).
- 37 Getzschmann, J. *et al.* Methane storage mechanism in the metal-organic framework Cu₃(btc)₂: An in situ neutron diffraction study. *Microporous Mesoporous Mater.* **136**, 50-58 (2010).
- 38 Wu, H. *et al.* Metal-Organic Frameworks with Exceptionally High Methane Uptake: Where and How is Methane Stored? *Chem. Eur. J.* **16**, 5205-5214 (2010).
- 39 Wu, H., Zhou, W. & Yildirim, T. Methane Sorption in Nanoporous Metal–Organic Frameworks and First-Order Phase Transition of Confined Methane. *J. Phys. Chem. C* **113**, 3029-3035 (2009).
- 40 Bogdan, K. *et al.* Adsorption-Induced Structural Phase Transformation in Nanopores. *Angew. Chem. Int. Ed.* **56**, 16243-16246 (2017).
- 41 Carrington, E. J., Vitorica-Yrezabal, I. J. & Brammer, L. Crystallographic studies of gas sorption in metal-organic frameworks. *Acta Cryst. B* **70**, 404-422 (2014).
- 42 Glaser, T. *et al.* Infrared study of the MoO₃ doping efficiency in 4,4'-bis(N-carbazolyl)-1,1'-biphenyl (CBP). *Org. Electron.* **14**, 575-583 (2013).
- 43 Stoeck, U. *et al.* A highly porous metal-organic framework, constructed from a cuboctahedral super-molecular building block, with exceptionally high methane uptake. *Chem. Commun.* **48**, 10841-10843 (2012).

- 44 Bureekaew, S. *et al.* MOF-FF – A flexible first-principles derived force field for metal-organic frameworks. *Phys. Status Solidi B* **250**, 1128-1141 (2013).

Krause et al - Towards NGA design - ESI.pdf (3.82 MiB)

[view on ChemRxiv](#) • [download file](#)

Other files

MOF-FF optimized simulated structures.zip (247.99 KiB)

[view on ChemRxiv](#) • [download file](#)

SCXRD-cif.zip (48.45 KiB)

[view on ChemRxiv](#) • [download file](#)
